UCSF
UC San Francisco Electronic Theses and Dissertations

Title
Physical and Cellular Mechanisms Underlying Villus Morphogenesis in the Mammalian Small Intestine

Permalink
https://escholarship.org/uc/item/00p9w9v9

Author
Miyazaki, Hikaru

Publication Date
2021

Peer reviewed|Thesis/dissertation

eScholarship.org Powered by the California Digital Library
University of California

Physical and Cellular Mechanisms Underlying Villus Morphogenesis in the Mammalian Small Intestine

by

Hikaru Miyazaki

DISSERTATION

Submitted in partial satisfaction of the requirements for degree of

DOCTOR OF PHILOSOPHY

in

Bioengineering

in the

GRADUATE DIVISION

of the

UNIVERSITY OF CALIFORNIA, SAN FRANCISCO
AND
UNIVERSITY OF CALIFORNIA, BERKELEY

Approved:

DocuSigned by:

Zev Gartner

6E99B613A5754DD...

Chair

DocuSigned by:

Ophir Klein

Ophir Klein

DocuSigned by:

Kevin Healy

B9D5E09D2ED9475...

Committee Members

Copyright 2021
by
Hikaru Miyazaki

Dedication and Acknowledgements

I am honored to share the accomplishment of earning this Ph.D. with the many others that have helped and supported me throughout my journey.

First and foremost, I was very lucky to have two close collaborators and mentors, Dr. Tyler Huycke and Dr. Teemu Hakkinen to work with on our project together, in the second half of my PhD. Tyler is an inspiring scientist; I learned a lot from his efficient, strategic, and productive ways to work as a scientist. Teemu has provided me a lot of insights from his mathematical and computational background, and his logical thinking and approaches helped me put our experimental findings into perspective and determine priorities. My thesis includes our collaborative efforts. Tyler has contributed experimental data of some of the explant pharmacological inhibitor experiments and tissue recombination experiments. All the computational models were implemented by Teemu. This work truly could not have developed into what it is now without them, and I am extremely thankful for the opportunity to work closely with them and grow as a scientist with their support.

I also had a unique opportunity to be co-mentored by Prof. Zev Gartner and Prof. Ophir Klein, and I learned a lot from their mentorships. Zev's excitement and enthusiasm for science kept energizing me to keep working on my project, and I appreciated his detailed attentions to my experimental data and suggestions for next steps. Ophir taught me how to best get help and resources from the surrounding networks and showed me how functional and efficient organizations should be run. I struggled to open-up and ask for help in the beginning, so it was an eye-opening learning and the mindset for me that we always should be reaching out to ask for help. I

am thankful to have been a part of both great labs, filled with so many excellent scientists that have supported me and taught me a lot of valuable scientific insights and ways to think.

Both Gartner lab and Klein lab were such supportive and welcoming environment, and I found many role models as well as friends among my colleagues. I'd like to thank Dr. Alex Hughes for giving me a first exposure to the morphogenesis and intestinal villus development – which later became my project, and Dr. Jimmy Hu, Dr. Sachiko Furukawa and Axel Rosendahl for training me on many basic laboratory techniques that became a basis of my research. Dr. Chris McGinnis and Dr. Eric Chow were both enormously helpful in helping me with the MULTI-seq experiments even during their holiday time back in December 2018. Dr. Dario Boffelli and Vaka Dedeepya assisted me with the single-cell sequencing data analysis. I also would like to thank Prof. Krishna Garikipati from University of Michigan for discussion and providing initial simulation code for phase-separation model and Prof. Matt Thomson from Caltech and Jake Cornwall Scoones from The Francis Crick Institute for providing initial simulation code for vertex model.

My bay-mates in Klein lab, Dr. Amnon Sharir, Dr. David Castillo and Efren Reyes had been a great company to work around with. The conversation related or unrelated to science, brightened my days and made my everyday work in the lab much more enjoyable. My research could not have been possible without the supports by many people in the lab and facilities at UCSF. I especially would like to thank Dr. Adriane Joo, Dr. Pauline Marangoni, Brooks Hoehn, Nick Wang and Asoka Rathnayake for making sure the lab is run smoothly so we could focus on our research. Dr. Kyle Marchuk, Dr.

John Eichorst and Jordan Briscoe from BIDC were very helpful in guiding me through my search for appropriate imaging systems. Tomoko Kakegawa and Vinh Nguyen at the flow core were particularly generous with their time and insights and helped me get high-quality cells of my need. Sergio Pedroza Lopez from animal facility were also extremely helpful. Nadia Ayad and Dr. Roger Oria Fernandez from Weaver lab helped me with running AFM experiments and generating ECM functionalized polyacrylamide gels and I am very thankful for their generosity with their time and sharing their expertise. Dr. Katie Cabral, Dr. Jennifer Hu and Dr. Rebecca Kim provided me with a lot of insights and encouragements as senior graduate students in the labs. I could not name all, but I feel very blessed to have gotten help from, worked alongside with, and have built friendship with everyone in both Gartner and Klein lab. I also would like to thank my dissertation committee and qualifying exam committee – Prof. Kevin Healy, Prof. Todd McDevitt, Prof. Marshall Wallace and Prof. James Bayrer for providing me with insightful feedback and teaching me how to think critically.

I am also thankful for all the friendship I have developed during PhD and maintained from the past. Spending time with them gave me happiness, restoration, and the energy to keep going. I have been fortunate to have met and built friendships with Penporn Koanantakool, Mangpo Phothilimthana, Inez Raharjo, Jennifer Ferrante, Camille Simoneau, and Taia Wu as my roommates. I appreciate all the fun time we spent together and the continuous love and support I received from Miho Kitagawa, Nancy Teresa, Lynda Han, Hansol Kang, and Sam Liu throughout my PhD time. Kunwoo Lee and IGSM encouraged me and helped me put my life into perspective when I was going through a difficult time in the beginning of my Ph.D. Our occasional

boardgame nights and dinner with Sophie Wang and Donald Eng really refreshed my mind and soul. I also would like to thank John Kim for all the great time we had together in the midst of Ph.D. and more importantly, for being my biggest supporter and cheerleader in the past four years.

My scientific pursuit and education could not have been possible without the support of my family. I thank my parents for providing me with all the opportunities and believing in me to make who I am today. In particular, my father understood the difficulties I have faced as a scientific trainee and was very encouraging throughout my Ph.D.

The past six and the half year as a PhD student was the hardest time in my life, but I learned more about who I am and made me appreciate my surroundings even more. And I am truly thankful for all the learning experience.

Physical and Cellular Mechanisms Underlying Villus Morphogenesis in the Mammalian Small Intestine

Hikaru Miyazaki

Abstract

Intestinal villi are luminal protrusions that are essential for efficient nutrient absorption. In mammals, villus formation initiates during embryogenesis with evagination of the intestinal epithelium and underlying mesenchyme into the lumen. This event is tightly coupled both temporally and spatially with the emergence of PDGFRα-expressing mesenchymal cells immediately below the epithelium that condense to form aggregates. While several signaling pathways have been linked to mesenchymal cell clustering and subsequent villus initiation, the physical and cellular mechanisms of villus cluster formation remain unclear. To uncover these mechanisms, we performed live imaging of intestinal explants and discovered that dynamic mesenchymal motility drives the formation of mesenchymal cell clustering and initiates epithelial morphogenesis. To identify the molecular underpinnings of this process, we performed single-cell RNA sequencing at multiple stages of villus morphogenesis, which revealed the emergence of cell adhesion and contractility programs within clustering PDGFRα-expressing cells. Further, pharmacological inhibition of these programs prevents clustering and villus formation, implicating that they are required for this process. A computational vertex model is used to simulate the clustering dynamics, demonstrating that differential motility and adhesion are both necessary and sufficient for the clustering. The computational model directly connects cluster formation and villus initiation to the

cellular properties. The model predictions and results obtained from explant tissue and *in vitro* engineered system display close correspondence, suggesting the robustness and applicability of our proposed model. Together, these results provide a new understanding and a cellular mechanism describing how mammalian intestinal villi are initiated.

Table of Contents

1 Introduction 1

1.1 Tissue structures for organ functions and development 2

1.1.1 Functions of tissue structures 2

1.1.2 Application of developmental biology for an advancement of biotechnology 4

1.2 Physical mechanisms of morphogenesis 6

1.2.1 Morphogenesis by local cell transformation 6

1.2.2 Morphogenesis by global tissue transformation 9

1.3 Small intestine 12

1.4 Small intestinal villus morphogenesis 15

1.4.1 Villus development in chick 16

1.4.2 Villus development in mouse 18

2 Results 24

2.1 Villus initiation is driven by dynamic activity of clustering mesenchymal cells 24

2.2 Single cell sequencing of developing intestine reveal molecular signature suggestive of increased adhesion program at clustering PDGFRα^{High} mesenchymal cells 33

2.3 Adhesion and actomyosin activity are required for mesenchymal cluster formation 55

2.4 Exploring physical models that explain the mechanism of villus morphogenesis 66

2.4.1 Spring Model 66

2.4.2 Phase-Separation Model 68

2.4.3 Vertex Cell-base Model 71

2.5 Application to an engineered *in vitro* living model system 82

3 Material and Methods 85

4 Discussion 99

4.1 Discussion 99
4.2 Unresolved questions 108
4.3 Future directions 110
4.4 Conclusion 112
References 113

List of Figures

1.1 Structure determines cell identities during development 5

1.2 Examples of physical mechanisms of morphogenesis 11

1.3 The small intestinal epithelium 14

2.1 Dynamic motility of PDGFRα^{High} mesenchymal cells drive cluster formation and initiation of epithelial deformation leading to villus development 28

2.2 Neither muscle confinements nor proliferation are required for mesenchymal cell clustering and initiation of villus morphogenesis 30

2.3 Tracking of cell nuclei motion on live imaging data reveal increased motility in PDGFRα^{High} clustering mesenchymal cells 31

2.4 Single-Cell Sequencing of the developing intestine reveals emergence of PDGFRα^{High} cell population that have upregulation of motility and adhesion programs 38

2.5 Overview of single-cell sequencing result 40

2.6 Slingshot analysis revealed pseudotime prediction closely matching the developmental trajectory 42

2.7 Upregulation of cell adhesion programs in PDGFRα^{High} cell populations 44

2.8 Development epithelium cell population is captured in the single-cell RNA sequencing data.....45

2.9 *Fabp1, Agr2* and *Cck* expression in developing intestine 47

2.10 Regional-dependent signature of epithelium and mesenchymal cell populations 48

2.11 Expression of adhesion-related genes and proteins in mesenchyme 60

2.12 Adhesion and contractility programs are indispensable for PDGFRα^{High} mesenchymal cluster formation 61

2.13 E15.5 Intestinal tissues of *Myh9* and *Myh10* double knockout in epithelium 62

2.14 E15.5 Intestinal tissues of *Myh9* and *Myh10* double knockout in mesenchyme 63

2.15 Mesenchymal *Myh9, Myh10* double knockout intestines were more sensitive to lower doses of blebbistatin treatments.....65

2.16 Model prediction by spring model and biological observations 76

2.17 Evidence supporting liquid-like behavior of PDGFRα^{High} mesenchymal cells 78

2.18 Phase separation model of villus patterning and folding 79

2.19 Vertex model predictions of villus morphogenesis and biological observations.....80

2.20 Sorted PDGFRα^{EGFP} cells seeded in Matrigel surface break up into clusters.....83

2.21 Comparison between *in vitro* engineered MEF clustering and computational predictions 84

3.1 Examples of curvature and 90% dispersion distance analysis.....88

3.2 Example images of stiffness measurement of targeted tissue location.....94

List of Tables

2.1 Markers of embryonic small intestinal cell populations in scRNA-seq data.....49

2.2 Cluster markers of subepithelial mesenchymal cell populations 50

2.3 Top 100 and Bottom 100 loadings of PC1 component among the subepithelial mesenchymal cell populations.....51

2.4 Cluster markers of epithelium populations 52

2.5 Top 100 and Bottom 100 loadings of PC1 component among the epithelium populations 53

2.6 Top 100 and Bottom 100 loadings of PC6 component among the subepithelial mesenchymal cell populations.....54

2.7 Summary of Integrin alpha and beta subunit pairs and their predicted ECM binding partners 65

3.1 Summary of mouse genetics utilized in the study 86

3.2 Summary of tissue segments and replicates obtained from each tissue for the single-cell sequencing experiment 90

1. Introduction

The luminal surface of the small intestine in many species is covered by finger-like protrusions called villus (*plural* villi). These structures contribute to the function of the intestine by increasing the absorptive surface area by more than 6 times, thereby improving nutrient absorption efficacy (Helander and Fändriks, 2014). In both mammalian and avian species, embryonic villus morphogenesis, which constitutes of formation of epithelial folds, is accompanied by formation of cell clusters in the adjacent subepithelial mesenchyme. Even though the final function and structure of the villi are similar in both mammalian and avian species, the question regarding active cell components underlying the morphogenesis and mechanisms of how these mesenchymal cell clusters emerge has not been definitely settled in the field. Different mechanisms have been proposed to be responsible for avian and mammalian villus morphogenesis.

The goal of this dissertation is to investigate the physical and cellular mechanisms underlying villus morphogenesis in the mouse small intestine. I identified subepithelial mesenchymal cells as the mechanically active cell components in forming clusters and initiating villus morphogenesis. Molecular investigation through single-cell RNA sequencing suggested that cell adhesion and contractility programs were upregulated in these clustering mesenchymal cell populations. Using explant pharmacological inhibition assays, my collaborators and I revealed that adhesion through integrins and actomyosin activity are indispensable for cluster formation and subsequent villus development. Based on these results, we implemented a

computational model proposing that differential cell motility and adhesion are both necessary and sufficient to describe mesenchymal cell cluster formation. Further, we have engineered an *in vitro* system demonstrating that a similar cell aggregation phenomenon can be recreated using simpler components – signifying the applicability of the suggested mechanism in a broader context, including tissue engineering. The proposed physical mechanisms likely apply to human development as well, thus contributing to our understanding of the conditions that are required for healthy villus development and, conversely, the conditions that might contribute to common human diseases such as celiac and inflammatory bowel diseases.

1.1 Tissue structures for organ functions and development

1.1.1 Functions of tissue structures

Organs contain populations of cells that perform each organ's main functions - such as the nutrient absorbing enterocytes of intestines and the milk-producing mammary epithelial cells of mammary glands, to name a few. These cells together with stroma – tissue that provides supportive, structural, or connective functions – form the functional unit of an organ. However, having all of the correct cell components is not sufficient to produce a functional organ; they need to be organized in space to orchestrate and carry out its function. For example, intestinal tubes are surrounded by smooth muscle layers. The contraction and relaxation of the muscle layers produce a peristaltic wave and propel the luminal contents down the long intestinal tube. In addition, tissues and organs themselves can form micro-scale structures critical to their functions. The small intestine not only has a long tubular shape as its macro-scale

structure, but its luminal surface is also composed of finger-like protrusions, the villi, that are critical to efficient organ function by increasing the absorptive surface area of the gut.

In addition to tissue functionality, some tissue structures have been suggested to be important for the development of the tissue itself. For example, morphogen gradient patterns generated in a structure-dependent manner can define the identity of cells in a spatial-dependent manner. For example, the balance between muscle-inducing Hedgehog, secreted from the epithelial layer, and muscle-suppressing Bone Morphogenetic Protein 4 (BMP4), upregulated in the mesenchyme by the same epithelium originated Hedgehog signals, define location of muscle development (**Fig. 1.1**A). This explains how muscle layers are formed a specific distance away from the epithelium and towards the outer layer of the intestinal tube (Huycke et al., 2019). In addition, Shyer and colleagues have suggested that initial bending of the intestinal epithelium defines compartmentalized distributions of differentiated epithelial cells. Their study showed that the initial epithelial curvature creates a pocket of concentrated epithelial-oriented morphogen signals in the mesenchyme at the villus tip. The mesenchymal cells in turn signal back to the epithelium to repress progenitor identity in the epithelium, thereby inducing differentiation at the villus surface while restricting proliferative progenitor cells to the base (Shyer et al., 2015) (**Fig. 1.1**B). The structures of restricted stem cells at the villi base are maintained throughout development, and the epithelial compartmentalization in the crypt-villus axis is critical in achieving rapid and efficient epithelial renewal.

1.1.2 Application of developmental biology for an advancement of biotechnology

Understanding of developmental biology has been fundamental in advancing the field of regenerative medicine. Over the past few decades, discovery of pluripotent stem cells such as embryonic stem cells (ESCs) and induced pluripotent stem cells (iPSCs) have laid the foundation for emerging new areas of biotechnology. They have enabled the generation of models of human development and disease and provided platforms for the generation of cells and tissues for research and transplantation for treatment of diseases. Achieving the full potential of these technologies is dependent on the ability to efficiently generate functional cell types from the undifferentiated stem cells. Translating the principles of developmental biology has been the most successful approach to direct differentiation of stem cells (Irion et al., 2008; Shahjalal et al., 2018). By sequentially culturing the stem cells in media cocktails that recapitulate key signaling conditions, many types of differentiated cells including cardiomyocytes, hematopoietic cells, hepatocytes, as well as pancreatic beta cells can now be generated.

Recapitulating developmental pathways is not only a tool of biologists and engineers to generate cells, but indeed damaged tissue itself may redeploy developmental programs to regenerate or repair itself. For example, damaged small intestinal or colonic epithelium exhibit a fetal-like reversion phenotype before regenerating adult epithelial cell types to restore homeostasis (Nusse et al., 2018; Sprangers et al., 2021; Yui et al., 2018).

While application of developmental principles have been hugely successful in the differentiation of many cell types and construction of simple organoids, the incorporation of structural cues or mesenchyme have not been explored as actively yet.

Understanding the developmental programs that regulate organ formation is an important step toward recreating better engineered tissue *in vitro* or regenerating damaged organs *in vivo* for disease modeling and regenerative medicine in the future.

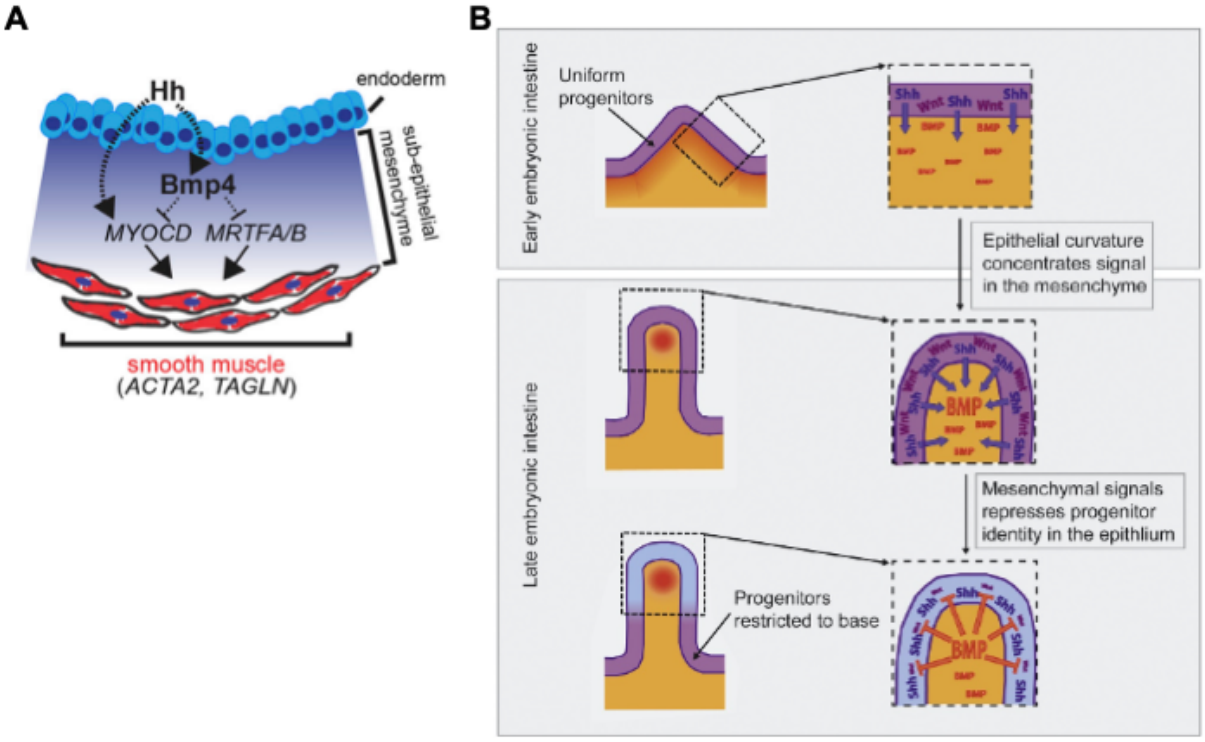

Figure 1.1 Structure determines cell identities during development A. Hedgehog and Bmp signaling control spatial differentiation of muscle layers. Hh is expressed by the endoderm and activates Bmp4 expression in the subjacent non-muscle mesenchyme, where its concentration is highest. Bmp4 subsequently acts at high concentrations to inhibit smooth muscle differentiation in subepithelial area, while allowing the induction of muscle formation at a distance farther away, where inhibitory Bmp levels are lower. Adapted from Huycke *et al.* 2019. **B.** Epithelial curvature concentrates Hh signal in the mesenchyme at the villus tip. Mesenchymal signals in turn represses progenitor identity in the epithelium at the villus surface. Adapted from Shyer *et al.* 2015.

1.2 Physical mechanisms of morphogenesis

In order for three-dimensional structures such as folds or branched networks to be generated by tissue, physical forces are required to cause deformations to pre-existing tissue (Misra et al., 2016). Several physical mechanisms have been described as mechanisms underlying epithelial buckling tissue morphogenesis. These mechanisms can be broadly divided into two classes of mechanisms: morphogenesis triggered by local transformation of cell behavior and tissue-wide mechanical instability resulting in tissue morphogenesis. Below, I cover a few of the mechanisms studied.

1.2.1 Morphogenesis by local cell transformation

One of the simplest and best described mechanisms that results in epithelial sheet deformation relies on spatial patterns of apical or basal cell contractility. The mechanism involves accumulation of active tension on one surface of an epithelial sheet, driving negative strain on the apical or basal surface of the epithelium, and ultimately bending of the sheet (Sawyer et al., 2010) (**Fig. 1.2**A). These constrictions are driven by contraction of an apical meshwork of filamentous actin (F-actin) by the molecular motor myosin and are characterized by increased expression of F-actin and phosphorylated myosin light chain (pMLC) on the shrinking surface (Lecuit and Lenne, 2007). Early reports of apical constriction driven morphogenesis included early stages of mesoderm invagination in Drosophila (Leptin, 1995; Lewis, 1947). Recently, apical constriction has been suggested to be the driver for crypt formation in the mouse intestine. Epithelium at the site of invagination showed characteristic wedge-like cell-shape and increased contractility gene profiles (Sumigray et al., 2018). Crypt structure

formation in *in vitro* small intestinal epithelial organoids has also been suggested to be driven by the same mechanism (Hartl et al., 2019).

Another example of epithelial-driven morphogenesis includes suprabasal intercalation. This mechanism explains how a multilayered stratified epithelium such as in the tooth, hair follicle and mammary gland form placodes – local epithelial thickenings accompanied by invagination. Panousopoulou and Green have observed tissue-wide tension present in the intercalating superficial layers of cells. These observations lead to the hypothesis that horizontal tension exerted by the suprabasal layer that forms a canopy over its underlying basal layer is the main driver of the invagination (Panousopoulou and Green, 2016) (**Fig. 1.2**B).

Another hypothesis explaining mechanisms of branching morphogenesis includes localized differential proliferation of cells. Theoretically, increased material in a localized area can result in mechanical instability and buckling morphogenesis of the region. Spatial patterns of increased proliferation have been observed in various branching epithelia such as the small intestine, salivary gland, mammary gland and kidney (Bernfield et al., 1972; Bresciani, 1968; Michael and Davies, 2004). However, the source of pre-patterning of proliferation signals has not been identified in many of the tissue systems, as epithelial-only organ systems still resulted in similar proliferation patterns and resulting morphogenesis. A more careful study observing proliferation patterns during lung morphogenesis reported that proliferation patterns arise only after morphogenesis is initiated (Weaver et al., 2000). These results suggest that although local proliferation is often observed during epithelial morphogenesis of many tissues, it

is inconclusive whether differential proliferation is the underlying physical mechanism (Varner and Nelson, 2014).

In addition to epithelial cells, stromal components have also been suggested to have roles in physically generating mechanical forces that lead to buckling morphogenesis. In the process of avian lung airway branching morphogenesis, apical constriction is sufficient to drive the initiation of monopodial branching with characteristic wedge-shaped profiles of epithelial cells and actomyosin contraction signature (Kim et al., 2013). These branching events colocalize with the site of fibroblast growth factor 10 (Fgf10) expression in submesothelial mesenchyme (Bellusci et al., 1997). However, for the subsequent bifurcation of the airway epithelium, wrapping of the airways by smooth muscle has been suggested to have an important role. Smooth muscle actin alpha expressing cells appear at the basal surface of the epithelial site where the future cleft is formed, and the following bifurcations are dependent on the presence of those smooth muscles. These results suggest that physical restraint imposed by localized smooth muscle around the cleft site is required for terminal bifurcation of the airway branching morphogenesis (Kim et al., 2015) (**Fig. 1.2**C).

Further, in hair follicles, contractility-driven cellular activities were suggested to be responsible for aggregation of dermal progenitors. These aggregate formations precede local changes in tissue structure and differential cell behavior of overlying epidermis (Shyer et al., 2017). Aggregation of contractile mesenchymal cells also exhibited local bending morphogenesis of ECM-based hydrogel sheets *in vitro*. Traction forces generated by mesenchymal cells on ECM strain the surface of the gel, resulting in curvature formation of the sheet (Hughes et al., 2018) (**Fig. 1.2**D).

1.2.2 Morphogenesis by global tissue transformation

Global mechanical instability caused by compression of elastic sheets results in buckling of the layer. In the case of tissue morphogenesis, the elastic sheets under compression often are growing inner epithelial layers, and compressive stress is applied by other layers such as outer muscle layers. The differential growth of the two connected layers results in mechanical instability, and the tissue releases the accumulating stresses by bending out of plane. Depending on the geometry of the system and the material properties of the conjoined tissue layers, this process can result in highly regular patterns of folds. Examples of morphogenesis driven by such mechanisms include intestinal villus morphogenesis in chick (Shyer et al., 2013) and aligned folds formation in mouse oviduct (Koyama et al., 2016). Though geometrically in a different configuration, gut looping is also driven by global differential growth between two connected pieces of tissue. Slowly expanding mesenteric sheets geometrically constrict the lengthening intestinal tube, achieving the looped formation of intestinal gut tubes that efficiently pack into the body cavity (Savin et al., 2011).

Tallinen and colleagues showed that the brain's gyral and sulcal fold formation can also be explained by global mechanical compression. During development of the brain, the outer cortex layer is rapidly growing in comparison to the underlying soft tissues. This growth differential results in mechanical compression of the outer layer, leading to formation of folds. They have demonstrated that the phenomenon can be recreated by using engineered 3D mimicry of the brain constructed with layered soft gels of differential swelling properties. These physical models not only developed

gyrification patterns similar to those of the real brain, but also followed spatiotemporal courses that closely mimic brain development (Tallinen et al., 2016).

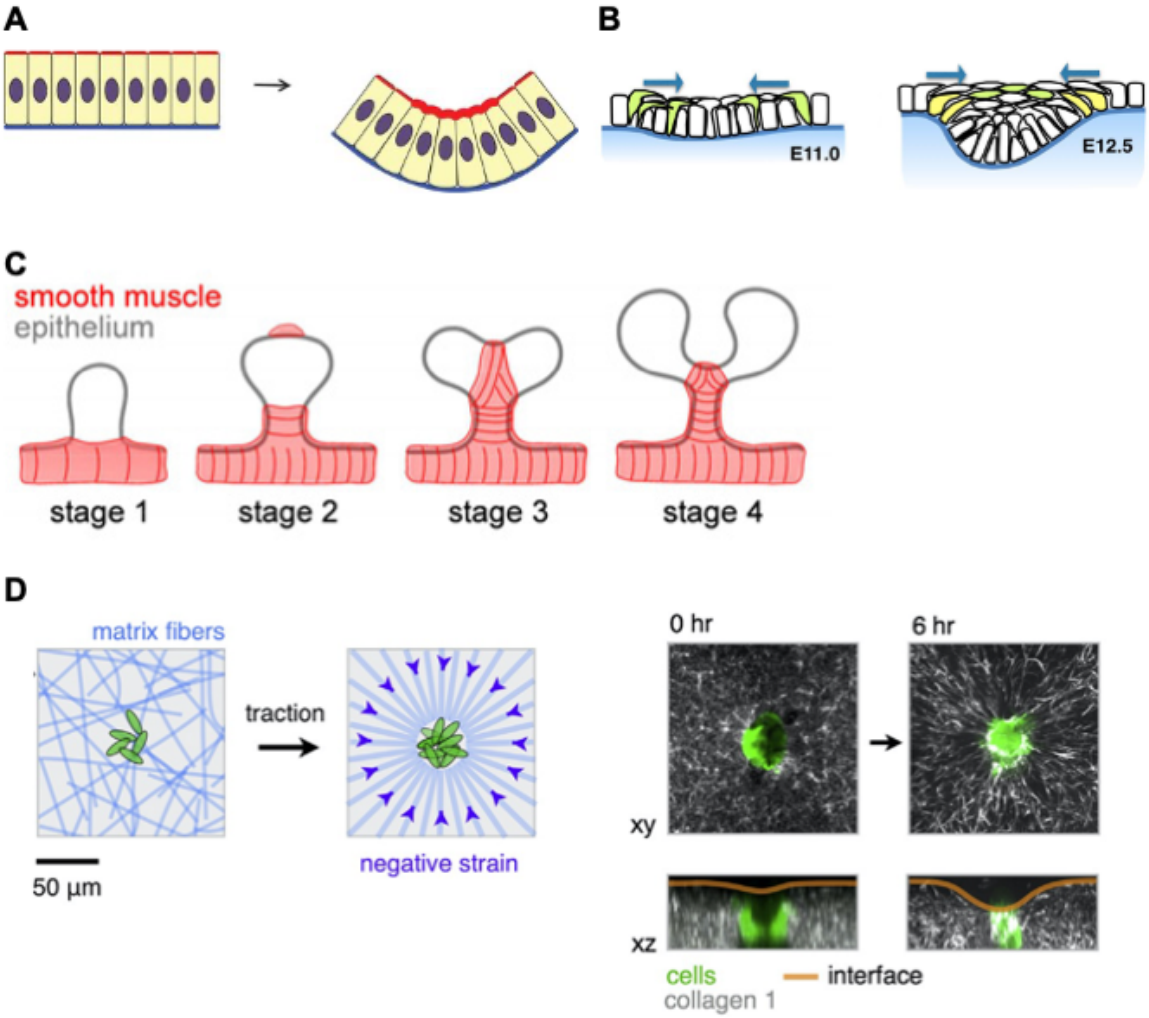

Figure 1.2 Examples of physical mechanisms of morphogenesis A. Simplified schematics of apical constriction. Accumulated actomyosin meshwork at the apical surface (depicted by red cable) gives rise to wedge-shaped cells and bending of the layer. Adapted from Pearl *et al.* 2017. **B.** Diagrammatic summary describing suprabasal intercalation driven placode invagination. Elongated suprabasal cells that form a canopy over basal epithelium exert tension and create a shallow bend. Adapted from Panousopoulou and Green, 2016. **C.** Schematic showing localization of smooth muscle during bifurcation of the airway epithelium. Smooth muscle wrapping of the epithelium at the cleft site is required for bifurcation. Adapted from Kim *et al.* 2016. **D.** Schematic (left) and experimental result (right) showing mesenchymal cell compaction on an ECM-based hydrogel. Compacting cells exert traction forces and align ECM fibers around the cell cluster, resulting in generation of strain at the surface and emergence of surface curvature. Adapted from Hughes *et al.* 2018.

1.3 Small intestine

The small intestine is the primary site of enzymatic breakdown and absorption of most nutrients including carbohydrates, proteins and fats in our body. The tubular organ is as long as 2m in humans, and the long tubular structure helps it obtain a large luminal surface area in which nutrients can be digested and absorbed. The surface area of the intestinal luminal area is further increased by macro and micro fold structures called villi and microvilli. Villi are finger-like structural protrusions that line the luminal surface of the small intestinal tubes. Microvilli are subcellular protrusions on the apical surface of the epithelial cells that further increase the total surface area. Villi and microvilli together are thought to amplify the small intestinal luminal surface area by 60 to 120 times relative to the initial flat stage, making the effective total mucosal surface area of human small intestinal epithelium as large as $32m^2$, approximately the size of a badminton court (Helander and Fändriks, 2014). The loss of intestinal epithelium surface area by villus atrophy, or significant reductions of the number of villi such as in celiac disease, results in insufficient absorption of nutrients. Villus atrophy is also associated with several symptoms of intestinal dysfunctions, including diarrhea, abdominal distention and excessive nutrients deficiency (Kwon et al., 2020).

The base of each villus is bounded by at least six crypts of Lieberkuhn, invaginating epithelial structures with a flask-like shape. They house dedicated epithelial populations of actively cycling intestinal stem cells marked by expression of Lgr5 at the base, along with progenitor cells that self-renew, to maintain epithelial function throughout life (Barker, 2014). The invaginated structures also physically protect these cells from luminal contents and pathogens (Sumigray et al., 2018).

A single-layered intestinal epithelium lines the luminal surface. Small intestinal epithelial cells include nutrient-absorbing enterocytes, mucin-secreting goblet cells, hormone-producing enteroendocrine cells, and other specialized cell types (Clevers, 2013). The epithelium also functions as a barrier to prevent transfer of harmful microorganisms, antigens and toxins from the gut lumen to elsewhere in the body. Intestinal epithelial cells have one of the fastest turnover rates in our body. They completely renew every 2 to 6 days in both humans and mice, with up to 10^{11} cells or as much as 200 grams of epithelial cells being lost and renewed every day in humans (Barker, 2014; Darwich et al., 2014; Mayhew et al., 1999). The stem cells and transit-amplifying cells in the crypts proliferate and generate differentiated intestinal epithelial cells. The newly generated differentiated cells migrate up toward the villus surface, where they perform their delegated functions and get extruded at the villus tip. The homeostatic equilibrium between the generation and loss of cells is maintained efficiently through a conveyor belt system in the crypt-villus axis (Williams et al., 2015) (**Fig 1.3**A,B).

One of the most significant advances in the field of intestinal research has been the development of *in vitro* intestinal organoid culture methods. A single adult intestinal epithelial stem cell can be grown to form an organoid *in vitro.* These epithelial-only three-dimensional tissues exhibit structures that recapitulate crypt architecture, and they also contain all of the resident epithelial cell types (Sato et al., 2009) (**Fig. 1.3**C,D). Organoid technology makes it possible to more easily test different culturing conditions or to image the cells. However, the other basic architecture of the intestine – villus

protrusion structures – are not formed in the epithelial-only organoids, suggesting that villus structure formation is not intrinsic to the epithelium alone.

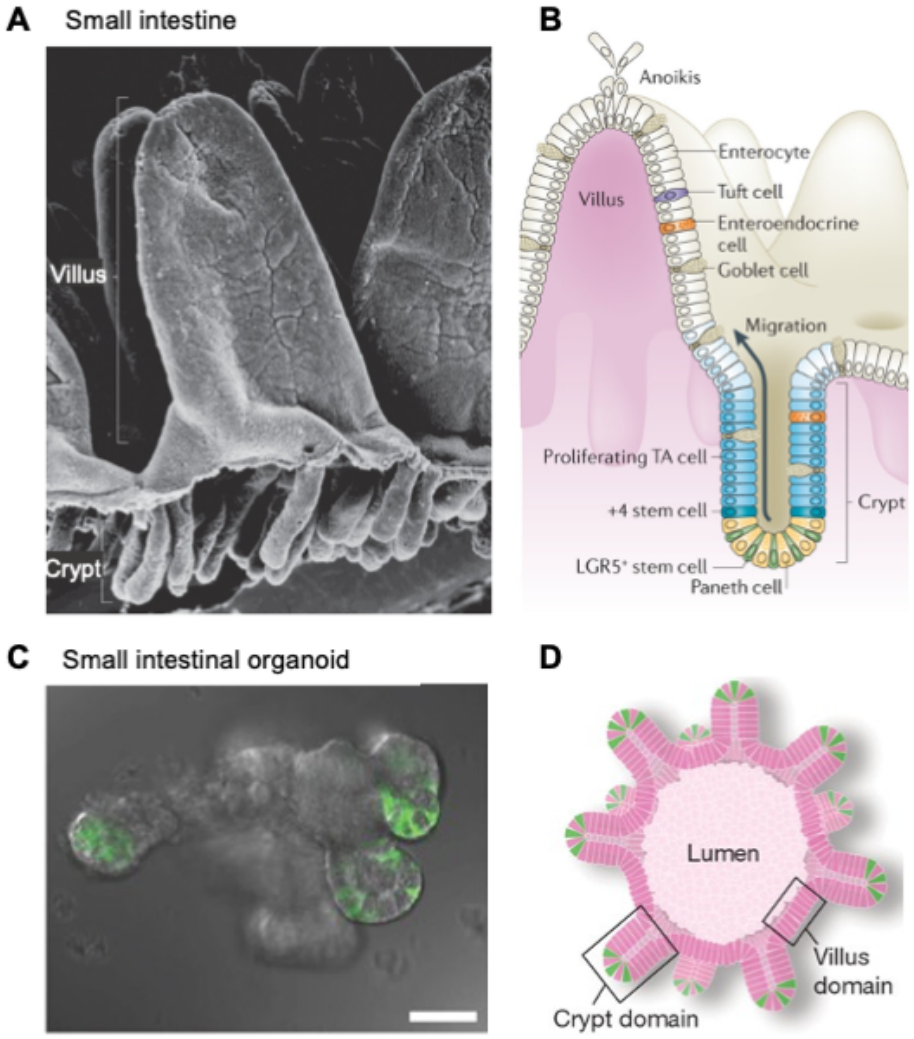

Figure 1.3 The small intestinal epithelium A.B. A scanning electron micrograph (A) and a diagram (B) of the small intestine. Lgr5-expressing stem cells are located at the crypt base. The stem cells continuously generate rapidly proliferating transit-amplifying (TA) cells, which differentiate into the various functional cells on the villus in a conveyor belt system. Adapted from Barker *et al.* 2014. **C.D.** A microscopic image (C) and a diagram (D) of an intestinal epithelial organoid. Lgr5-GFP cells are marked green and are located at the base of crypts. Scale bar 50 μm. Figure adapted from Sato *et al.* 2009.

1.4 Small intestinal villus morphogenesis

Crypt structures form during early neonatal time points (between postnatal day 5 to 10 in mice), with myosin-II driven apical constriction of epithelium as an underlying mechanism (Sumigray et al., 2018). Villus structures, on the other hand, are formed much earlier in development, during the embryonic stage. Their morphogenesis start at E14.5 and emerged villi are visible at E15.5 in mice, week 6 and week 8 in human and E8 and E16 in chick, respectively (Shyer et al., 2013; Spence et al., 2011; Walton et al., 2015). Villus formation begins in the duodenum and progressively spreads to the distal ileum (Kammeraad, 1942; Walton et al., 2012).

In mammals, the formation of villi is tightly associated both spatially and temporally with the formation of cell clusters in the subepithelial mesenchyme. These mesenchymal cell clusters are characterized by high expression of genes such as *Pdgfra* (Platelet Derived Factor receptor-alpha), *Ptch1* (Patched 1) and *Bmp3* (Bone Morphogenetic Protein 3) (Karlsson et al., 2000; Shyer et al., 2015; Spence et al., 2011; Walton et al., 2012). Similar mesenchymal cell clusters are also observed in the emerged villi of chick.

Despite the similar final structure and function of villi across many species, it is unclear whether unifying mechanisms drive the morphogenesis in different animal species. Two different physical mechanisms have been proposed to be responsible for villus morphogenesis in chick and mouse (Walton et al., 2018).

1.4.1 Villus development in chick

One of the characteristics observed in chick villus development is the sequential luminal structure transitions from flat (E8) to longitudinal ridges (E9-12), and zigzag patterns (E13-15) before finally transforming into individual villi (E15-17) (Shyer et al., 2013; Walton et al., 2018). Concomitantly with each transition, layers of smooth muscle are formed in the following order: an inner circular layer, an outer longitudinal layer, and an inner longitudinally oriented muscularis mucosa layer, respectively; this suggests possible roles of constricting muscle layers in intestinal villus morphogenesis (Coulombre and Coulombre, 1958; Shyer et al., 2013).

Shyer and colleagues investigated the role of smooth muscle layers in the morphogenesis of villi. Their study concluded that constriction of the growing inner tissue mass by the developing outer muscle is responsible for each of the structural transitions. At the ridge and zigzag stages, they separated the muscle layer from the inner mesenchymal and epithelial tissue composite, and measured the length of each of the layers. This revealed that inner mesenchyme-epithelial composite layers unfold to circumferential or longitudinal length greater than that of the muscle layers, indicating that these inner tissue layers were under radial and longitudinal compression by the outer muscle layer at each stage. In addition, inhibition of smooth muscle development with the use of small molecule inhibitors (AG1295 and FK506) impaired the formation of new muscle layers and their corresponding structural transitions, confirming that muscle layer differentiation is indispensable for the luminal structural formations. Further, they showed that the tissue of the epithelial layer is more than 10 times stiffer than that of adjacent mesenchyme. Mathematical model assuming solid-elastic property of the

tissue incorporated relative material stiffnesses, geometrical properties, and differential growth of the tissue. The model predicted the formation of ridges and zigzags of the constricted growing epithelial layer.

However, further examination of this model found that additional compression by inner longitudinal muscularis mucosa were not sufficient to explain the transition from zigzag to individual villi structures. Instead, additional localized proliferation of epithelium and mesenchyme at the sides of the zigzag valley were proposed to drive the zigzag structures to twist and form into individual bulges (Shyer et al., 2013).

The same group further suggested that the compartmentalization of different epithelial cell populations in the villus-crypt axis is a result of villus structure formation (Shyer et al., 2015). Despite the uniform expression of hedgehog (Hh) signals by epithelium at the initiation of vilification, Hh-dependent genes and other mesenchymal cluster marker genes such as *Ptch1*, *Bmp4* and *Pdgfra* were only induced in the mesenchyme at the tips of villi. This led them to hypothesize that the induction of mesenchymal cluster identity is structure-dependent, and that concentration gradients of epithelial-derived signaling control the induction of cluster marker genes in the mesenchymal cells at the villus tips. To test this, they artificially imposed luminal villus-protrusion-like-folds on explanted epithelium by placing a fine grid. Induced villus cluster genes were observed in the mesenchyme of the artificial villus structures. These observations led them to conclude that the formation of mesenchymal cell clusters is not a cause but rather a consequence of villi structure. Their study further suggested that these mesenchymal clusters in turn suppress the epithelial progenitor identity in villi tips, accomplishing compartmentalization of epithelium into differentiated epithelium at the

villus surface while maintaining proliferating progenitor populations at the base. The separation of the epithelium domain into proliferative and less-proliferative domains along the crypt-villus axis is maintained until adulthood and likely contributes to elongation of villus structure during development (Shyer et al., 2015).

1.4.2 Villus development in mouse

One of the biggest differences between villus development in avian and mammalian species is that mammalian intestines do not undergo sequential morphogenesis through the ridge and zigzag forms, but instead, villus structures directly emerge from the smooth surface of the lumen (Sbarbati, 1982; Walton et al., 2018). Villus development occurs in multiple rounds, with new villi emerging between existing villi (Walton et al., 2012).

Contribution of muscle confinement

Villi arise only after circular smooth muscle layers are formed in both chick and mouse. When muscle layer differentiation is inhibited with small molecule inhibitors, villi do not develop (Shyer et al., 2013). However, in comparison to chick, the smooth muscle layers differentiate much more rapidly in mice (within a 2-day period, instead of over 4 days in chick). In addition, the mouse epithelium is only 1.5 times as stiff as the mesenchyme, compared to the 10-fold difference in chick (Shyer et al., 2013). Using the same elastic solid model used to describe ridge and zigzag structure formation of chick intestine, the computational simulation suggested that the same mechanism of tissue confinement by outer muscle could describe the direct villus morphogenesis

mechanism. The different sequences of paths taken to form individual villus structures could be explained by differences in epithelium material properties.

However, comprehensive investigations by Walton and colleagues in mouse tissue have suggested that the mechanical folding mechanism driven by muscle layer confinement is unlikely the cause of villus emergence in mice. There is no temporal correlation between muscle layer development and villus morphogenesis. The inner circular muscle layer is already developed at E13.5, before villus morphogenesis initiates, while the outer longitudinal muscle layer is not formed until E16.5, after the first round of villus structures are already formed. Muscularis mucosa, the third inner longitudinal layer of muscle, remains immature at E16.5 and is discontinuous even at E18.5, a time point at which most of the villi are already elongated. The maturation of muscle layers is thus not temporally coincident with villus emergence (Walton et al., 2015).

In addition, when circular muscle confinement was released by longitudinally cutting open the tube of explant intestinal tissue, the explant still formed mesenchymal cell clusters. Corresponding to each cluster, villus structures were also formed. These experiments provide additional evidence that questions the proposed requirement of muscle confinement in villus morphogenesis (Walton et al., 2015).

In another study, over-activation of Hh signaling in mesenchyme was achieved by genetically knocking out the Hh downstream inhibitor genes *Sufu* (Suppressor of fused homolog) and *Spop* (Speckle-type POZ protein) in intestinal mesenchyme. In these mouse models, the muscle layers were expanded, highly disoriented, and no longer organized into circular and longitudinal layers. In addition, contraction of the

muscle cells was severely impaired. Despite the absence of functional muscle layers, the PDGFRα+ expressing mesenchymal cells clustered, and corresponding villus formation was observed, supporting the idea that active muscle layers are dispensable for intestinal vilification in mice (Coquenlorge et al., 2019).

Further, regarding the issue of whether mesenchymal cluster formation is a cause or consequence of structural transformation, Walton and colleagues also conducted grid-placement experiments on mouse tissue to artificially induce luminal deformation. In contrast to what had been suggested based on the investigations done with chick, the scaling relation between the sizes of imposed folds and the sizes and numbers of resulting mesenchymal cell clusters did not hold. Instead of each structural fold corresponding to one villus and one mesenchymal cluster, multiple mesenchymal cell clusters were observed per grid area when grid sizes were increased from 55 μm to 75 μm and multiple villi were formed accordingly. These experiments suggested that epithelial deformation is not sufficient to induce the characteristic mesenchymal cluster formation and villus morphogenesis in mice (Walton et al., 2015).

Contribution of soluble signals

Based on the correlation between the presence of mesenchymal clusters and emergence of villi, mesenchymal cluster formations are now thought to directly initiate villus morphogenesis in mice. Several studies have revealed that soluble ligands such as BMP, Hh, and Platelet Derived Growth Factor A (PDGFA) promote villus morphogenesis by impacting the mesenchymal cell population (Karlsson et al., 2000; Kwon et al., 2020; Walton et al., 2012).

As in the chick, Hh ligands are secreted by the developing intestinal epithelium of mice. Hh receptors and downstream targets such as Ptch1 and Gli1 (GLI family Zinc finger 1) are expressed in mesenchymal clusters. Inhibition of Hh signaling prevents cluster formation and villus development, suggesting a requirement for Hh signaling in the initiation of mesenchymal cluster formation and subsequent emergence of villi (Madison et al., 2005; Walton et al., 2012). Upregulation of Hh, on the other hand, increased the size of mesenchymal cell clusters and corresponding villi width. These results suggested that paracrine Hh signaling from the epithelium to the Hh-responsive mesenchymal cells drives the formation and size of mesenchymal cell clusters and, consequently, the emergence of villi.

They noted that the mesenchymal cells at the clusters were mostly non-proliferative, ruling out a mechanism by which the cluster formation is driven by locally induced proliferation (Karlsson et al., 2000; Walton et al., 2012). Bmp signaling has been suggested to pattern and drive mesenchymal cell clustering in the intestine. In addition to expressing Hh receptors, the subepithelial mesenchymal cell population and clustered mesenchymal cells express several BMP genes, such as *Bmp3, Bmp4, Bmp5*, and *Bmp1*. In addition, some BMP modifier genes including *Nog* (Noggin) and *Fstl1* (Follistatin Like 1) are also expressed at the sites of clusters or throughout the mesenchyme, respectively, around the same developmental time frame. Addition of a local BMP ligand source by placing BMP soaked agarose beads on explant tissue locally inhibited mesenchymal cell cluster formation and subsequent villus emergence. Further, global inhibition of BMP signaling by treating explant cultures with the small molecule BMP inhibitor, Dorsomorphin, resulted in formation of larger mesenchymal

clusters and some ‘stripe-like’ fused patterns of mesenchymal clusters. Based on the resemblance of the BMP regulated cluster patterns, and the patterns obtainable by a Turing reaction-diffusion mechanism in which diffusing, mutually interacting activator and inhibitor molecules produce stable morphogen patterns, these authors hypothesized that mesenchymal clustering patterns are generated by the reaction-diffusion mechanism. BMP ligands and BMP inhibitors were proposed to act as Turing inhibitors and activators, respectively. These patterned morphogens in turn would serve as cues to turn on cluster marker genes in mesenchymal cell populations (Walton et al., 2015).

PDGFA (Platelet Derived Growth Factor A) and PDGFRα are another paracrine ligand-receptor pair expressed in epithelium and mesenchymal cell clusters of developing intestines, respectively. *Pdgfa* deletion caused reduced proliferation of mesenchyme during development and a reduced number and irregular width and length of villi in adults. However, the initiation of villus morphogenesis as characterized by *Pdgfra*-expressing mesenchymal cell cluster formation was not impaired. In a parallel experiment, now knocking out the receptor, *Pdgfra*, the mice with the mutation were not able to survive past embryonic day E16.5. However, the embryonic phenotype of villi was similar to that of *Pdgfa* knockout mice; mesenchymal cell clusters were observed with corresponding villus development, even though the number of villi was reduced, and each villus was wider. These results suggest that although the pathway is likely important for later villus elongation, it is indispensable for the mesenchymal cell cluster formation and initiation of villus morphogenesis (Karlsson et al., 2000).

Other mechanisms have also been suggested to explain mesenchymal cluster formation. The most recent study suggested the role of planar cell polarity (PCP) genes in cluster formation and subsequent villus morphogenesis. Using bulk-RNA sequencing from a *Sufu* and *Spop* mesenchymal knockout mouse, Hh over-activated mouse, this team identified PCP genes, including *Fat4* (FAT Atypical Cadherin 4), *Dchs1* and *Dchs2* (Dachsous Cadherin-Related 1 and 2), as direct target genes downstream of Hh signaling in mesenchyme. Knockout mice of *Fat4, Dchs1* as well as *Wnt5* (PCP ligand) genes all resulted in fusion of villi in parts of the small intestines (Rao-Bhatia et al., 2020). These data suggest the possible roles of planar cell polarity pathways in proper mesenchymal cell clustering and subsequent villi formation.

While several signaling pathways have been linked to mesenchymal cell clustering and subsequent villus initiation, the cellular mechanisms of villus cluster formation and how these implicated pathways are integrated in the mechanism to cause morphogenesis remain unclear. My thesis investigation aims to fill these gaps in knowledge.

2. Results

2.1 Villus initiation is driven by dynamic activity of clustering mesenchymal cells

Because it has been previously shown that mesenchymal cells at villus clusters upregulate expression of the *Pdgfra* gene(Karlsson et al., 2000; Walton et al., 2012), we began by investigating the emergence and localization of PDGFRα expressing mesenchymal cells in mouse intestinal tissue undergoing villus morphogenesis. Using mice that express H2B-EGFP fusion protein in the *Pdgfra* endogenous locus (Hamilton et al., 2003), PDGFRα expressing cells' nuclei were monitored in tissue from developmental time point E13.5 to E18.5 (**Fig. 2.1**A). At E13.5, the interface between the epithelium and mesenchyme is smooth and the mesenchymal cell population presents uniformly low expression of PDGFRα. At E14.5, cells with high expression of PDGFRα (PDGFRα^{High} cells) differentiate in the subepithelial layer of the mesenchyme – the earliest sign of villus morphogenesis. Between E14.5 and E15.5, mesenchymal clusters of PDGFRα^{High} cells start forming in the proximal portion of the small intestine concomitant with basal deformation of the overlying epithelium. This initially deformed epithelium subsequently evaginates and outgrows into the lumen to form individual villi. This series of events happens in a proximal to distal wave along the length of the intestine (Kammeraad, 1942; Walton et al., 2012). At spaces in between these forming villi, new rounds of PDGFRα^{High} cell differentiation occur to achieve approximately four rounds of cluster formation and villus emergence as described previously (Walton et al.,

2012). Here, we focus on understanding the mechanism driving the progression from the emergence of PDGFRα^{High} population to the formation of mesenchymal clusters and the initial epithelial deformation.

The presence of the outer smooth muscle layers allows compressive stresses to develop in the epithelium due to the in-plane growth of the cells. Confinement imposed by smooth muscle layers on the inner layers of subepithelial mesenchyme and epithelium were suggested to be necessary for villus morphogenesis of both chick and mouse (Shyer et al., 2013). However, compressive forces mediated by the muscle are dispensable in mice, as mesenchymal clusters and villi form even when the intestine is cultured after being cut open longitudinally, interrupting the radial confinement by the inner circular muscle (Walton et al., 2016). The villus morphogenesis was observed at the edges of the tissue as well. We repeated the experiment and confirmed that relaxation of muscle confinement, either by filleting open the gut or preventing smooth muscle contractility with Nifedipine, does not impede mesenchymal cluster formation and villus morphogenesis (**Fig. 2.2**A). In addition, when muscle differentiation was blocked genetically, by knocking out the master regulator of smooth muscle differentiation, *Myocardin,* in the intestinal mesenchyme, the PDGFRα^{High} mesenchymal cells clustered and the corresponding villi structures were observed despite significant loss of smooth muscle alpha actin (SMA) expressing muscle layer (**Fig. 2.2**B). Further, blocking epithelial growth by treating the explant tissues with the proliferation inhibitor Aphidicolin did not prevent the formation of mesenchymal clusters or villus initiation (**Fig. 2.2**C,D). Thus, constraining of growing inner epithelium by the outer muscle layer

is dispensable for villus initiation in mice, consistent with other recent reports (Coquenlorge et al., 2019; Walton et al., 2016).

We therefore began by examining how local activities of the subepithelial PDGFRα-expressing cells might drive villus initiation at the sites where they aggregate into villus clusters. To examine the dynamics of mesenchymal villus cluster formation and villus morphogenesis, we conducted live imaging of explant tissues expressing fluorescent reporters in both epithelium (*Shh*^{Cre}*, Rosa26*^{tdTomato}) and mesenchyme (*Pdgfra*^{EGFP}). To improve optical resolution and to minimize tissue movement by peristalsis, intestinal tubes were longitudinally cut open and treated with the calcium channel inhibitor Nifedipine, which blocks peristalsis without impairing cluster formation. The formation of mesenchymal cell clusters and basal epithelial deformation co-occurred in time and space (**Fig. 2.1**B, C), suggesting that cluster emergence might drive epithelial deformation.

To directly test this hypothesis, we replaced the native endoderm-derived epithelium with epithelium of non-intestinal origin, Madin-Darby Canine Kidney (MDCK) cells. Strikingly, the formation of PDGFRα^{High} mesenchymal cell clusters and corresponding epithelial deformation were observed (**Fig. 2.1**D). These results strongly support the notion that mesenchymal cells are the physical driver of the cluster formation that initiates epithelial morphogenesis of the villus.

Next, we investigated how these mesenchymal clusters form. Treating the explant tissues with the proliferation inhibitor Aphidicolin did not prevent the initiation of mesenchymal clusters and villus initiation, suggesting the initiation step is independent of proliferation, consistent with previous observations that villus clusters cells are non-

proliferative (**Fig. 2.2**C,D) (Walton et al., 2012). Together, these results indicate that clustering and initiation of morphogenesis is mesenchymal driven, and is not due to growing epithelium that buckles. We then monitored and tracked the emergence of clustered mesenchymal cells by live imaging. Using *Pdgfra*^{EGFP} explant tissue, we observed that the position of nuclei of PDGFRα^{High} mesenchymal cells were highly dynamic and motile in forming the clusters; indeed, some cells traveled from a distance of several nuclei away (**Fig. 2.1**E, **2.3**A). In contrast, cell nuclei that did not end up in clusters by the end of the imaging displayed minimal motility with lower level of nuclear EGFP expression (**Fig. 2.1**E-G, **2.3**A). Individual tracks of cell movement showed that long-distance traveling PDGFRα^{High} cells demonstrated bursts of high directional motility toward the point of clustering, followed by slower motility once closer to the destination cluster (**Fig. 2.3**B). However, the basal motility of these cells was also elevated: Even when the motility burst (above 10 μm/hr) data points were discarded from the dataset, the clustering cells still displayed differentially higher motility in comparison to the non-clustering PDGFRα^{low} cell nuclei (**Fig. 2.3**C,D). The observation of cell motility leading to formation of clusters contrasts with the traditional Turing reaction-diffusion based chemical morphogen patterning mechanism that has previously been invoked to describe villus cluster formation, in which cells change their state or identity according to the final morphogen patterns (Turing, 1952).

These results together strongly indicate that dynamic and active clustering of PDGFRα^{High} mesenchymal cells initiates the morphogenesis of epithelial evagination during mouse intestinal villus formation.

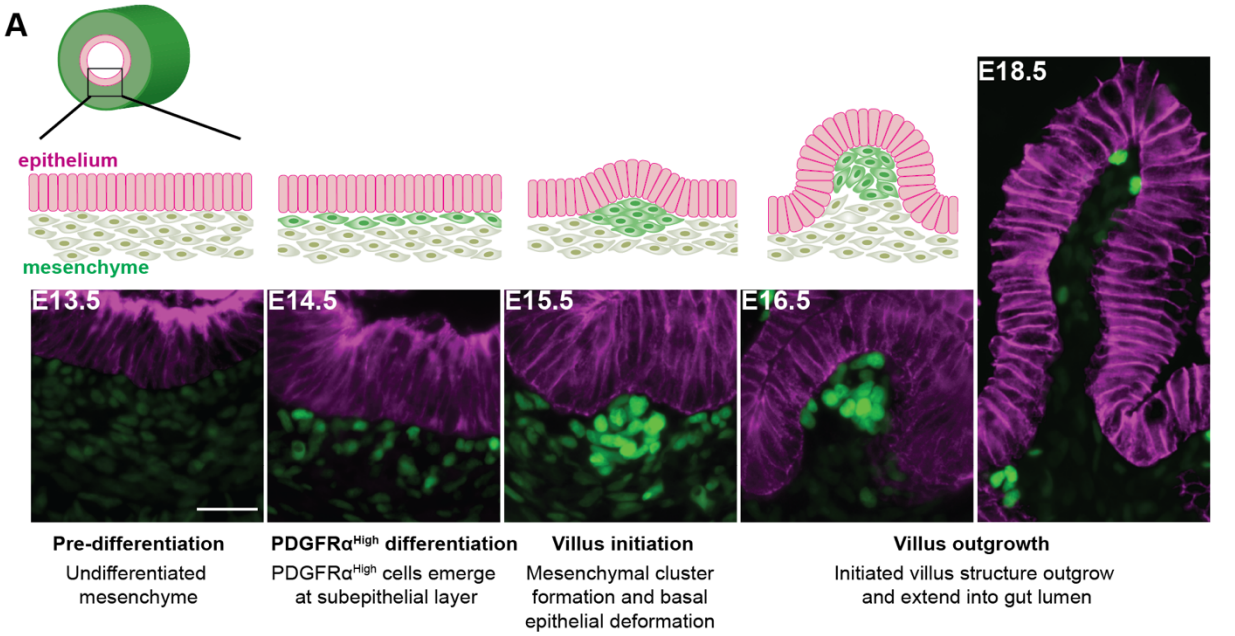
A
epithelium
mesenchyme
E13.5
E14.5
E15.5
E16.5
E18.5
Pre-differentiation
Undifferentiated mesenchyme
PDGFRα^High differentiation
PDGFRα^High cells emerge at subepithelial layer
Villus initiation
Mesenchymal cluster formation and basal epithelial deformation
Villus outgrowth
Initiated villus structure outgrow and extend into gut lumen

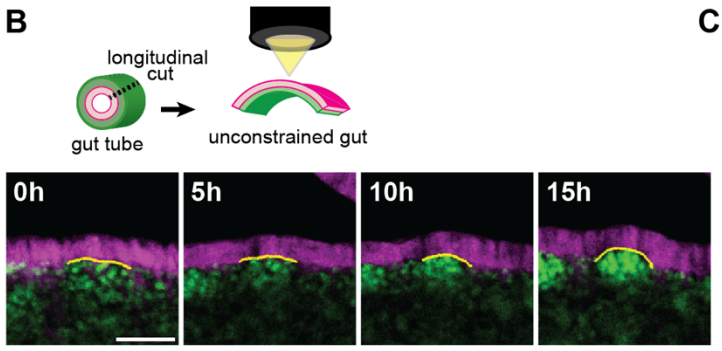
B
longitudinal cut
gut tube
unconstrained gut
0h
5h
10h
15h

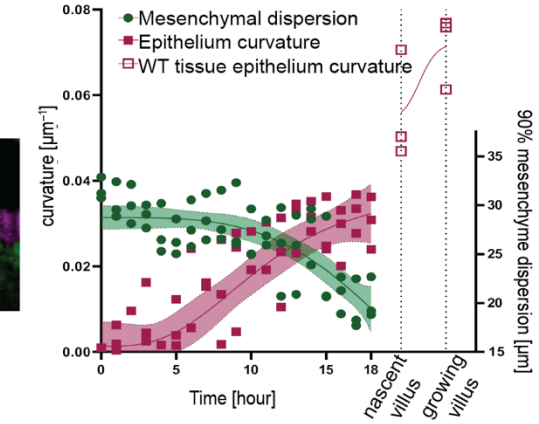
C
Mesenchymal dispersion
Epithelium curvature
WT tissue epithelium curvature
curvature [μm⁻¹]
90% mesenchyme dispersion [μm]
Time [hour]
nascent villus
growing villus

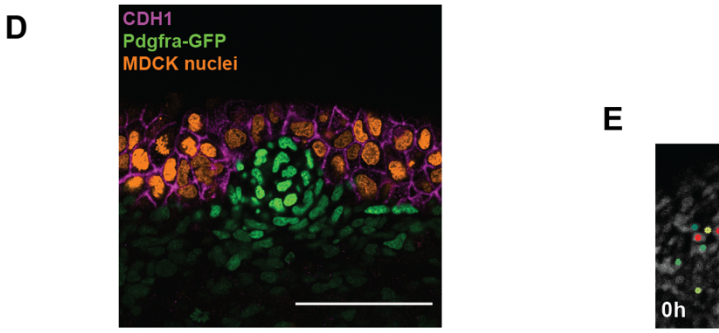
D
CDH1
Pdgfra-GFP
MDCK nuclei

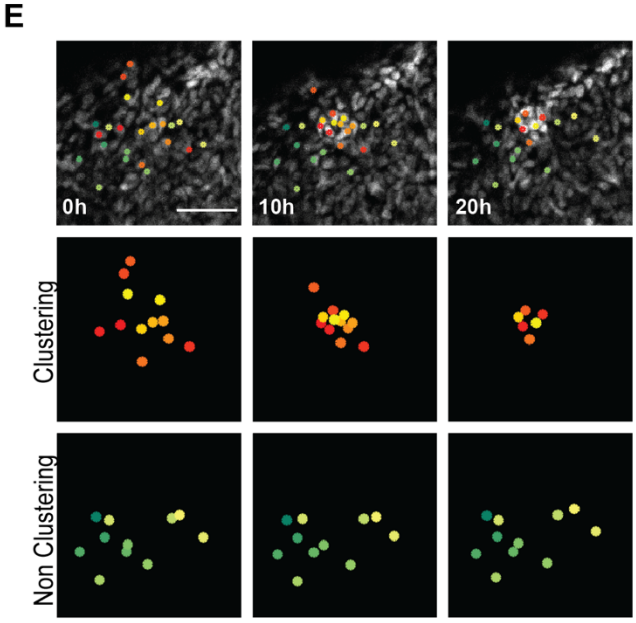
E
0h
10h
20h
Clustering
Non Clustering

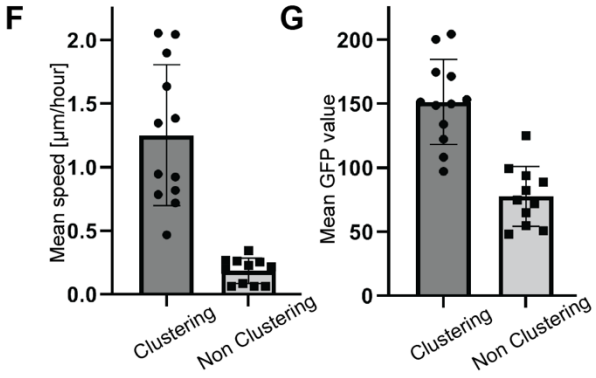
F
Mean speed [μm/hour]
Clustering
Non Clustering

G
Mean GFP value
Clustering
Non Clustering

Figure 2.1 Dynamic motility of PDGFRα^{High} mesenchymal cells drive cluster formation and initiation of epithelial deformation leading to villus development A. Overview of villus development between E13.5 to E18.5. Emergence and clustering of PDGFRα^{High} mesenchymal cells happen between E14 - E15.5. These deformed sites later elongate and outgrow into lumen to become individual villus. Scale bar = 25 μm. **B.** Live imaging of mesenchymal cell (green) and epithelial (magenta) population show co-occurrence of mesenchymal cluster appearance and epithelial deformation. Scale bar = 50 μm. **C.** Quantification of live-imaged data reveal increasing epithelial basal curvature and decreasing mesenchymal dispersion distance (lower values indicate tighter mesenchymal population) over the development. **D.** Explant tissue of epithelial cells replaced by Madin-Darby Canine Kidney (MDCK) cells revealed mesenchymal cell cluster formation and epithelial deformation. **E.** Live imaging and tracks of *Pdgfra*^{EGFP} nuclei during the cluster formation. All tracked cells (top), clustering cells (middle), and non-clustering cells (bottom) are shown. Tracked cells are color-labeled. Scale bar = 50 μm. **F.G.** Quantification of the live tracked nuclei data. Average speed (F) and Average GFP pixel value (G) of tracked *Pdgfra*^{EGFP} nuclei for clustering and non-clustering cell populations are computed.

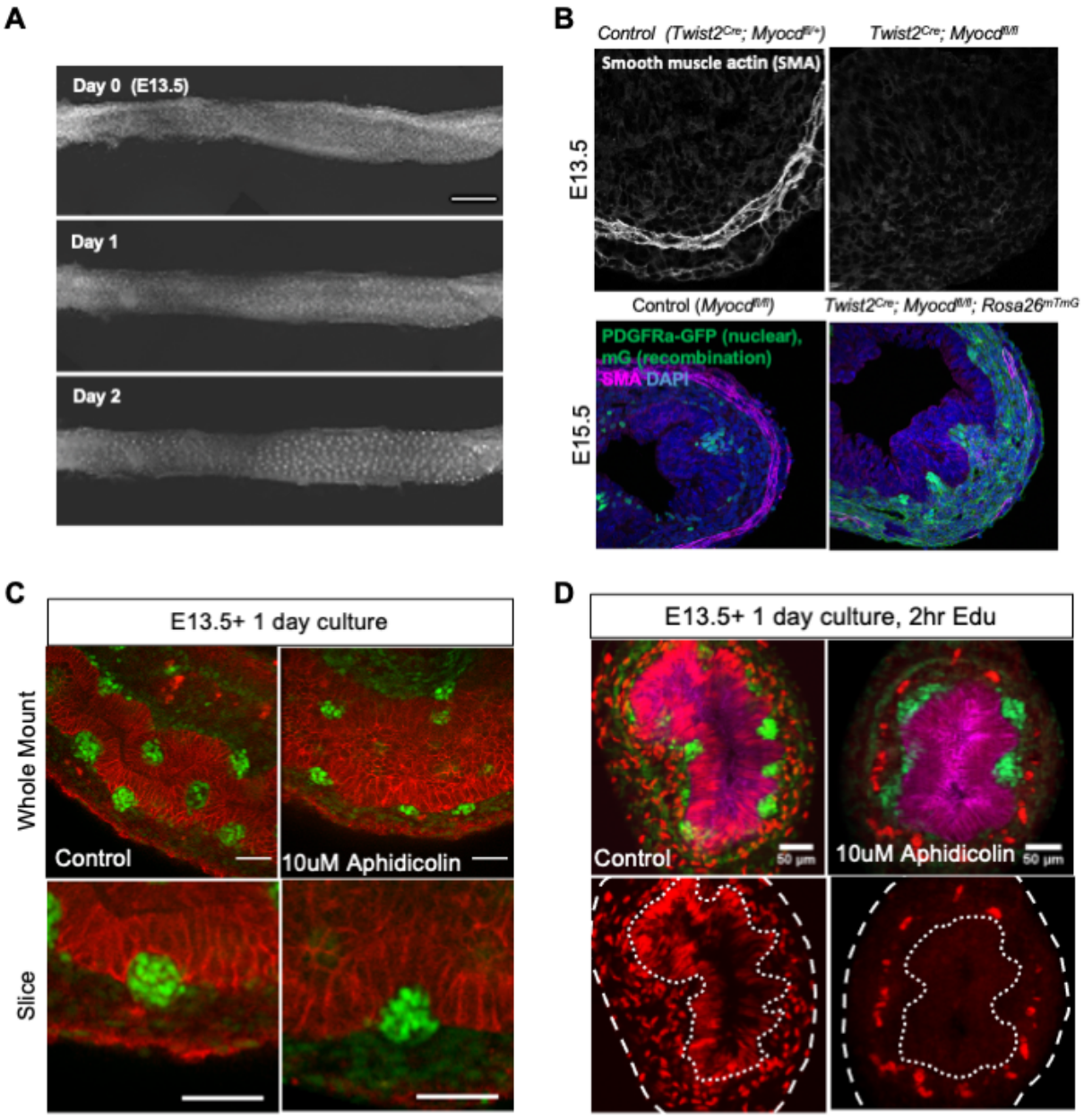

Figure 2.2 Neither muscle confinements nor proliferation are required for mesenchymal cell clustering and initiation of villus morphogenesis. A. Longitudinally cutting open the explant intestinal tube, thereby removing radial constraints by outer muscle layer, does not hinder mesenchymal cluster formation and villi formation. Scale bar = 500 μm. **B.** *Myocardin* knockout in mesenchyme significantly reduces the presence of muscle cells labeled by expression of smooth muscle actin. Despite the lack of muscle layer, PDGFRα expressing mesenchymal cell clusters and corresponding villus formation are observed at E15.5. **C.** E13.5 *Pdgfra*^{EGFP} explant intestinal tissue cultured in control medium and 10 μM Aphidicolin. Tissue after 1 day of culture was fixed and immunostained with Ecad to label epithelium (red). Scale bar = 50 μm. **D.** Cultured explant tissues were assayed for level of proliferation with 2.5 hour incubation with EdU with or without the presence of Aphidicolin. PDGFRα nuclei (green), Ecad (epithelium, magenta), and EdU (proliferation, red). Aphidicolin treated explant tissues have significantly reduced level of cell proliferation. Scale bar = 50 μm.

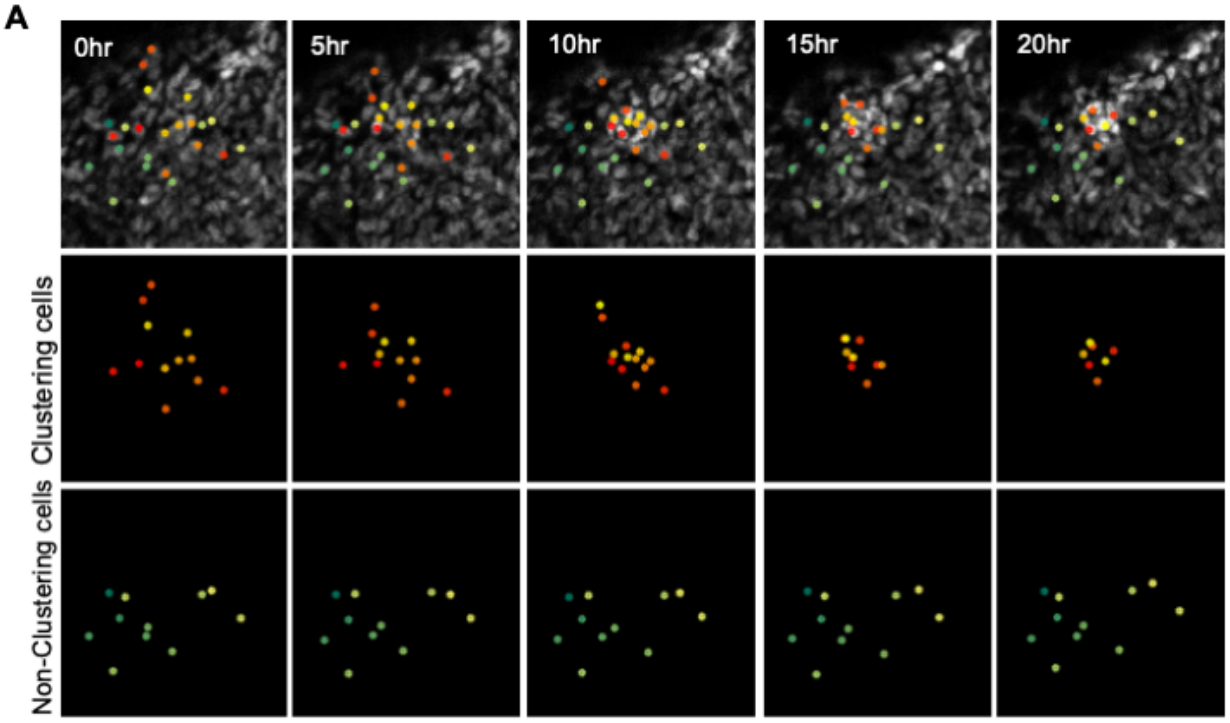
A
0hr
5hr
10hr
15hr
20hr
Clustering cells
Non-Clustering cells

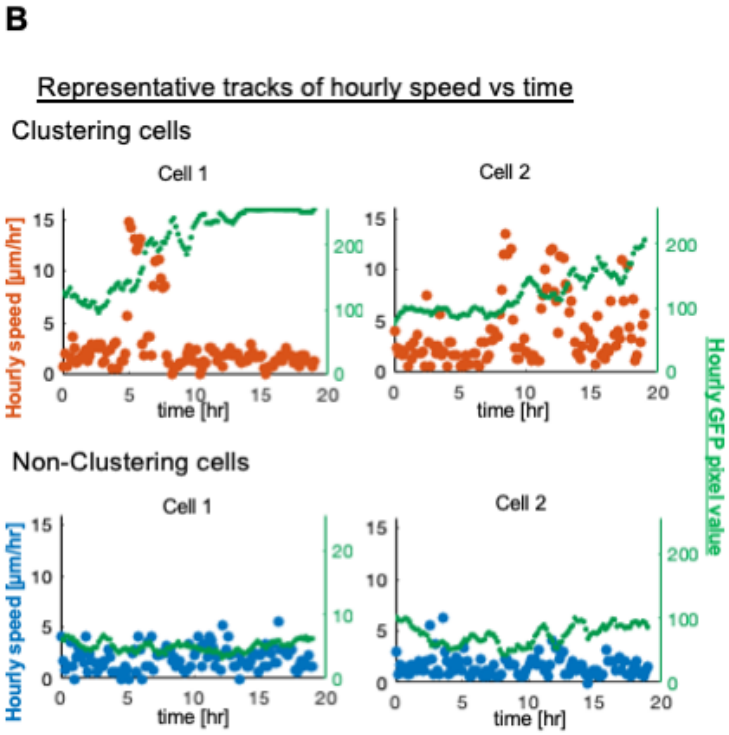
B
Representative tracks of hourly speed vs time
Clustering cells
Cell 1
Cell 2
Hourly speed [μm/hr]
Hourly GFP pixel value
time [hr]
Non-Clustering cells
Cell 1
Cell 2
Hourly speed [μm/hr]
time [hr]

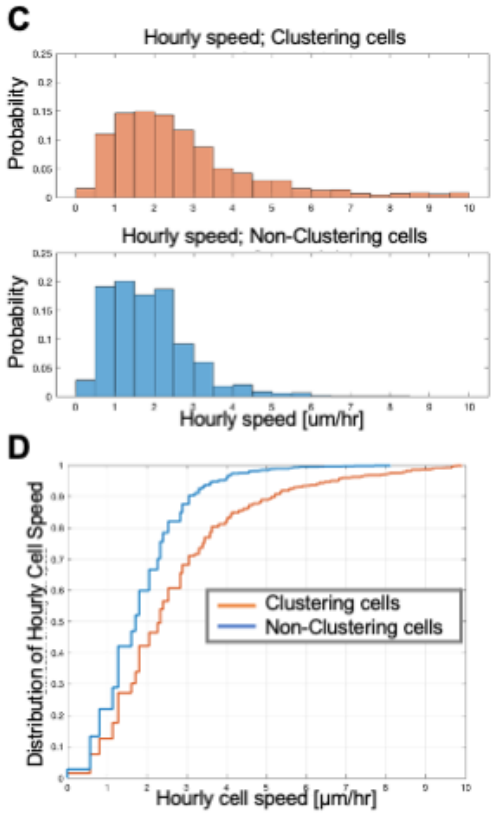
C
Hourly speed; Clustering cells
Probability
Hourly speed; Non-Clustering cells
Probability
Hourly speed [um/hr]
D
Distribution of Hourly Cell Speed
Clustering cells
Non-Clustering cells
Hourly cell speed [μm/hr]

Figure 2.3 Tracking of cell nuclei motion on live imaging data reveal increased motility in PDGFRα^{High} clustering mesenchymal cells. A. Live imaging and tracks of *Pdgfra*^{EGFP} nuclei during the cluster formation. All tracked cells (top), clustering cells (middle), and non-clustering cells (bottom) are shown. Tracked cells are color-labeled. **B.** Representative profile of tracked individual cells. Clustering cells show spikes of high motility among baseline motility, when joining the cluster. Hourly speed [μm/hr] and hourly GFP pixel values were analyzed to minimize noise due to frame-drifts and manual tracking. **C.** Histogram comparing the baseline motility values of clustering cells and non-clustering cells. Hourly speed data points above 10 μm/hr (spikes of high motility) were removed from the clustering-cells' data points to only consider baseline motility. **D.** Cumulative plot displaying baseline hourly speed distribution reveals a right-shifted curve for clustering cell population, indicating that even among baseline motility more proportion of them are moving at a higher motility.

2.2 Single cell sequencing of developing intestine reveal molecular signature suggestive of increased adhesion program at clustering PDGFRα^{High} mesenchymal cells

To understand the molecular programs that drive mesenchymal cell clustering and villus morphogenesis, we conducted single-cell RNA sequencing of intestinal tissues across five developmental time points (**Fig. 2.4**A). Along its length, the intestine not only displays different functions and molecular profiles, but during embryogenesis also represents different stages of development, as villus morphogenesis progresses in a proximal-to-distal wave along the length of the intestine (Haber et al., 2017; Kammeraad, 1942; Walton et al., 2012). Taking advantage of this, we captured these functional regions and developmental pseudotime points along the length of intestines by segmenting tissues into 2.5mm-length pieces that we sequenced with MULTI-seq, a multiplexing sample labeling strategy using lipid modified barcodes (McGinnis et al., 2019b) (**Fig. 2.4**B). As PDGFRα^{High} mesenchymal cells that initiate villus morphogenesis only account for <2.5% of total cells, we enriched for rare cell type populations in addition to collecting unbiased population of all live single cells to ensure that we captured sufficient number of cells of interest (**Fig. 2.4**C). A total of 86,845 cells across 117 MULTI-seq tagged samples among 5 embryonic days passed barcode assignment, quality control and Doublet Finder criteria for further downstream analysis (McGinnis et al., 2019a). The resulting dataset from two different experimental days were integrated for batch correction and visualized using Uniform Manifold Approximation and Projection (UMAP) dimensional reduction (Becht et al., 2019).

Hierarchical clustering and marker gene analysis revealed six major cell types of embryonic mouse intestine, including epithelium, mesenchyme, endothelium, immune cells, mesothelium and enteric nervous system (ENS) cell populations (**Fig. 2.5**A,D, **Table 2.1**). Samples collected on two different experimental days were well-aligned, and the sorted 'enriched' cell populations were observed at expected cluster locations (**Fig. 2.5**B,C). When mesenchymal cell populations were subsetted and analyzed for gene expressions, we identified three principal subtypes of mesenchymal cells – *Acta2*(encoding Alpha Smooth Muscle Actin) expressing muscle cells, a *Bmp4* expressing cell population and a *Ptn* expressing cell population (**Fig. 2.4**E, **2.5**E,F). *Bmp4* is one of the marker genes expressed in the subepithelial population of mesenchyme and subsequently upregulated in villus clusters (Walton et al., 2015). Therefore, we decided to refer to the *Bmp4* expressing population as "subepithelial mesenchymal cells." *Pdgfra*-high expressing cells are included in the subepithelial mesenchymal cell group as expected (**Fig. 2.4**D, **2.5**F).

Further subsetting of subepithelial mesenchymal cells revealed the existence of three major categories of cells: cycling cells, a PDGFRα-High lineage population, and a PDGFRα-low stroma lineage population with increased expression of genes such as *Dcn* and *Rspo3* (**Fig. 2.4**D, **2.5**G-I, **Table 2.2**). The sorted enriched population of *Pdgfra*^{EGFP} GFP-High cells aligned well with the clusters represented by cells with high expression of *Pdgfra* genes, confirming that the expression level of the GFP reported in the *Pdgfra*^{EGFP} embryos correlates well with gene expression (**Fig. 2.4**D, **2.5**J).

When the developmental time points were followed in the enriched PDGFRα^{High} cell population, we observed differentiation trajectories of PDGFRα^{High} cells

transforming from newly emerged differentiated clustering population at E14.5 to PDGFRα^{High} cell population of elongated villi at E18.5 (**Fig. 2.4**F). We additionally performed Principle Component Analysis (PCA) on this cell population, which revealed that PC1 captures gene groups representing this temporal developmental trajectory (**Fig. 2.4**G, **Table 2.3**). When the distribution of this cell population along the length of the intestine was analyzed, the relative location of cells of proximal or distal origin qualitatively aligned with the expected developmental lineage; distal pieces were more enriched in newly differentiated PDGFRα-High 1 cluster cell population, while proximal pieces had increased numbers of further differentiated PDGFRα-High 2 cluster cell populations. (**Fig. 2.4**B, **2.5**K). This region-dependent developmental wave was quantitatively assessed by the PC1 'villus developmental' score (**Fig. 2.4**I). Furthermore, the 'Slingshot' method was used to computationally infer pseudotime trajectories (Street et al., 2018). The tissue developmental stages and cell-cycle trajectories corresponded well with the predicted pseudotime trajectories (**Fig. 2.6**A,B). Along the PDGFRα^{High} lineage trajectory, several genes including *Bmp3* and *Gja1* were upregulated specifically in the nascent and clustering PDGFRα^{High} population (PDGFRα-High 1), while some other genes including *Npnt* and *Fat4* became upregulated in PDGFRα^{High} cell population (PDGFRα-High 2) as villus morphogenesis progressed (**Fig. 2.5**G, **2.6**C,D). This single-cell RNA sequencing dataset is the first to capture the emergence and development of PDGFRα^{High} cell population with spatial and temporal resolution.

To understand the molecular programs that underlie formation of PDGFRα^{High} mesenchymal cell clusters, we performed differential gene expression analysis

comparing PDGFRα^{High} cells (PDGFRα-High 1) and PDGFRα-low subepithelial stroma cells (PDGFRα-low 1). Kyoto Encyclopedia of Genes and Genomes **(**KEGG) biological process analysis of upregulated gene groups identified 'ECM-receptor interaction; KEGG:04512' and 'Focal adhesion; KEGG:04510' as the top upregulated biological programs (**Fig. 2.7**). Specifically, increased expression of some ECM genes such as laminin genes and Collagen 4 and Collagen 6 genes, and ECM-binding receptors such as *Itga1*, *Itga2*, and *Itga11* were observed, contributing to the adhesive signature of PDGFRα^{High} cell population (**Fig. 2.4**I,J). In addition, genes suggestive of Calcium signaling and actomyosin activities were upregulated in the same population (**Fig. 2.4**J). Together, these molecular signatures suggest that clustering PDGFRα^{High} cells display increased cellular adhesion programs.

Epithelial development was also captured in the dataset. Among epithelial cell populations, distinct clusters of differentiated goblet and enteroendocrine cell identities as well as enterocytes population were identified (Haber et al., 2017) (**Fig. 2.8** A,B, **Table 2.4**). Visualization of cell populations along developmental time points revealed that epithelial cell populations start out as a relatively uniform population of progenitor cells, marked by gene expression of *Shh*. Following villus development, epithelial cells start to differentiate into enterocyte identities, characterized by the increased expression of various Fatty-acid binding protein genes (*Fabp*) and apolipoproteins (*Apoa*) (**Fig. 2.8**B,C). This general differentiation trajectory that represents villus development is again manifested in proximal-distal waves along the length of the intestine, suggesting developmental wave is also evident in the epithelial differentiation (**Fig. 2.8**D-F, **Table 2.5**). RNAscope in situ hybridization assay revealed that *Fabp1* expressing epithelial

cells only appear after villus morphogenesis on the villus surface (**Fig. 2.9**A,B). These observations are in agreement with the conclusion suggested by Shyer et al. where they claim epithelial differentiation is a result of villus structure-dependent signaling gradients (Shyer et al., 2015).

One intriguing observation from the epithelial dataset is that differentiated goblet and enteroendocrine cells are present at E13.5 and E14.5, developmental time points before villus morphogenesis (**Fig. 2.8**C, **2.9**A,C,D). This is consistent with the observation noted from the single-cell sequencing of human embryonic intestines (Elmentaite et al., 2020). These results again suggest that secretory cell differentiation may be driven by a mechanism independent of villus morphogenesis, and sources other than classical Lgr5-expressing epithelial stem cells may produce differentiated secretory cell subsets during development (Elmentaite et al., 2020; Guiu et al., 2019).

As differences in cell identity along the length of the intestine could represent regionalization of the intestine in addition to differences due to development, I further analyzed whether or not the molecular signatures corresponding to the regionality of intestines are apparent during development. In both epithelial and mesenchymal population, the proximal-distal axis were observed as a gradient of molecular signature along the anterior to posterior axis independent of developmental trajectory. (**Fig. 2.5**K, **2.10**A,B). PC6 captures gene groups representing the proximal - distal profile that is independent from developmental stages among PDGFRα^{High} cell populations (**Fig. 2.10**C-E, **Table 2.6**).

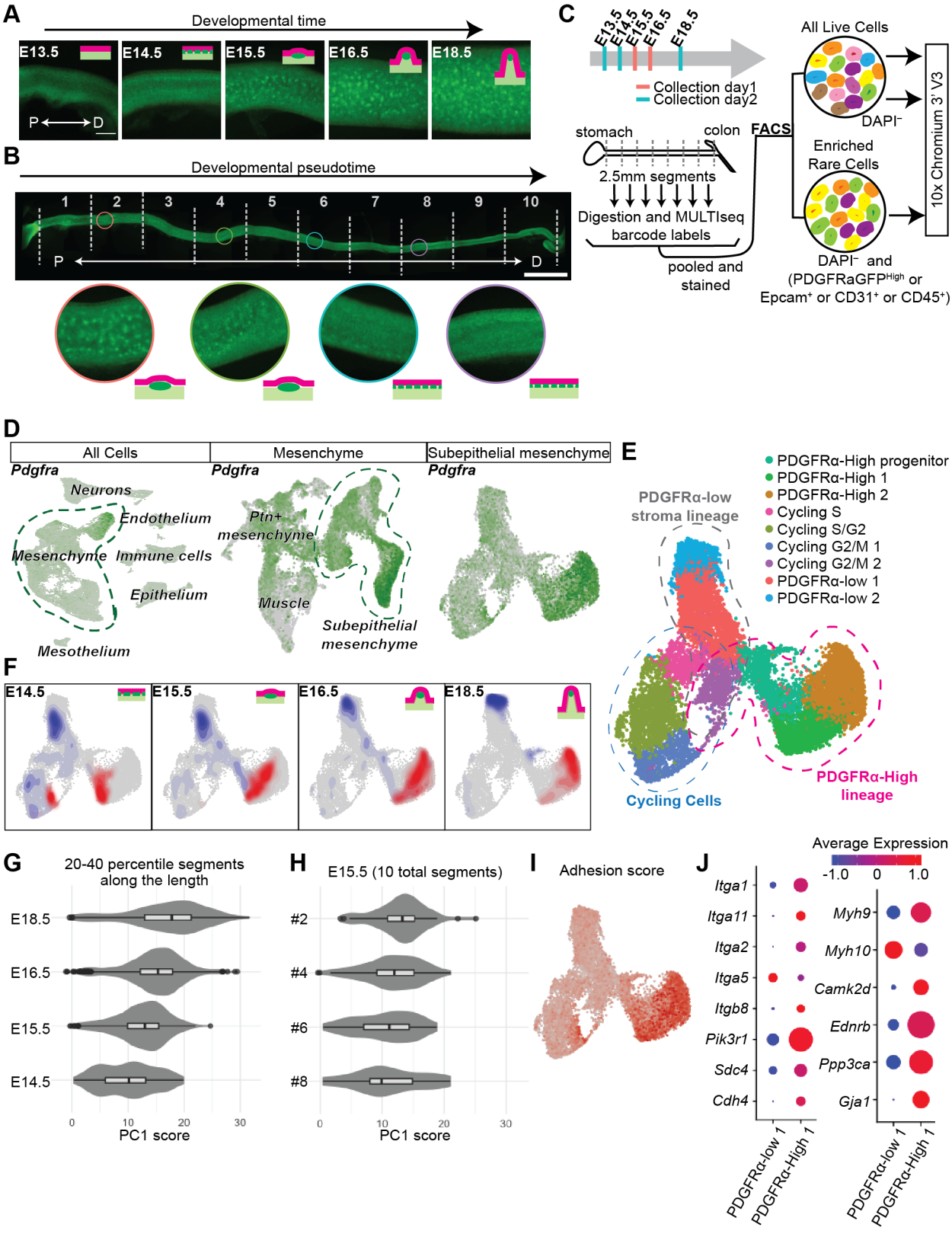
A
Developmental time
E13.5
E14.5
E15.5
E16.5
E18.5
P
D
B
Developmental pseudotime
1 2 3 4 5 6 7 8 9 10
P
D
C
E13.5
E14.5
E15.5
E16.5
E18.5
Collection day1
Collection day2
stomach
colon
FACS
2.5mm segments
Digestion and MULTIseq barcode labels
pooled and stained
All Live Cells
DAPI⁻
Enriched Rare Cells
DAPI⁻ and (PDGFRaGFP^High or Epcam⁺ or CD31⁺ or CD45⁺)
10x Chromium 3' V3
D
All Cells
Mesenchyme
Subepithelial mesenchyme
Pdgfra
Neurons
Endothelium
Mesenchyme
Immune cells
Epithelium
Mesothelium
Ptn+ mesenchyme
Muscle
Subepithelial mesenchyme
E
PDGFRα-High progenitor
PDGFRα-High 1
PDGFRα-High 2
Cycling S
Cycling S/G2
Cycling G2/M 1
Cycling G2/M 2
PDGFRα-low 1
PDGFRα-low 2
PDGFRα-low stroma lineage
Cycling Cells
PDGFRα-High lineage
F
E14.5
E15.5
E16.5
E18.5
G
20-40 percentile segments along the length
E18.5
E16.5
E15.5
E14.5
0 10 20 30
PC1 score
H
E15.5 (10 total segments)
#2
#4
#6
#8
0 10 20 30
PC1 score
I
Adhesion score
J
Average Expression
-1.0 0 1.0
Itga1
Itga11
Itga2
Itga5
Itgb8
Pik3r1
Sdc4
Cdh4
Myh9
Myh10
Camk2d
Ednrb
Ppp3ca
Gja1
PDGFRα-low 1
PDGFRα-High 1
PDGFRα-low 1
PDGFRα-High 1

Figure 2.4 Single-Cell Sequencing of the developing intestine reveals emergence of PDGFRα^{High} cell population that have upregulation of motility and adhesion programs. A. Fluorescent GFP image of *Pdgfra^{EGFP}* intestines used for the experiments of different developmental stages. Scale bar = 200 μm. **B.** Fluorescent GFP image of one of the E15.5 *Pdgfra^{EGFP}* intestines used for the experiment. The tissue was segmented into 2.5 mm pieces. Proximal pieces have mesenchymal cell clusters, while distal pieces have few clusters. Scale bar = 2 mm. **C.** Schematics summarizing the experiment. E13.5 - E18.5 *Pdgfra^{EGFP}* intestinal tissues were collected over 2 different experiments. Tissues were cut into 2.5 mm pieces, digested and labeled with MULTI-seq lipid-modified barcodes. Unmodified proportions of all live cells and populations enriched for PDGFRα^{High} cells, immune cells, endothelial cells and epithelial cells were sorted and captured to single-cell sequencing GEMs using 10x Chromium V3 kits. **D**. Dataset captured and used for the analysis. Mesenchymal cell groups that contain *Pdgfra* expression cells were followed to subset the dataset into subepithelial mesenchymal cell population**. E.** UMAP projection of Bmp4 expressing subepithelial mesenchymal cell populations reveal 3 lineages of cell categories: PDGFRα^{High} cell lineage, PDGFRα^{low} stroma lineage and cell-cycle population**. F.** Distribution of PDGFRα^{High} cell populations at different developmental time points by density plot. **G.** Principal Component 4 (PC4) scores for tissues of different developmental time points. PC4 represents development. **H.** PC4 scores for E15.5 tissues along the length of the intestine (segment 2,4,6 and 8) reveals progression of development at proximal regions **I.** Combined expression of adhesion related KEGG-term genes that are upregulated in PDGFRα-High 1 population. **J.** Specific list of the genes contained in the adhesion-related KEGG terms plotted in I and their expression.

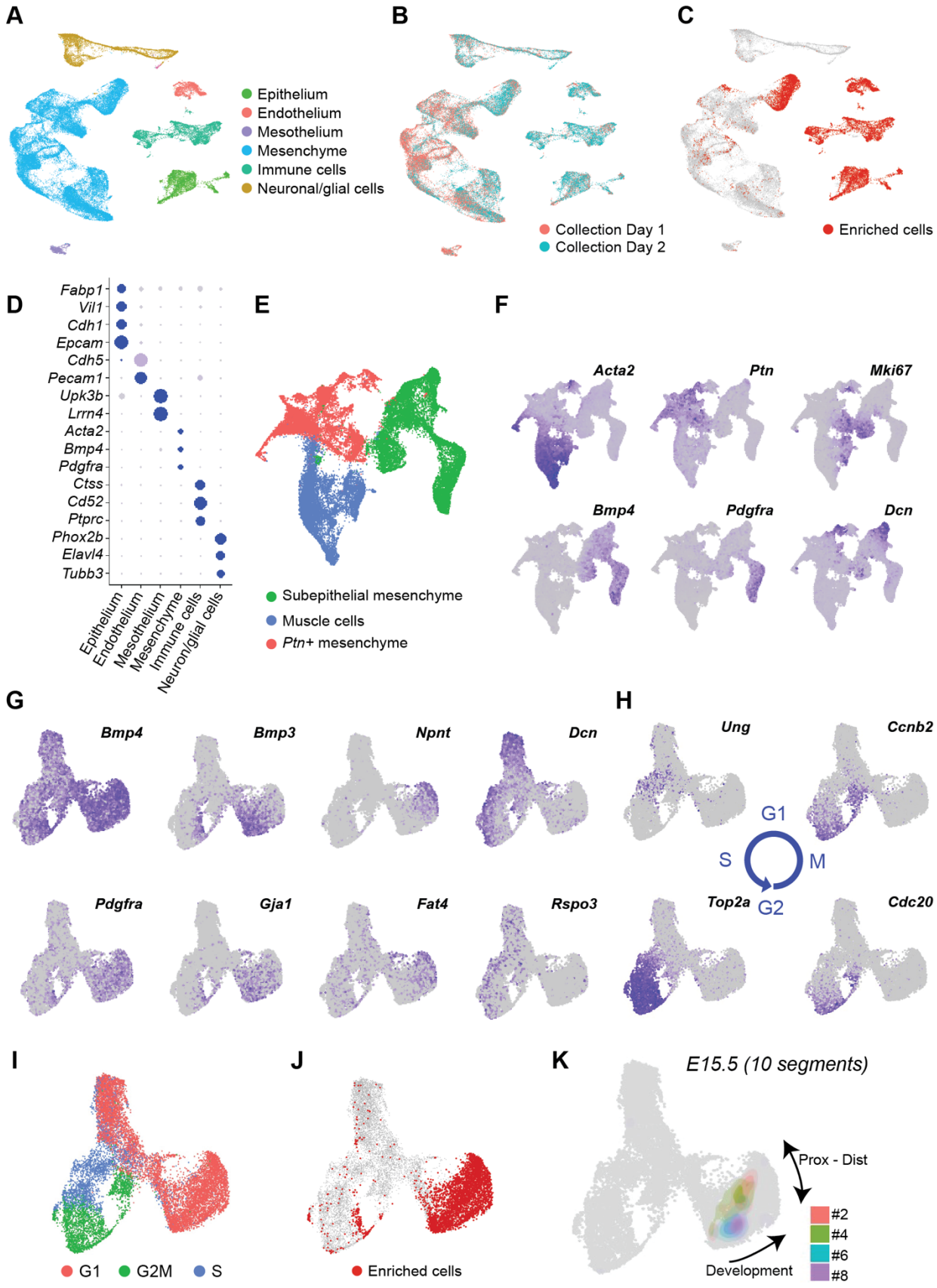
A
Epithelium
Endothelium
Mesothelium
Mesenchyme
Immune cells
Neuronal/glial cells
B
Collection Day 1
Collection Day 2
C
Enriched cells
D
Fabp1
Vil1
Cdh1
Epcam
Cdh5
Pecam1
Upk3b
Lrrn4
Acta2
Bmp4
Pdgfra
Ctss
Cd52
Ptprc
Phox2b
Elavl4
Tubb3
Epithelium
Endothelium
Mesothelium
Mesenchyme
Immune cells
Neuron/glial cells
E
Subepithelial mesenchyme
Muscle cells
Ptn+ mesenchyme
F
Acta2
Ptn
Mki67
Bmp4
Pdgfra
Dcn
G
Bmp4
Bmp3
Npnt
Dcn
Pdgfra
Gja1
Fat4
Rspo3
H
Ung
Ccnb2
G1
S
M
G2
Top2a
Cdc20
I
G1
G2M
S
J
Enriched cells
K
E15.5 (10 segments)
Prox - Dist
Development
#2
#4
#6
#8

Figure 2.5 Overview of single-cell sequencing result A. UMAP projection of all cells collected. **B.** Overlays of two different collection days reveal successful integration of data. **C.** Enriched cell populations overlay to the expected clusters. **D.** Marker genes for each cell types identified. **E.** UMAP projection of Mesenchymal cells reveal three major categories of mesenchymal cell types. **F.** Expression profile of cluster-defining marker genes. *Acta2, Mki67, Bmp4* each represent muscle cells, proliferating population and subepithelial mesenchymal cells. Bmp4 expressing population include PDGFRα^{High} population and *Dcn* expressing PDGFRα^{Low} population. **G.** Expression profile of cluster-defining marker genes of *Bmp4+* subepithelial mesenchymal cell population. PDGFRα^{High} population can be subdivided into a cell population with *Bmp3* and *Gja1* expression and another with *Npnt* and *Fat4* genes. PDGFRα^{Low} population expression of unique sets of genes including *Dcn* and *Rspo3*. **H.** Expression of proliferation marker genes representing different stages of cell-cycle. **I.** Identified cell cycle phase assignment by cell-cycle scoring. **J.** Overlay of PDGFRα^{High} cells in "enriched cell" populations. **K.** Distribution of E15.5 PDGFRα^{High} cell populations at different segments by density plot.

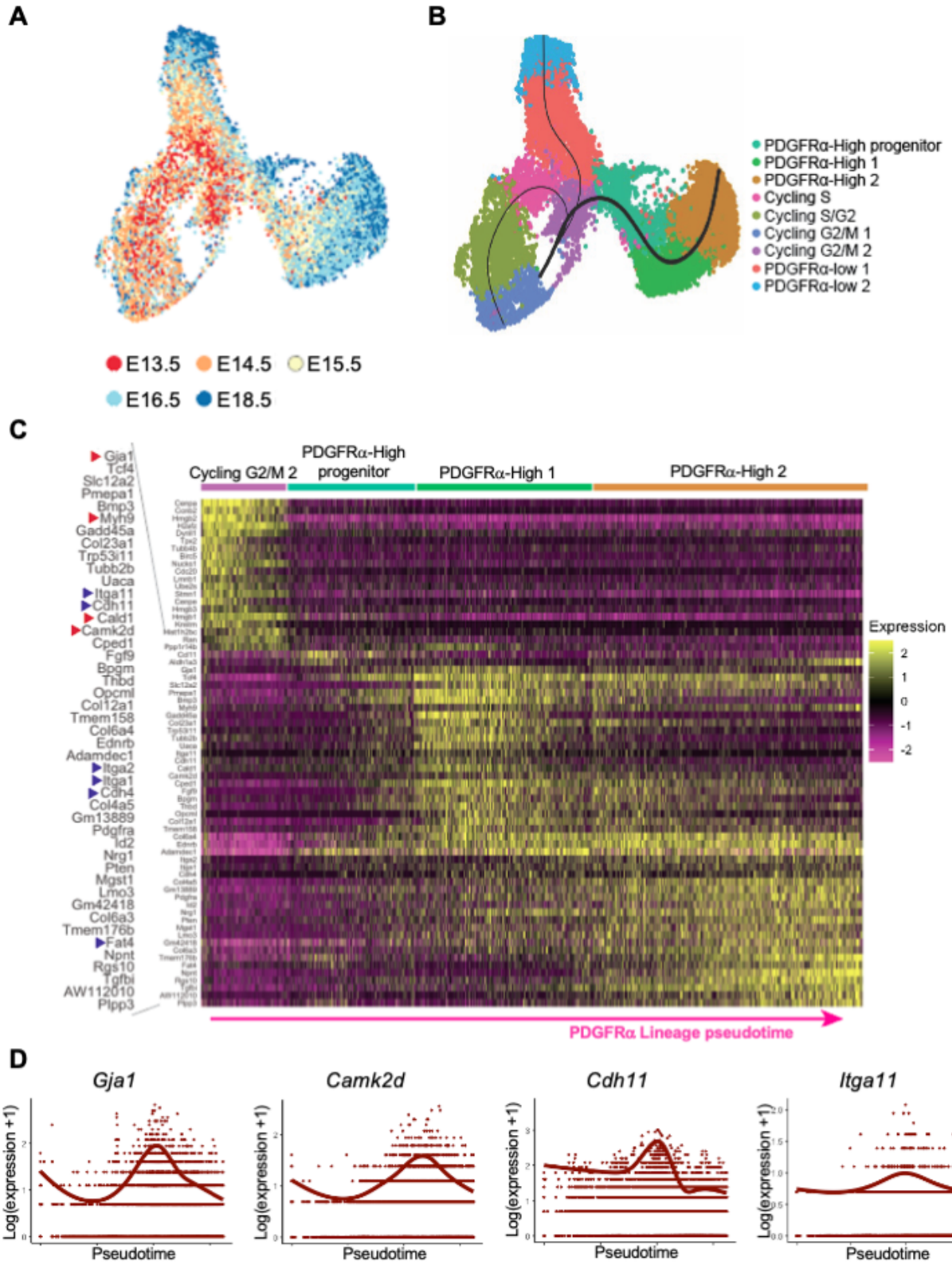
A
B
PDGFRα-High progenitor
PDGFRα-High 1
PDGFRα-High 2
Cycling S
Cycling S/G2
Cycling G2/M 1
Cycling G2/M 2
PDGFRα-low 1
PDGFRα-low 2
E13.5
E14.5
E15.5
E16.5
E18.5
C
Cycling G2/M 2
PDGFRα-High progenitor
PDGFRα-High 1
PDGFRα-High 2
Gja1
Tcf4
Slc12a2
Pmepa1
Bmp3
Myh9
Gadd45a
Col23a1
Trp53i11
Tubb2b
Uaca
Itga11
Cdh11
Cald1
Camk2d
Cped1
Fgf9
Bpgm
Thbd
Opcml
Col12a1
Tmem158
Col6a4
Ednrb
Adamdec1
Itga2
Itga1
Cdh4
Col4a5
Gm13889
Pdgfra
Id2
Nrg1
Pten
Mgst1
Lmo3
Gm42418
Col6a3
Tmem176b
Fat4
Npnt
Rgs10
Tgfbi
AW112010
Plpp3
Expression
2
1
0
-1
-2
PDGFRα Lineage pseudotime
D
Gja1
Camk2d
Cdh11
Itga11
Log(expression +1)
Pseudotime

Figure 2.6 Slingshot analysis revealed pseudotime prediction closely matching the developmental trajectory A. Cell profile distribution based on developmental time point. **B.** Pseudotime trajectories predicted by slingshot analysis reveal three main lineages of cell trajectories. **C.** Heatmap showing marker genes along PDGFRα lineage trajectories reveal groups of contractility associated genes (red arrows) and adhesion related genes (blue arrows) are upregulated in PDGFRα-High cell population. Cells are sorted in order of pseudotime value based on the slingshot analysis. **D.** Example of gene expression profiles along the pseudotime. Genes selected here are Calcium signaling suggestive genes (*Gja1* and *Camk2d*) and adhesion related genes (*Cdh11 and Itga11*) that are specifically upregulated in PDGFRα-High 1 cell population but later downregulated at PDGFRα-High 2 population. TradeSeq workflow together with slingshot analysis were employed to generate the graphs.

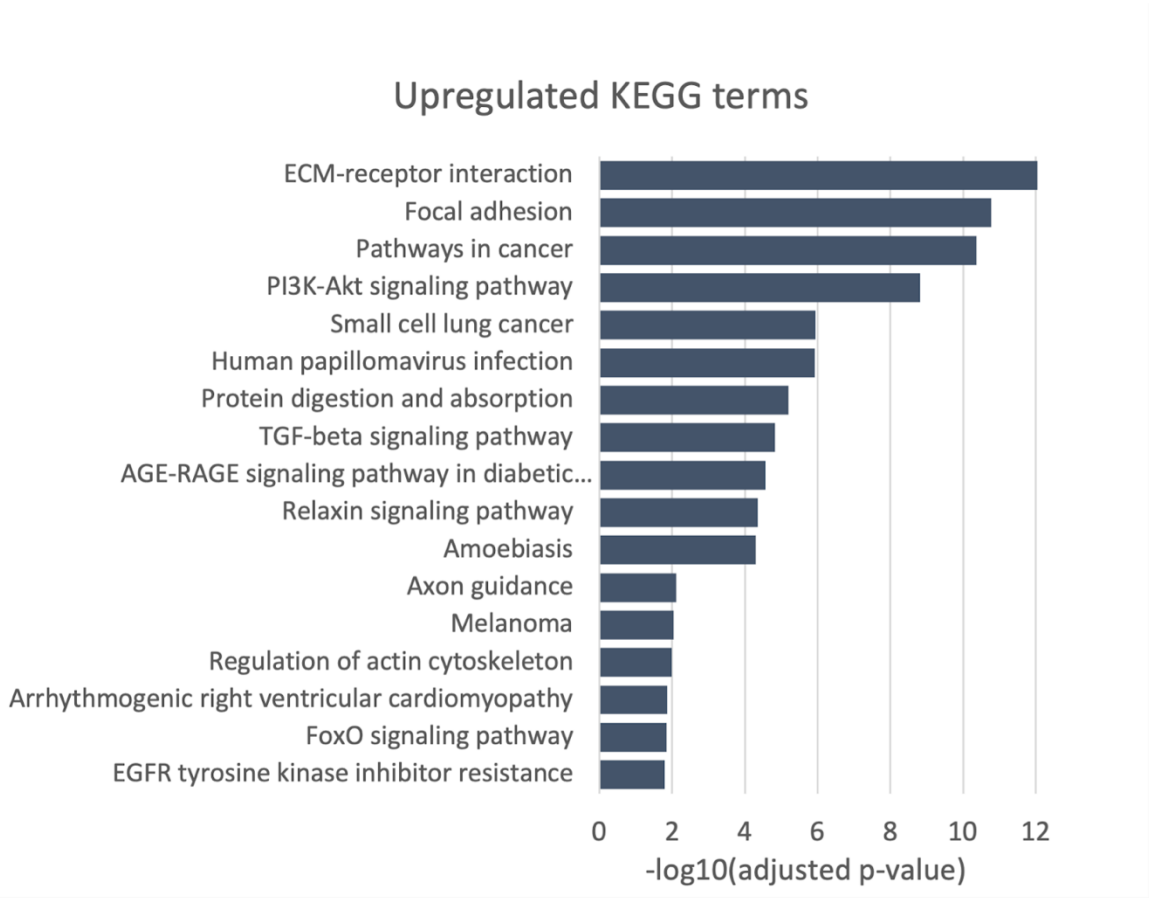

Figure 2.7 Upregulation of cell adhesion programs in PDGFRα^{High} cell populations. KEGG analysis of upregulated genes among PDGFRα-High 1 PDGFRα^{High} clustering cell population in comparison to PDGFRα-low 1 population, suggested ECM-receptor interaction and adhesion as top upregulated programs.

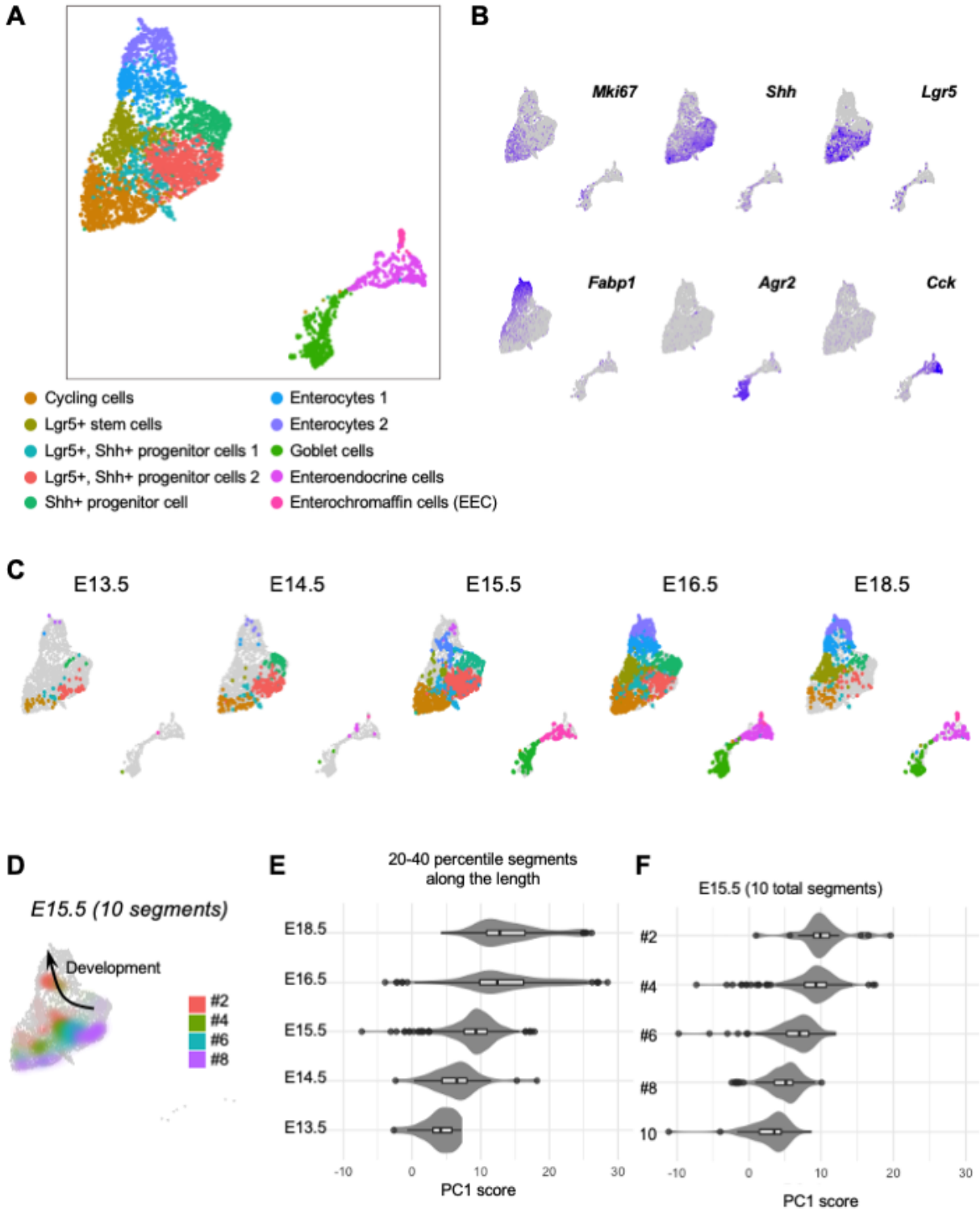
A
B
Mki67
Shh
Lgr5
Fabp1
Agr2
Cck
Cycling cells
Lgr5+ stem cells
Lgr5+, Shh+ progenitor cells 1
Lgr5+, Shh+ progenitor cells 2
Shh+ progenitor cell
Enterocytes 1
Enterocytes 2
Goblet cells
Enteroendocrine cells
Enterochromaffin cells (EEC)
C
E13.5
E14.5
E15.5
E16.5
E18.5
D
E15.5 (10 segments)
Development
#2
#4
#6
#8
E
20-40 percentile segments along the length
E18.5
E16.5
E15.5
E14.5
E13.5
-10
0
10
20
30
PC1 score
F
E15.5 (10 total segments)
#2
#4
#6
#8
10
-10
0
10
20
30
PC1 score

Figure 2.8 Development epithelium cell population is captured in the single-cell RNA sequencing data A. UMAP projection of epithelial cells and identified cell types. **B.** Expression of epithelial marker genes. Each genes mark following population; *Mki67*: proliferating cells, *Shh*: undifferentiated epithelium, *Lgr5*: adult stem cell marker gene, *Fabp1*: enterocytes, *Agr2*: goblet cells, *Cck*: enteroendocrine cells. **C.** Cell population distribution based on developmental time point. **D.** Distribution epithelial cells along the length of the intestine of E15.5 intestine (segment 2, 4, 6 and 8 of 10 segments). **E,F.** PC1 of epithelium represents development-dependent gene groups. PC1 scores across developmental time point (E) and along the length of the E15.5 intestine (F).

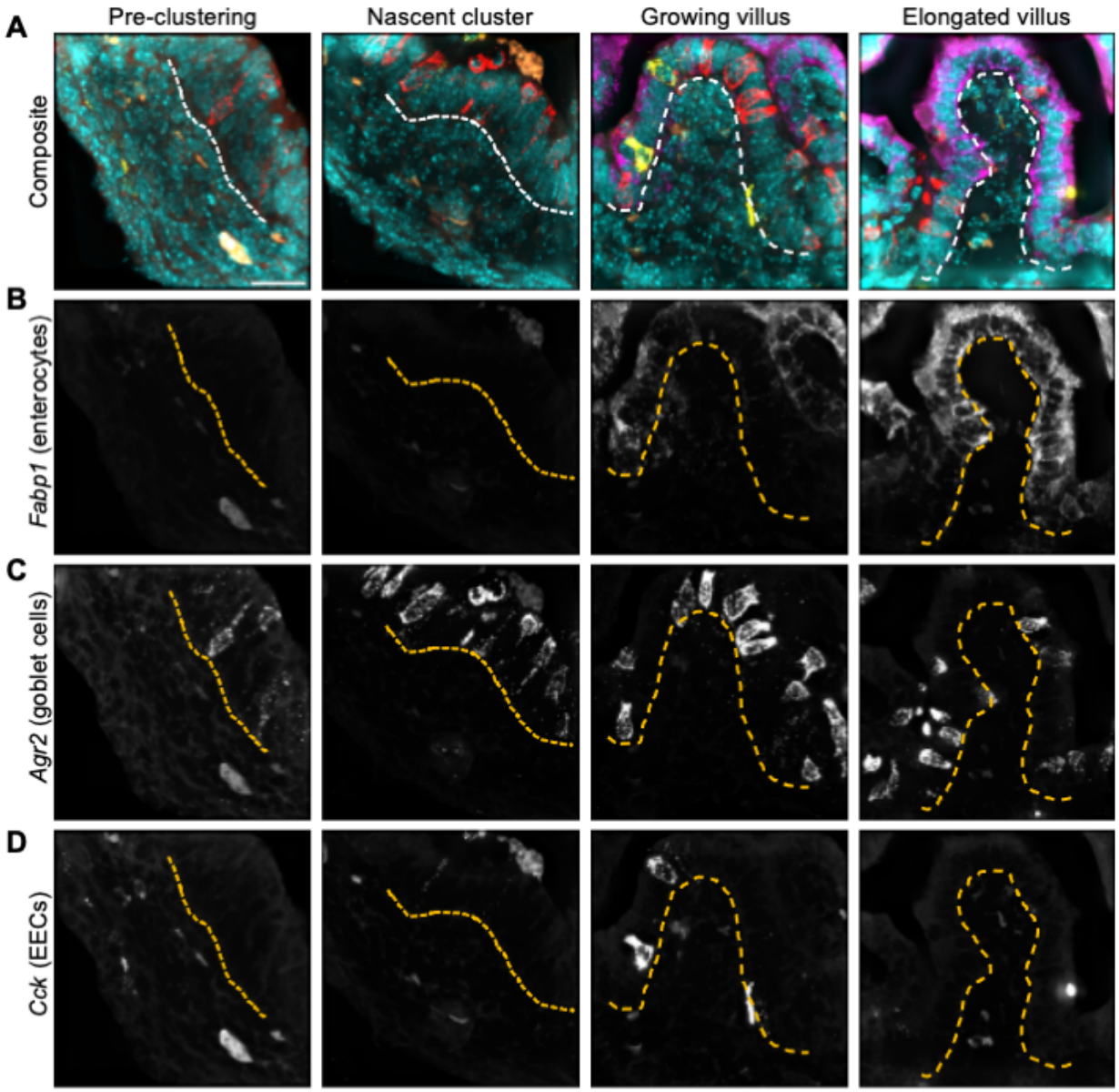

Figure 2.9 *Fabp1, Agr2* and *Cck* expression in developing intestine E15.5 Tissues were probed for the localization of epithelial marker genes using fluorescent in-situ hybridization (RNAscope) methods. Tissue sections representing different stages of villus development (pre-clustering, nascent cluster, growing villus, and elongated villus) are captured. **A.** Composite of all epithelial markers (light blue: DAPI nuclei label, magenta: *Fabp1*, red: *Agr2*, yellow: *Cck*) **B.** *Fabp1* expressions only appear once the villus structure is formed. **C.** Goblet cells are present throughout the villus development. **D.** Enteroendocrine cells were much fewer in comparison to goblet cells.

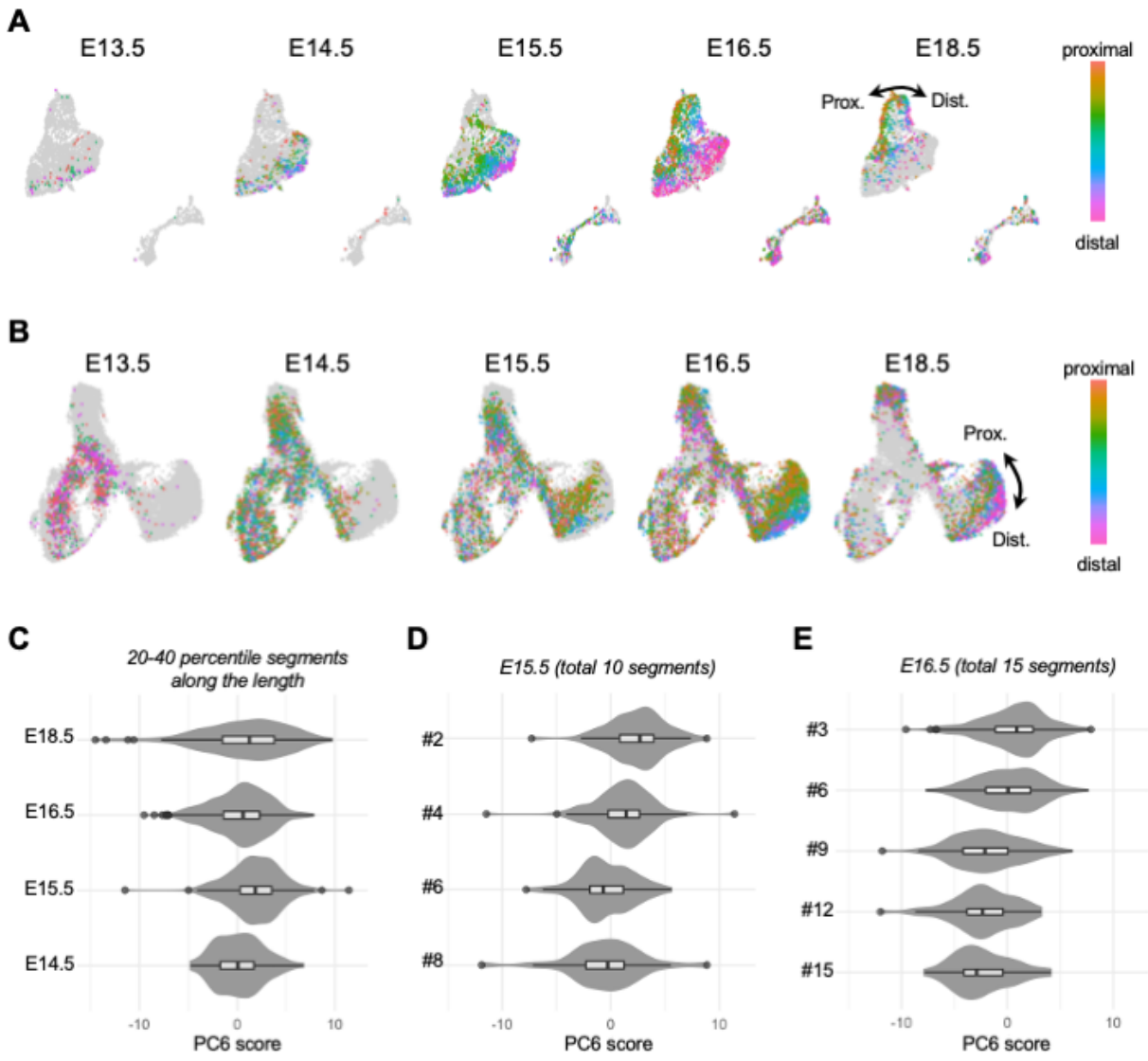

Figure 2.10 Regional-dependent signature of epithelium and mesenchymal cell populations A. Distribution of epithelial cells along the length of the intestine at each developmental time point. **B.** Distribution of Bmp4+ subepithelial mesenchymal cell populations along the length of the intestine at each developmental time point. **C-E.** PC6 of mesenchyme represent region dependent gene groups. C. PC6 scores for tissues of different developmental time points reveal no gradient of distribution along the PC6 axis. D&E. PC6 score for along the length of the intestine of E15.5 intestine (D) and E16.5 intestine (E).

Table 2.1 Markers of embryonic small intestinal cell populations in scRNA-seq data Cell type markers that characterizes each cell-types of the entire dataset.

scRNA-seq Cell-type clusteer markers							
Cell type	gene	avg_log2FC	p_val_adj	Cell type	gene	avg_log2FC	p_val_adj
Epithelium	Fabp1	4.285867	0	Mesenchyme	Col3a1	2.589239	0
	Sct	4.207244	0		Igf2	2.31477	0
	Tff3	4.197383	0		Dlk1	2.268826	0
	Apoa1	4.163874	0		Gas5	2.208026	0
	Fabp2	4.130214	0		Cdkn1c	2.114502	0
	Rbp2	4.10988	0		Rpl13a	2.106748	0
	Lgals4	4.058737	0		Ccn1	1.978542	0
	Apoa4	4.042177	0		Sfrp1	1.953477	0
	Nts	3.991806	0		Tcf21	1.917538	0
	Lypd8	3.794897	0		Meis2	1.895044	0
	Epcam	3.694602	0		Gm42418	1.853882	0
	Krt8	3.676246	0		Nme2	1.849648	0
	Ghrl	3.560732	0		Mdk	1.848865	0
	Spink4	3.516768	0		Nedd4	1.840155	0
	Cldn7	3.494444	0		Serpinh1	1.831318	0
	Defa24	3.451939	0		Acta2	1.83079	0
	Pyy	3.324488	0		Col1a2	1.824679	0
	Lgals2	3.306076	0		Myh11	1.795029	0
	Fcgbp	3.296263	0		Hmga2	1.794236	0
	Apoc2	3.296241	0		Grb10	1.767482	0
Endothelium	Fabp4	4.192482	0	Immune cells	Apoe	4.405238	0
	Cdh5	3.280208	0		Cd74	3.987224	0
	Ccl21a	3.25639	0		C1qb	3.52498	0
	Pecam1	3.063148	0		C1qa	3.502783	0
	Egfl7	2.957805	0		C1qc	3.460444	0
	Cldn5	2.825103	0		Ctss	3.35368	0
	Mest	2.784845	0		Fcer1g	3.28895	0
	Ramp2	2.736028	0		Il1b	3.26303	0
	Kdr	2.703683	0		Cxcl2	3.256845	0
	Plvap	2.647565	0		Tyrobp	3.143059	0
	Cav1	2.637059	0		Pf4	3.141384	0
	Gng11	2.558333	0		H2-Aa	2.944911	0
	Ptprb	2.543505	0		Mrc1	2.827373	0
	Col18a1	2.52183	0		Tmsb4x	2.810097	0
	Tm4sf1	2.465351	0		Cd52	2.753096	0
	Cd93	2.452975	0		Srgn	2.743998	0
	Flt1	2.435195	0		Laptm5	2.7319	0
	Icam2	2.347931	0		Ctsb	2.725555	0
	Crip2	2.317123	0		Ccl4	2.720693	0
	Igfbp3	2.272473	0		Lcp1	2.685571	0
Mesothelium	Upk3b	3.910498	0	Neuronal/ glial cells	Phox2b	3.449644	0
	Igfbp5	2.555097	0		Tubb3	3.263607	0
	Arhgap29	2.544179	0		Tuba1a	3.112366	0
	Dcn	2.532611	0		Dpysl3	3.075464	0
	Krt19	2.460253	0		Ascl1	2.850704	0
	Ezr	2.408734	0		Gap43	2.818234	0
	Krt7	2.388593	0		Uchl1	2.61744	0
	Podxl	2.372766	0		Hand2os1	2.556472	0
	Fbln2	2.361823	0		Nefm	2.536065	0
	Igf2	2.34594	0		Elavl4	2.523713	0
	Peg3	2.308936	0		Tlx2	2.477556	0
	Col18a1	2.288142	0		Rbp1	2.423625	0
	Bcam	2.201102	0		Rtn1	2.392393	0
	Aldh1a2	2.165245	0		Map1b	2.285773	0
	Nnat	2.120905	0		Ppp1r14b	2.267614	0
	Npnt	2.010597	0		Hoxb5	2.236201	0
	Alcam	2.004733	0		Tubb2b	2.21112	0
	Aprt	1.996029	0		Ccnd1	2.164054	0
	Sparc	1.995593	0		Phox2a	2.137009	0
	Net1	1.96222	0		Syt1	2.091264	0

Table 2.2 Cluster markers of subepithelial mesenchymal cell populations Cell cluster markers identified by differential expression analysis using FindMarkers in Seurat among the subepithelial mesenchymal cell population.

scRNA-seq Subepithelial mesenchyme cluster markers

Cluster	gene	avg_log2FC	p_val_adj
PDGFRa-High progenitor	Ccl11	1.167016	1.35E-155
	Aldh1a3	0.722527	4.57E-32
PDGFRa-High 1	Bmp3	1.662085	0
	Gadd45a	1.628162	0
	Pmepa1	1.505518	0
	Cped1	1.223912	0
	Tcf4	1.182739	0
	Fgf9	1.16335	0
	Bpgm	1.08771	0
	Col6a4	1.077857	0
	Col23a1	1.049362	0
	Ednrb	1.025384	0
	Thbd	1.012736	0
	Slc12a2	0.993955	0
	Opcml	0.929916	0
	Trp53i11	0.928764	0
	Gja1	0.899684	0
	Hgf	0.794397	0
	Bmp2	0.856868	4.54E-294
	Adamdec1	0.85945	2.79E-293
	Procr	0.825039	7.00E-268
	Emid1	0.841749	1.40E-249
PDGFRa-High 2	Adamdec1	2.120887	0
	Npnt	2.096345	0
	Ednrb	1.654149	0
	Col4a5	1.597748	0
	Rgs10	1.572475	0
	Col6a4	1.563008	0
	Gm13889	1.491628	0
	Pdgfra	1.443911	0
	Id2	1.416896	0
	Slco2a1	1.329055	0
	Tgfbi	1.319518	0
	Nrg1	1.307447	0
	AW112010	1.298404	0
	Pten	1.265932	0
	Plpp3	1.2533	0
	Mgst1	1.224259	0
	Lmo3	1.221355	0
	Col6a3	1.217236	0
	Nid1	1.106854	0
	Tcf4	1.080314	0
Cycling S	Hells	1.386786	0
	Cdc6	0.973085	0
	Ung	0.865994	0
	Ccne2	1.02764	5.08E-294
	Lig1	1.432352	1.68E-290
	Mcm7	1.458573	4.50E-286
	Uhrf1	1.244966	3.24E-274
	Slfn9	1.025869	1.77E-273
	Mcm5	1.09311	2.47E-260
	Mcm3	1.356429	1.79E-254
	Clspn	0.965388	1.19E-249
	Dhfr	0.912337	1.68E-246
	Fam111a	0.963212	4.42E-245
	Gins2	0.937629	4.13E-242
	Mcm6	1.210679	4.93E-232
	Gmnn	1.07648	1.13E-229
	Chaf1b	0.762785	3.82E-219
	Rrm2	1.054339	2.66E-213
	Dtl	0.877726	3.25E-205
	Chaf1a	0.896619	1.16E-203

Custer	gene	avg_log2FC	p_val_adj
Cycling S/G2	Hist1h1b	3.050118	0
	Hist1h2ap	2.808018	0
	Hist1h2ae	2.766896	0
	Pclaf	2.627021	0
	Top2a	2.27861	0
	Hist1h1e	1.830695	0
	Hist1h1a	1.742025	0
	Lig1	1.701708	0
	Hmgb2	1.671967	0
	Mki67	1.578145	0
	Atad2	1.565373	0
	Dek	1.543328	0
	Tyms	1.527555	0
	Rrm2	1.46666	0
	Tuba1b	1.442271	0
	Stmn1	1.42005	0
	Smc2	1.420002	0
	Pcna	1.331111	0
	H2afz	1.313234	0
	Tubb5	1.309862	0
Cycling G2/M 1	Ube2c	3.182842	0
	Cenpf	2.847987	0
	Top2a	2.513591	0
	Prc1	2.500204	0
	Arl6ip1	2.485739	0
	Nusap1	2.482414	0
	Cenpa	2.195904	0
	H2afx	2.125119	0
	Cenpe	2.090166	0
	Hmgb2	2.044216	0
	Mki67	2.014059	0
	Cks2	2.007529	0
	Tubb4b	1.983305	0
	Tpx2	1.91041	0
	Hmmr	1.872123	0
	Cdc20	1.85766	0
	Birc5	1.827935	0
	Ccnb1	1.775567	0
	Cdca8	1.730757	0
	Cdk1	1.668875	0
Cycling G2/M 2	Cenpa	1.811437	0
	Ccnb2	1.419551	0
	Knstrn	0.913318	4.92E-259
	Hist1h2bc	0.947553	1.38E-256
	Hmgb1	0.916444	1.51E-221
	Nucks1	1.080594	3.17E-206
	Cenpf	0.759516	5.26E-190
	Birc5	0.945106	2.03E-186
	Hmgb2	1.094831	6.55E-186
	H2afz	1.195972	1.16E-178
	Dynll1	1.097363	4.29E-177
	Cdc20	0.866913	1.59E-171
	Cdca8	0.729839	1.68E-170
	Tpx2	0.844113	2.68E-166
	Cdca3	0.743967	7.71E-165
	Tubb4b	1.030946	2.59E-153
	Cenpe	0.819176	1.40E-141
	Stmn1	0.885237	1.88E-130
	Selenoh	0.788388	8.21E-118
	Ube2s	0.964806	1.08E-116

Custer	gene	avg_log2FC	p_val_adj
PDGFRa-low 1	Lsp1	0.794891	7.25E-298
	Zeb2	0.713634	1.26E-264
	Ccnd2	0.764432	5.86E-219
	Dlk1	0.731844	5.41E-202
	Acta2	0.742136	1.40E-152
PDGFRa-low 2	Dcn	2.888231	0
	Cxcl13	2.770519	0
	Col1a1	2.366009	0
	Ogn	2.305453	0
	Mfap4	2.135734	0
	Sparc	2.015377	0
	Aspn	1.970902	0
	Col1a2	1.957857	0
	Dpt	1.735959	0
	Fibin	1.652193	0
	Ccdc80	1.474922	0
	Lox	1.370919	0
	Svep1	1.271537	0
	Adamts19	1.049741	0
	Fndc1	1.014941	0
	Prss35	0.706289	0
	Col14a1	1.662731	5.60E-295
	Thbs2	1.22183	3.65E-271
	Aebp1	1.111429	1.04E-270
	Shisa3	1.031839	2.47E-270

Table 2.3 Top 100 and Bottom 100 loadings of PC1 component among the subepithelial mesenchymal cell populations PC1 represented the developmental trajectories of PDGFRα^{High} cell populations. Loadings on PC1 are summarized in the table.

Top 100 PC1 loadings			
gene	loading	gene	loading
Adamdec1	0.1351	Col6a2	0.0412
Ednrb	0.1162	Gadd45a	0.0411
Tcf4	0.1075	Col4a1	0.0408
Col6a4	0.1026	Gm26532	0.0400
Pmepa1	0.0729	Tmem176b	0.0400
Meg3	0.0714	Nid1	0.0399
Nrg1	0.0702	Fbn2	0.0386
Gm13889	0.0695	Gja1	0.0385
Rgs10	0.0694	Olfm1	0.0383
Lmo3	0.0682	Sema6a	0.0383
Cped1	0.0677	Plpp3	0.0382
Slc12a2	0.0658	Synpo2	0.0382
Npnt	0.0625	Smoc1	0.0381
Id2	0.0615	Kif26b	0.0378
Mgst1	0.0613	Pik3r1	0.0373
Cdkn1c	0.0607	Rpl27a	0.0373
Tsc22d1	0.0574	Aldh1a2	0.0373
Id3	0.0569	Lamc1	0.0373
Fgf9	0.0568	Col4a2	0.0364
Pdgfra	0.0566	Enho	0.0362
Col4a5	0.0566	Runx1	0.0361
Bmp3	0.0563	Nbl1	0.0360
Tgfbi	0.0558	Adamts18	0.0359
Bmp2	0.0554	Lamb1	0.0359
Ptch1	0.0553	Hrc	0.0355
Id1	0.0524	Ndufa4l2	0.0354
Neat1	0.0505	Elovl7	0.0352
Bmp4	0.0502	Malat1	0.0351
mt-Co3	0.0498	Zbtb20	0.0345
Pten	0.0495	Itm2b	0.0343
Col23a1	0.0495	Hk2	0.0343
Emid1	0.0476	Camk2d	0.0343
Lama5	0.0469	Fry	0.0342
Hbb-bs	0.0469	Glp2r	0.0341
Bpgm	0.0463	Trp53i11	0.0340
Col6a1	0.0455	Opcml	0.0337
Col6a3	0.0449	Itga2	0.0337
Tmem158	0.0449	Mmp2	0.0332
mt-Atp6	0.0445	Angptl6	0.0331
Pcsk6	0.0435	Hbb-bt	0.0329
Slco2a1	0.0429	Eps8	0.0326
Thbd	0.0428	Robo2	0.0325
Dach1	0.0427	Xist	0.0322
AW112010	0.0426	Myh9	0.0320
Foxq1	0.0424	Sema3f	0.0317
Aldoa	0.0420	Tshz2	0.0316
Ramp1	0.0418	Bnip3	0.0314
Ppp3ca	0.0418	Adamts9	0.0311
Col12a1	0.0416	Col4a6	0.0309
Vegfa	0.0413	Tbx3	0.0309

Bottom 100 PC1 loadings			
gene	loading	gene	loading
Top2a	-0.2108	Lgals1	-0.0474
Hmgb2	-0.1646	Sgo1	-0.0468
Pclaf	-0.1364	Ccdc34	-0.0465
Hist1h2ae	-0.1261	Smc4	-0.0462
Nusap1	-0.1010	Cenpe	-0.0458
Ube2c	-0.0992	Ogn	-0.0456
Col1a1	-0.0962	Ube2s	-0.0456
Stmn1	-0.0918	Ran	-0.0454
H2afz	-0.0906	Ppia	-0.0453
Hmgb1	-0.0902	Rpsa	-0.0451
Dcn	-0.0882	Rps8	-0.0434
Prc1	-0.0872	Lmnb1	-0.0431
Tuba1b	-0.0868	Cdca3	-0.0429
Cenpf	-0.0867	Ccne2	-0.0423
Birc5	-0.0850	Ranbp1	-0.0423
Hist1h1b	-0.0816	Ccnb2	-0.0420
Lig1	-0.0760	Ccna2	-0.0417
Lsp1	-0.0756	Pbk	-0.0411
Ptn	-0.0741	H2afv	-0.0411
Dek	-0.0719	Rps12	-0.0410
Sparc	-0.0697	Tubb4b	-0.0408
Col14a1	-0.0678	Hist1h2ab	-0.0407
Cenpa	-0.0678	Cenpw	-0.0407
Zeb2	-0.0661	Pola1	-0.0405
Ptma	-0.0658	Cenph	-0.0402
Tubb5	-0.0657	Cdc20	-0.0401
Rpl41	-0.0635	S100a10	-0.0400
Cks2	-0.0616	Anp32b	-0.0399
Cdca8	-0.0609	Cenpm	-0.0393
H2afx	-0.0608	Fbln1	-0.0393
Mki67	-0.0605	Mis18bp1	-0.0392
Nucks1	-0.0595	Tyms	-0.0390
Col3a1	-0.0584	Spc24	-0.0389
Cxcl13	-0.0575	Ckap2l	-0.0382
Tpx2	-0.0565	Tmpo	-0.0381
Marcks	-0.0561	Meis2	-0.0380
Arl6ip1	-0.0557	Tacc3	-0.0375
Ckap2	-0.0538	G2e3	-0.0374
Spc25	-0.0530	Selenoh	-0.0373
Cdk1	-0.0529	Knl1	-0.0372
Smc2	-0.0513	Kif23	-0.0366
Ccnb1	-0.0512	Acta2	-0.0365
Hmmr	-0.0511	Kif11	-0.0364
Itm2a	-0.0504	Esco2	-0.0363
Mcm7	-0.0493	Aurkb	-0.0362
Racgap1	-0.0490	Rrm2	-0.0361
Incenp	-0.0486	Cks1b	-0.0358
Hjurp	-0.0485	Gmnn	-0.0357
Lockd	-0.0483	Dbf4	-0.0356
Dlk1	-0.0483	Tk1	-0.0355

Table 2.4 Cluster markers of epithelium populations Top 20 Cell cluster markers identified by differential expression analysis using FindMarkers in Seurat among the epithelium population.

scRNA-seq Epithelial cluster markers

Cluster	gene	avg_log2FC	p_val_adj
Cycling cells	Top2a	2.504116	0
	Hist1h2ae	2.420876	0
	Hist1h1b	1.998599	0
	Prc1	1.478704	0
	Cdk1	1.305555	0
	Hist1h2ab	0.91386	0
	Pclaf	1.86334	1.29E-300
	Nusap1	1.631188	3.30E-300
	Esco2	0.84543	1.50E-279
	Tubb5	1.307321	7.55E-275
	Tuba1b	1.253828	1.45E-268
	Incenp	1.063305	4.74E-268
	Pbk	0.909908	1.79E-267
	Aurkb	0.836599	2.41E-266
	Fbxo5	0.892123	3.80E-264
	Mis18bp1	0.833098	5.08E-262
	Spc25	0.97462	5.94E-256
	Sgo1	0.901003	4.40E-243
	Aurka	0.900091	4.44E-242
	Ube2c	1.760053	6.75E-233
Lgr5+ stem cells	Jaml	1.347936	2.37E-136
	Cps1	1.543606	5.14E-133
	Olfm4	1.613951	3.87E-104
	Hspe1	0.630618	6.57E-102
	Ppp1r1b	1.089755	1.55E-100
	Pycard	1.14549	2.24E-99
	Prap1	0.975795	7.82E-93
	Pglyrp1	1.174536	3.36E-87
	Tomm5	0.709816	3.85E-85
	Atp5g1	0.562769	9.07E-85
	Dmbt1	1.760653	2.10E-84
	Cox7b	0.612855	2.38E-83
	Ptma	0.619019	2.85E-82
	Atp5j2	0.498933	8.03E-79
	Clca3b	0.719874	1.77E-78
	Rps2	0.479931	2.46E-78
	Ccl25	1.148817	2.72E-77
	Hspd1	0.838815	2.98E-77
	Atp5k	0.531455	1.74E-76
	Aldh1b1	0.91554	2.25E-76
Lgr5+, Shh+ progenitor cells 1	H19	1.744411	2.91E-69
	Gm42418	1.911437	1.23E-55
	Gm47283	0.770977	4.39E-37
	Eef2	0.547979	2.19E-35
	mt-Cytb	0.517425	5.22E-30
	mt-Nd4	0.434213	4.47E-23
	mt-Nd2	0.518535	7.46E-22
	Rpl4	0.3351	4.95E-19
	Trim2	0.497178	6.75E-19
	mt-Nd1	0.406192	1.16E-17
	Gm26917	2.027787	2.72E-17
	Hmga1b	0.478185	1.11E-16
	Eef1g	0.33998	1.58E-16
	Smarca4	0.441748	2.41E-14
	Snhg9	0.455852	2.62E-14
	Ssrp1	0.409066	2.99E-14
	Mybbp1a	0.440944	7.06E-14
	Eif3b	0.394607	1.73E-13
	Tkt	0.324486	4.35E-13
	mt-Atp6	0.299386	9.06E-13
Lgr5+, Shh+ progenitor cells 2	Rpl27a	0.397894	3.48E-149
	Bex1	1.060997	2.31E-142
	Npm1	0.771006	7.96E-135
	Hsp90ab1	0.521958	3.56E-131
	Snrpg	0.55779	6.13E-123
	Rplp1	0.383394	2.88E-122
	Hmgn1	0.708462	4.33E-116
	Bex4	0.73771	4.78E-116
	Mif	0.623615	7.02E-114
	Ncl	0.700754	5.84E-113
	Rps26	0.348264	8.78E-111
	Rplp2	0.33193	1.79E-109
	Rpl12	0.4053	2.28E-108
	Set	0.684531	1.93E-107
	Hmgb1	0.613565	1.96E-106
	Rpl37	0.319335	1.55E-105
	Rpl6	0.354003	5.60E-102
	Shh	0.717427	7.89E-102
	Rps21	0.315047	1.64E-101
	Rps20	0.367629	2.98E-101

Custer	gene	avg_log2FC	p_val_adj
Shh+ progenitor cells	2610528A11Rik	1.07833	5.56E-80
	Lmo4	1.040998	1.70E-78
	S100a6	1.355469	2.60E-74
	Atf3	1.702282	1.01E-72
	Edn1	2.419488	7.03E-71
	Ahnak	0.967859	1.64E-61
	Anxa2	0.764634	6.59E-60
	Hbegf	0.986704	1.68E-58
	Tmsb4x	0.590586	4.81E-58
	Cbln2	0.801742	9.57E-57
	Klf6	1.184818	1.56E-52
	Krt19	0.614423	1.80E-50
	2200002D01Rik	0.711953	2.14E-50
	Pdzk1ip1	0.667302	1.54E-46
	Rps27	0.268692	1.15E-44
	Actg1	0.667264	1.91E-44
	S100a11	0.848548	4.78E-44
	Rps28	0.25308	9.19E-44
	Cxcl16	0.406315	1.92E-43
	Tmsb10	0.431054	2.28E-43
Enterocytes 1	Apoa1	1.077997	3.97E-128
	2200002D01Rik	1.215879	1.66E-118
	St3gal4	1.285876	7.65E-108
	Ace2	1.046466	5.39E-102
	Maf	1.271832	1.53E-101
	Dbi	1.056242	1.06E-100
	Pycard	1.270025	5.86E-97
	Gstm3	1.292091	5.13E-92
	Gna11	1.091725	1.92E-91
	Mttp	1.079886	9.19E-88
	Slc51a	1.093686	2.18E-87
	Apoc3	0.709986	2.53E-87
	Adh1	0.962852	1.05E-86
	Lypd8	1.309962	1.70E-86
	Chchd10	0.838028	7.56E-84
	Tfec	0.753416	7.67E-82
	Slc7a9	0.914589	5.54E-80
	Ndrg1	1.01106	3.95E-77
	Gm21885	0.678094	4.58E-77
	Uqcr11	0.584387	3.37E-76
Enterocytes 2	Lct	3.140219	0
	Creb3l3	2.774708	0
	Gda	2.695423	0
	Tdrp	1.945445	0
	Gsta2	1.863992	0
	Mafb	1.791513	0
	F10	1.629418	0
	Pdzk1	1.549192	0
	Slc2a2	1.147023	0
	2010003K11Rik	0.954089	0
	Ifit1bl2	1.797714	1.24E-297
	Gm21885	1.573953	6.73E-280
	Fcgrt	3.579355	1.83E-273
	Adh1	2.344109	1.06E-268
	Ace2	2.712998	4.79E-268
	Leap2	2.188993	1.80E-266
	Alpi	2.412063	4.00E-266
	Clec2h	2.409865	3.46E-265
	Gm2061	1.096823	3.87E-262
	Tm6sf2	1.479124	1.91E-261
Goblet cells	Spink4	6.850747	0
	Defa24	6.138973	0
	Defa17	5.584975	0
	Agr2	5.57181	0
	Fcgbp	5.523441	0
	Guca2a	4.639237	0
	Clca1	4.295438	0
	Muc2	4.009643	0
	Ccl9	3.27683	0
	Selenom	3.106834	0
	Tpsg1	2.566646	0
	Klk1	2.274998	0
	Creb3l1	2.138872	0
	Spdef	1.834484	0
	Ramp1	1.786264	0
	Gcnt3	1.710695	0
	Hepacam2	1.674058	0
	Rep15	1.634431	0
	Galnt12	1.593234	0
	Fut2	1.513893	0

Custer	gene	avg_log2FC	p_val_adj
Enteroendocrine cells	Cck	6.6484	0
	Cpe	3.387268	0
	Scg2	3.34359	0
	Neurod1	2.906056	0
	Scgn	2.718482	0
	Isl1	2.593089	0
	Etv1	2.569116	0
	Aplp1	2.454927	0
	Hmgn3	2.36314	0
	Insm1	2.315625	0
	Pax6	2.249145	0
	Scg3	2.151851	0
	Cacna1a	2.02748	0
	Fev	2.007443	0
	Vwa5b2	2.001867	0
	Cxxc4	1.99328	0
	Gfra3	1.867859	0
	Prnp	1.798836	0
	Pclo	1.705309	0
	Nefm	1.688442	0
Enterochromaffin cells (EEC)	Tac1	5.204728	0
	Tph1	4.152842	0
	Rab3c	3.643486	0
	Lmx1a	2.20006	0
	Slc38a11	1.788665	0
	Trpm2	1.340097	0
	Cwh43	0.89916	0
	Scn3a	3.083233	2.88E-288
	Kcnc1	1.314007	4.80E-249
	Snap25	2.247043	1.65E-247
	Ryr3	0.804422	6.21E-241
	Glis3	0.949516	1.99E-240
	Il18r1	1.207466	1.21E-238
	Gabra2	0.583984	2.00E-229
	Agr3	1.26253	6.98E-229
	Tmigd3	0.938748	2.99E-228
	Syn2	1.127666	1.15E-220
	Trpc7	0.581379	2.55E-219
	Npy1r	0.78834	7.55E-206
	Trpa1	2.205859	2.97E-186

Table 2.5 Top 100 and Bottom 100 loadings of PC1 component among the epithelium populations PC1 represented the developmental trajectories of epithelial populations. Loadings on PC1 are summarized in the table.

Epithelium Top 100 PC1 loadings			
gene	loading	gene	loading
Mt1	0.1022	Akr1c19	0.0274
H19	0.0819	Ace2	0.0269
Fabp1	0.0715	Atp5j2	0.0269
Prap1	0.0675	Maob	0.0266
Apoa1	0.0666	Hmgcs2	0.0264
Mt2	0.0660	Cox5a	0.0263
Fabp2	0.0576	S100a10	0.0257
Dbi	0.0575	Scd2	0.0254
Apoc3	0.0492	Fcgrt	0.0254
2200002D01Rik	0.0478	Mif	0.0253
Apoa4	0.0449	Gpx1	0.0253
Rps8	0.0438	Lct	0.0252
Lypd8	0.0437	Rpl37	0.0251
Hspe1	0.0421	Rpl13	0.0250
S100g	0.0418	Hmgb2	0.0249
Spink1	0.0416	Rpl32	0.0247
Oat	0.0413	Gpx4	0.0245
Rplp1	0.0406	Rpl27a	0.0241
Rbp2	0.0393	Sult1b1	0.0240
Cps1	0.0374	Gstm3	0.0240
Rpl41	0.0365	Txn1	0.0238
Hspd1	0.0362	Acaa2	0.0237
Pycard	0.0361	Pdzk1ip1	0.0237
Mttp	0.0360	Gna11	0.0236
mt-Cytb	0.0351	Chpt1	0.0231
Dmbt1	0.0343	Ckmt1	0.0231
Maf	0.0326	Aadac	0.0230
Jaml	0.0325	Bex4	0.0230
Rps2	0.0321	Alpi	0.0230
Aldob	0.0321	Plin2	0.0230
Ptma	0.0319	Top2a	0.0229
Mamdc4	0.0318	C1qbp	0.0229
Aprt	0.0317	Apob	0.0229
Uqcrq	0.0316	Rps29	0.0227
Chchd10	0.0312	Tmem37	0.0226
mt-Nd1	0.0306	Rpl39	0.0225
Rps12	0.0304	Cyc1	0.0224
Creb3l3	0.0303	Rps19	0.0223
Atp5k	0.0302	Npm1	0.0223
Uqcr11	0.0301	Slc51a	0.0221
Ncl	0.0299	St3gal4	0.0220
Atp5g1	0.0297	Mgst1	0.0218
Cdkn1c	0.0293	Eps8l3	0.0217
Rpl36	0.0289	Ndufa4	0.0215
Cox5b	0.0287	Slc7a9	0.0214
Rpl6	0.0286	Cycs	0.0214
mt-Co3	0.0281	Rpsa	0.0210
Adh1	0.0281	Mogat2	0.0210
Dgat2	0.0279	Gsta2	0.0209
Cox7b	0.0277	Aldh1b1	0.0206

Epithelium Bottom 100 PC1 loadings			
gene	loading	gene	loading
Sct	-0.1886	Rimbp2	-0.0517
Tff3	-0.1766	Tspan1	-0.0514
Fxyd3	-0.1605	Scin	-0.0510
Clps	-0.1478	Tpsg1	-0.0510
Selenom	-0.1383	Cst3	-0.0506
Hepacam2	-0.1088	Defa17	-0.0504
Malat1	-0.1075	Creb3l1	-0.0499
Bex2	-0.0990	Gnao1	-0.0496
Neurod1	-0.0980	Gcnt3	-0.0494
Chgb	-0.0958	Scg2	-0.0494
Serpina1c	-0.0940	Cplx2	-0.0493
Spink4	-0.0933	Ddc	-0.0493
Cpe	-0.0915	Cadps	-0.0487
Cck	-0.0858	Serpinf2	-0.0480
Agr2	-0.0855	Ids	-0.0477
Insm1	-0.0831	Sez6l2	-0.0473
Fcgbp	-0.0826	Cacna2d1	-0.0471
Serpina1b	-0.0806	Cbfa2t3	-0.0466
Meg3	-0.0759	Reg4	-0.0461
Aplp1	-0.0757	Myl7	-0.0460
Guca2a	-0.0756	Pyy	-0.0456
Vwa5b2	-0.0753	Muc2	-0.0452
Tm4sf4	-0.0743	Cdkn1a	-0.0451
Scgn	-0.0709	Igfbpl1	-0.0450
Fev	-0.0700	Gch1	-0.0446
Ffar2	-0.0690	Gm35409	-0.0442
Hmgn3	-0.0684	Itm2c	-0.0441
Map1b	-0.0679	Tpd52	-0.0439
Fam183b	-0.0669	Gm1123	-0.0438
Defa24	-0.0664	Map2	-0.0437
Cxxc4	-0.0661	Hk2	-0.0435
Cacna1a	-0.0658	Syt7	-0.0434
Chga	-0.0646	Txndc5	-0.0434
Ttr	-0.0644	Smpd3	-0.0433
Isl1	-0.0643	Clca1	-0.0432
Etv1	-0.0640	Dst	-0.0430
Gfra3	-0.0640	Syt13	-0.0428
Tox3	-0.0620	Abcc8	-0.0426
Peg3	-0.0611	Krt18	-0.0423
Nkx2-2	-0.0602	Krt8	-0.0420
Scg3	-0.0597	Atp2a3	-0.0420
Pax6	-0.0585	5330417C22Rik	-0.0419
Camk2n1	-0.0573	Tspan13	-0.0418
Pcsk1	-0.0563	Anxa6	-0.0417
Prnp	-0.0558	Ptprn2	-0.0416
Pam	-0.0551	Pclo	-0.0412
Runx1t1	-0.0540	Rgs17	-0.0412
Smim6	-0.0527	Cryba2	-0.0410
Ghrl	-0.0518	Kctd12	-0.0407
Ccl9	-0.0518	Celf3	-0.0405

Table 2.6 Top 100 and Bottom 100 loadings of PC6 component among the subepithelial mesenchymal cell populations PC6 represented the tissue identity along the length of the intestine among PDGFRα^{High} cell populations. Loadings on PC6 are summarized in the table.

Top 100 PC6 loadings			
gene	loading	gene	loading
Lsp1	0.1281	Grb10	0.0338
H19	0.1031	Nr2f2	0.0335
Ptn	0.1029	Ddx21	0.0332
Dlk1	0.0802	Myl6	0.0330
Acta2	0.0773	Tle4	0.0329
mt-Co3	0.074	Sparcl1	0.0328
Meis2	0.0737	Tmem158	0.0324
Nrp2	0.0732	Igf2	0.0323
Rgs5	0.0729	Hist1h2bc	0.0317
Hand2	0.067	Ptma	0.0317
Hmgb1	0.0644	Nasp	0.0312
Plagl1	0.064	mt-Nd3	0.0310
Gas1	0.062	Abcc9	0.0309
mt-Cytb	0.0614	Lmnb1	0.0308
Igfbp5	0.0605	Bcl11a	0.0305
Cdkn1c	0.0601	Runx1t1	0.0305
Cd81	0.0596	Slc12a2	0.0304
mt-Atp6	0.0594	Hmga2	0.0303
Aldh1a2	0.0582	Ptms	0.0301
Wnt5a	0.0576	Tagln	0.0300
Smoc2	0.0563	Gdf10	0.0296
Tmsb4x	0.0555	Dynll1	0.0296
mt-Nd4	0.0518	Hnrnpa3	0.0290
Psd	0.0504	Gm42418	0.0290
mt-Nd1	0.0473	Myh11	0.0288
Actb	0.0453	Pbx1	0.0283
Thbs4	0.0432	Ldhb	0.0283
Myl9	0.0423	Epha4	0.0283
Nucks1	0.0411	Nrk	0.0281
Tmsb10	0.0399	Lgals1	0.0280
Sfrp1	0.0397	Myh10	0.0278
Tshz2	0.0394	Samd5	0.0277
Alcam	0.0388	Btg1	0.0277
Tsc22d1	0.0385	Nme1	0.0275
Sox4	0.0382	Ranbp1	0.0275
Khdrbs3	0.0382	Fdps	0.0275
Meis1	0.0381	Iqgap2	0.0272
Sub1	0.038	Gucy1b1	0.0269
Npnt	0.0378	Gm26917	0.0264
Ppp1r14b	0.0377	Adamts18	0.0264
mt-Co2	0.0371	Meg3	0.0262
Foxp1	0.0371	Nrep	0.0260
Ncl	0.0371	Hmgcs1	0.0258
Kcnj8	0.0369	H3f3b	0.0254
Svil	0.0365	Ddx3y	0.0253
Mest	0.0363	H2afz	0.0252
Vcan	0.0363	Hmgb3	0.0252
Pdgfra	0.036	Pid1	0.0247
Set	0.0354	Gm34030	0.0242
Hoxa4	0.0339	Zfhx4	0.0242

Bottom 100 PC6 loadings			
gene	loading	gene	loading
Adamdec1	-0.2737	Icam1	-0.0502
Fos	-0.1918	Tmem100	-0.0497
Junb	-0.1914	Klf2	-0.0497
Jun	-0.1647	Gem	-0.0495
Cebpd	-0.144	Phlda1	-0.0492
Nfkbia	-0.1301	Dusp1	-0.0489
Sparc	-0.1262	Rps20	-0.0489
Ccl11	-0.1225	Pcolce	-0.0488
Btg2	-0.1185	Rps24	-0.0487
Cxcl10	-0.1177	Apela	-0.0485
Dcn	-0.1119	Rps3a1	-0.0479
Zfp36	-0.109	Ifitm3	-0.0476
Egr1	-0.1068	Rps12	-0.0468
Socs3	-0.1019	Col6a4	-0.0458
Irf1	-0.0989	Stc2	-0.0455
Cxcl13	-0.0985	Gpc3	-0.0447
Ier2	-0.094	Rps28	-0.0443
Ier3	-0.0933	Col6a2	-0.0443
Fosb	-0.0899	Adamts1	-0.0433
Hist1h2ae	-0.084	Rpl27a	-0.0425
Xist	-0.0822	Rpl37a	-0.0422
Plac8	-0.0783	Ccl2	-0.0416
Id3	-0.0778	Aebp1	-0.0406
Atf3	-0.0754	Bmp4	-0.0405
Col1a1	-0.0752	Nkx2-3	-0.0404
Gadd45g	-0.0751	Mfap4	-0.0403
Pim1	-0.0735	Rpl24	-0.0402
Hist1h1b	-0.0709	Rps27a	-0.0401
Igfbp7	-0.0695	Cited2	-0.04
Cxcl1	-0.0686	Rps27	-0.0399
Rarres2	-0.0681	Anxa2	-0.0398
Rps8	-0.0666	Prc1	-0.0396
Rpl39	-0.0666	Zeb2	-0.0394
Gadd45b	-0.0643	Gpx3	-0.0388
Top2a	-0.0624	S100a10	-0.0384
Col6a5	-0.0602	44443	-0.0384
Hspa1a	-0.0601	Rap2a	-0.0383
Gm26532	-0.06	Rpl37	-0.0383
Rpl23	-0.0594	Procr	-0.038
Tpt1	-0.0583	Apoe	-0.038
Jund	-0.0579	Ppp1r15a	-0.038
Cebpb	-0.0559	Eef1a1	-0.0377
Tagln2	-0.0558	Rps5	-0.0376
Rpl28	-0.0549	Gm13889	-0.037
Col1a2	-0.0542	Thbs1	-0.037
Igf1	-0.0533	Rpl32	-0.0368
Abi3bp	-0.052	Tmem176b	-0.0367
Rps4x	-0.0519	Aldh2	-0.0366
Rpl6	-0.0515	Tmem176a	-0.0364
Cxcl2	-0.0503	Mmp23	-0.0364

2.3 Adhesion and actomyosin activity are required for mesenchymal cluster formation

Cell adhesion including both cell-cell adhesion molecules, cadherins, and cell-ECM adhesion molecules, integrins, was one of the signatures that distinguishes newly differentiated clustering PDGFRα^{High} cells from the rest of the *Bmp4* expressing subepithelial mesenchymal cell population in our single-cell sequencing data. A few types of cadherins, *Cdh4* and *Cdh11* in particular, are upregulated in the clustering cells (**Fig. 2.11**A,B). As various ECM and integrins were also upregulated in the PDGFRα^{High} cell populations, we investigated the role of the integrins in mesenchymal cluster formation.

Integrins are heterodimeric transmembrane receptors comprising alpha and beta subunits that facilitate cell-matrix-cell and cell-ECM adhesion. Integrin β1 is the most abundant β-subunit and makes heterodimers with a number of alpha subunits, with the specificity to particular ECM substrates largely determined by the combination of alpha and beta subunits. Our data show that Integrin β1 is expressed throughout the subepithelial mesenchymal cells and that Integrin β8 expression is upregulated in the PDGFRα^{High} cells. As for alpha subunits, Integrin α1, 2, 8 and 11 were specifically upregulated in the clustering PDGFRα^{High} population, while integrin α5 and αV expression were widespread across the subepithelium mesenchymal cell population (**Fig. 2.11**C). The expected binding partners, ECM components such as collagens, fibronectins, and laminin proteins, were also present throughout the mesenchyme (**Fig. 2.11**D). Relevant integrin alpha and beta subunit heterodimer pairs and their target ECM components are summarized in **Table 2.7**. To test the roles of integrins, explant

tissues were subjected to treatment with TC-I 15, a specific molecule inhibitor of Integrin $\alpha 2\beta 1$, and an Integrin $\alpha 5\beta 1$ inhibitor. Integrin $\alpha 2\beta 1$ mainly interacts with collagens and laminins, which are highly enriched at the basement membrane during cell clustering. Blocking $\alpha 2\beta 1$ function impaired the formation of tight clusters and led to a failure of basement membrane deformation along the basal surface. On the other hand, blocking $\alpha 5\beta 1$, which mainly binds to fibronectin that is present throughout the mesenchyme, completely prevented cluster formation. The fact that these tissues failed to form tight mesenchymal cell clusters and epithelial deformation when integrin function is blocked, suggests that specific integrin mediated cell-ECM adhesion is essential for cluster formation and villus initiation (**Fig. 2.12**A).

Both integrins and cadherins are linked to the actin cytoskeleton intracellularly, and non-muscle myosin mediated actomyosin activities have been implicated in adhesion formation and maturation (Vicente-Manzanares et al., 2009). Integrin-ECM adhesions have also been suggested to enhance cadherin-mediated cell-cell adhesion strength through actomyosin activities (Martinez-Rico et al., 2010). We therefore hypothesized that actomyosin activity may also be essential in driving cluster formation by assisting cell-cell adhesion of PDGFRα^{High} cells (**Fig. 2.12**B).

Indeed, our single cell analysis along with immunostaining reveals that two out of three major isoforms of non-muscle myosin, non-muscle myosin IIA (*Myh9*) and IIB (*Myh10*) are highly expressed in PDGFRα^{High} clusters (**Fig. 2.12**C). Activities of the actomyosin were further suggested by increased expression of myosin light chain kinase (Mylk) and phospho-myosin light chain (pMLC) within clustering PDGFRα^{High} subepithelial cells (**Fig. 2.12**C). When actomyosin activity was inhibited in explant tissue

culture by treatment with the myosin II inhibitor, blebbistatin, or Rock inhibitor, Y-27632, both the treated tissues failed to form mesenchymal clusters and subsequent villus morphogenesis (**Fig. 2.12**D). These treatments however did not prevent the differentiations of PDGFRα^{High} cell populations in the subepithelial layer. In addition, Blebbistatin treatment was reversible; when the drug was removed from the culture, the tissue started forming mesenchymal cell clusters and corresponding villi (**Fig. 2.12**D). This suggests that differentiated PDGFRα^{High} cells are primed to cluster, but blebbistatin treatment blocks it. Importantly, we did not observe pMLC in the overlying epithelium, consistent with our other findings suggesting the initial buckling event in the epithelium is driven by the actomyosin activities of the mesenchyme.

Pharmacological treatment, however, is systemic and not specific to different tissue components. In order to assess the importance of myosin activity specifically in mesenchymal cells, we generated *Myh9* and *Myh10* double conditional KO mice. When the *Myh9* and *Myh10* were knocked out in epithelium by using a constitutively active *Shh-Cre* driver, Shh^{Cre} ,$Myh9^{flox/flox}$,$Myh10^{flox/flox}$, intestinal morphology was substantially altered. The proximal portion of the intestine was inflated, while the diameter of the tube got narrower and the epithelial layer was disrupted in the distal region. Indeed, cross-sectional examination of the distal tissue revealed greatly deformed morphology of the epithelial layer, where fewer bloated epithelial cells were covering the luminal surface. However, the mesenchymal cell clusters and corresponding basal deformation were still observed (**Fig. 2.13**).

Similarly, *Myh9* and *Myh10* were knocked out in mesenchyme with a constitutive mesenchymal driver *Twist2-Cre* or with an inducible driver, *Pdgfra-CreER*. Embryos

with *Twist2*^{Cre} ,*Myh9*$^{flox/flox}$,*Myh10*$^{flox/flox}$ genotypes were not viable (data not shown). Therefore, we used *Pdgfra-CreER*, an inducible driver specific to mesenchyme. Tamoxifen was administered to pregnant dams by oral gavage three consecutive days between E11.5 and E13.5 before embryos were collected (**Fig. 2.14**A). The *Pdgfra*^{CreER} ,*Myh9*$^{flox/flox}$,*Myh10*$^{flox/flox}$ double-knockout mice however did not show a visible embryonic phenotype or a villus structural phenotype, despite recombination of the fluorescent reporter mT/mG, suggesting that Cre was active in these cells (**Fig. 2.14**B). We next performed both qPCR and immunostaining to examine the level of mRNA and protein. qPCR revealed that mRNA expression in mesenchymal cells was reduced to 30%, but still detectable in the knockout tissues (**Fig. 2.14**C). Expression of *Myh11*, a muscle subtype of myosin heavy chain, was increased in the knockout tissue, suggesting possible compensation (**Fig. 2.14**D). In addition, protein staining revealed that both non-muscle myosin IIA and IIB expression was reduced but still present in the mesenchymal clusters (**Fig. 2.14**B). These data suggest that incomplete gene knockout, compensation by other genes, or protein perdurance, or a combination of all three, could underlie the lack of a phenotype in these mutants. We also attempted to increase the efficiency of deletion by using null/flox lines, which would only require recombination of one allele at each locus, but double null/flox knockout mice also did not reveal obvious defects to villus structure at E15.5 (**Fig. 2.14**E).

Despite the lack of a visible phenotype with these knockout tissues, the Myh9 and Myh10 deleted intestines with reduced mesenchymal expression of non-muscle myosins were more sensitive to the treatment with the actomyosin inhibitor, blebbistatin. When the E13.5 explant tissues of *Pdgfra*^{CreER} ,*Myh9*$^{flox/flox}$,*Myh10*$^{flox/flox}$ mice were

cultured in reduced concentration of Blebbistatin, we observed that knockout tissues were significantly more likely to fail to form mesenchymal clusters in comparison to its wild-type littermates (**Fig. 2.15**).

Together, these results suggest that mesenchymal actomyosin activity and integrin-mediated adhesions are critical in driving cluster formation and induce subsequent villus evagination.

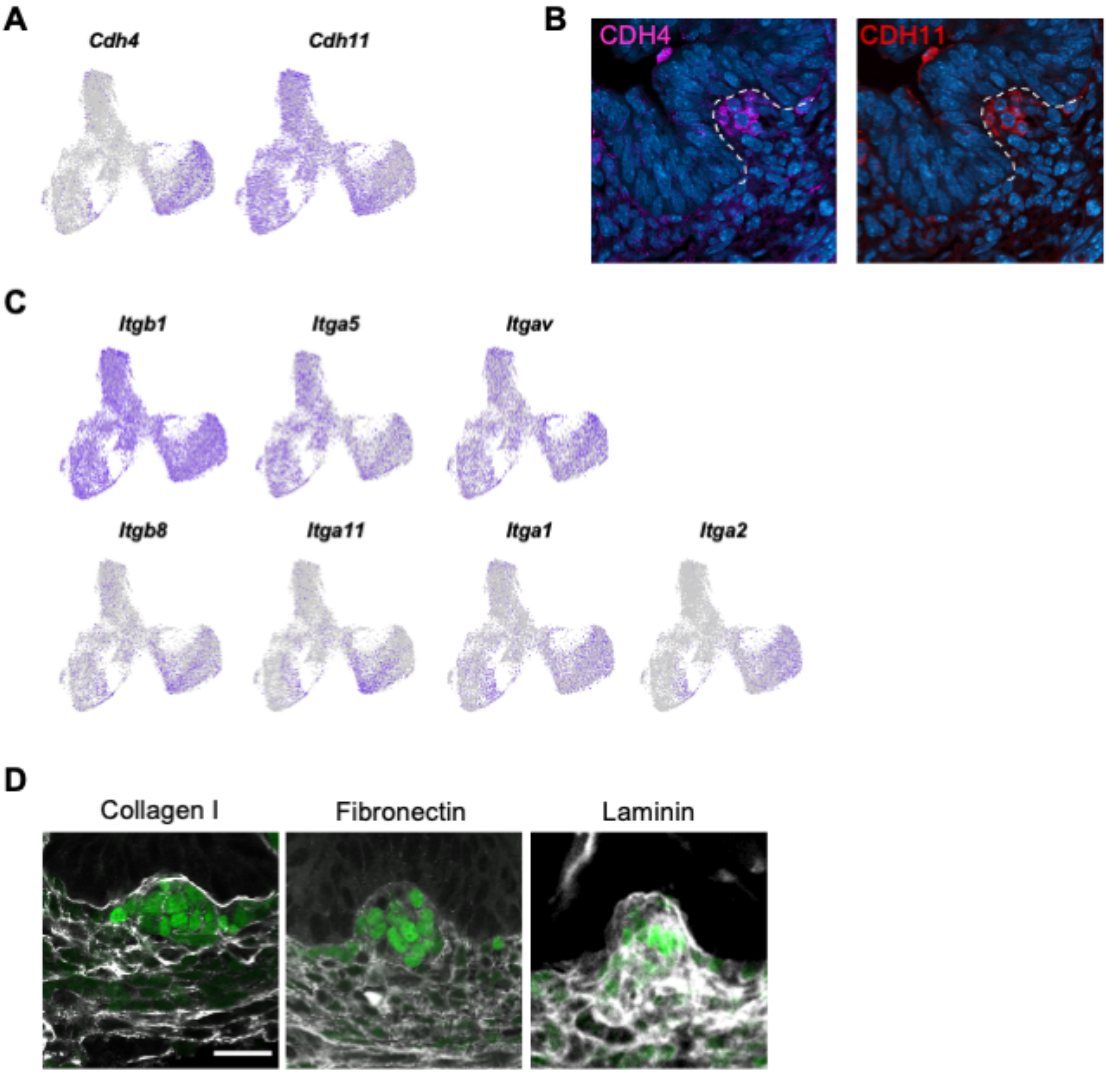

Figure 2.11 Expression of adhesion-related genes and proteins in mesenchyme A. Expression of cadherin genes in subepithelial mesenchyme. **B.** Cadherin 4 and 11 protein expressions are upregulated in the mesenchymal cluster. **C.** Integrin α and β subunit gene expression in subepithelial mesenchyme. **D.** ECM protein expression in mesenchyme. Scale bar = 25 μm.

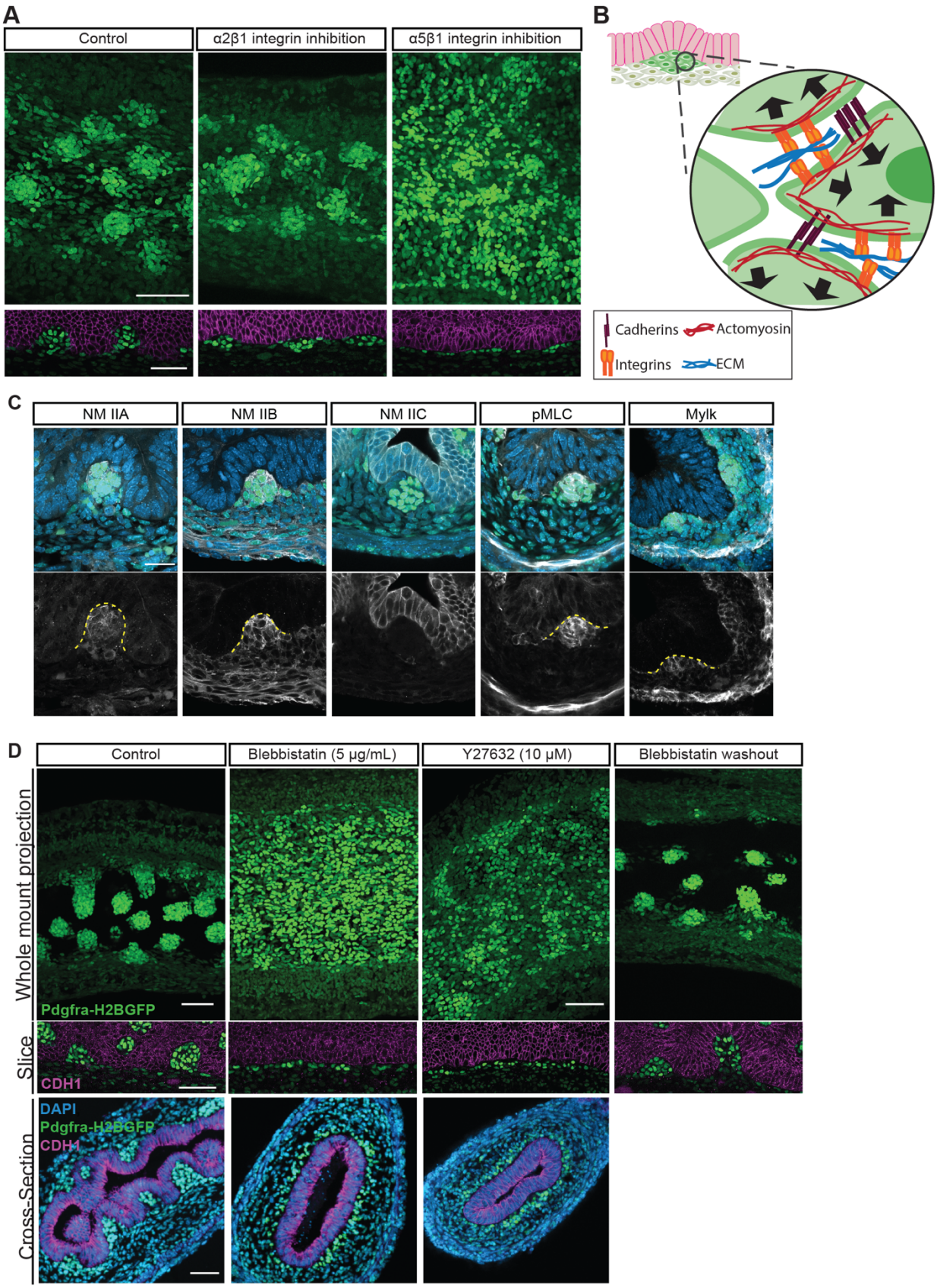
A
Control
α2β1 integrin inhibition
α5β1 integrin inhibition
B
Cadherins
Actomyosin
Integrins
ECM
C
NM IIA
NM IIB
NM IIC
pMLC
Mylk
D
Control
Blebbistatin (5 μg/mL)
Y27632 (10 μM)
Blebbistatin washout
Whole mount projection
Pdgfra-H2BGFP
Slice
CDH1
Cross-Section
DAPI
Pdgfra-H2BGFP
CDH1

Figure 2.12 Adhesion and contractility programs are indispensable for PDGFRα^{High} mesenchymal cluster formation A. E13.5 PDGFRα^{High} tissue cultured with integrin inhibitors for 2 days. Integrin α2β1 inhibition results in wider clusters without epithelial morphogenesis and integrin α5β1 inhibition results in failure to form clusters. **B.** Schematic diagrams displaying integrins and cadherin connected to the actomyosin network intracellularly. **C.** Expression of proteins suggestive of active actomyosin activities in the clustering mesenchymal cells. **D.** E13.5 PDGFRα^{High} tissue cultures with actomyosin inhibitors. Blebbistatin treated tissue once the drug is replaced with control media after 2 days of culture formed mesenchymal clusters and deformed basal epithelium just as control tissue.

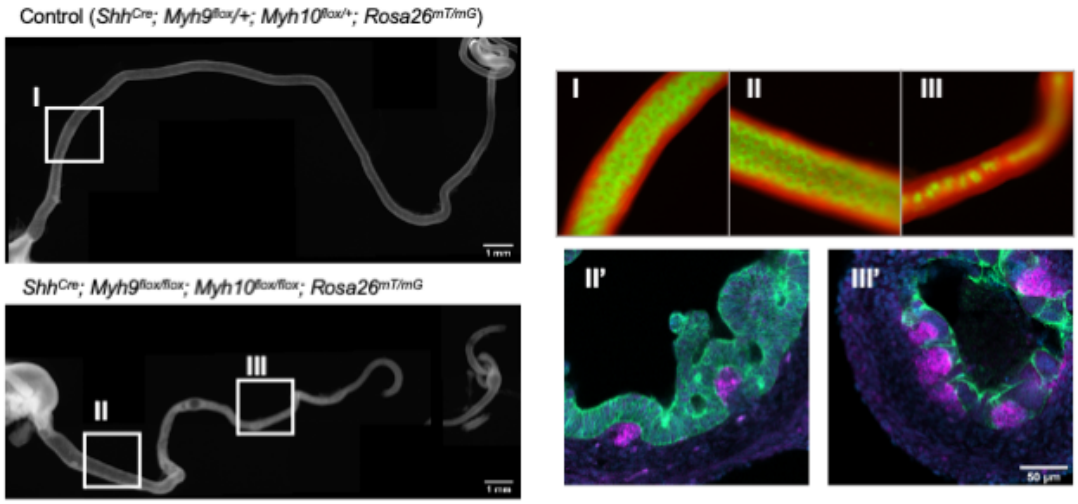

Figure 2.13 E15.5 Intestinal tissues of *Myh9* and *Myh10* double knockout in epithelium Images of E15.5 intestines of control and epithelial *Myh9* and *Myh10* knockout tissue. (I-III) mT/mG expression of the whole mount tissue shows the epithelium (green) and mesenchyme (red) of the tissue at locations indicated in the left panels. The distal region of the mutant tissue (III) reveals narrower tubes and discontinuous luminal epithelium. (II', III') Cross sections of the proximal (II') and distal (III') region of mutant tissue with PDGFRα immunofluorescent staining (magenta).

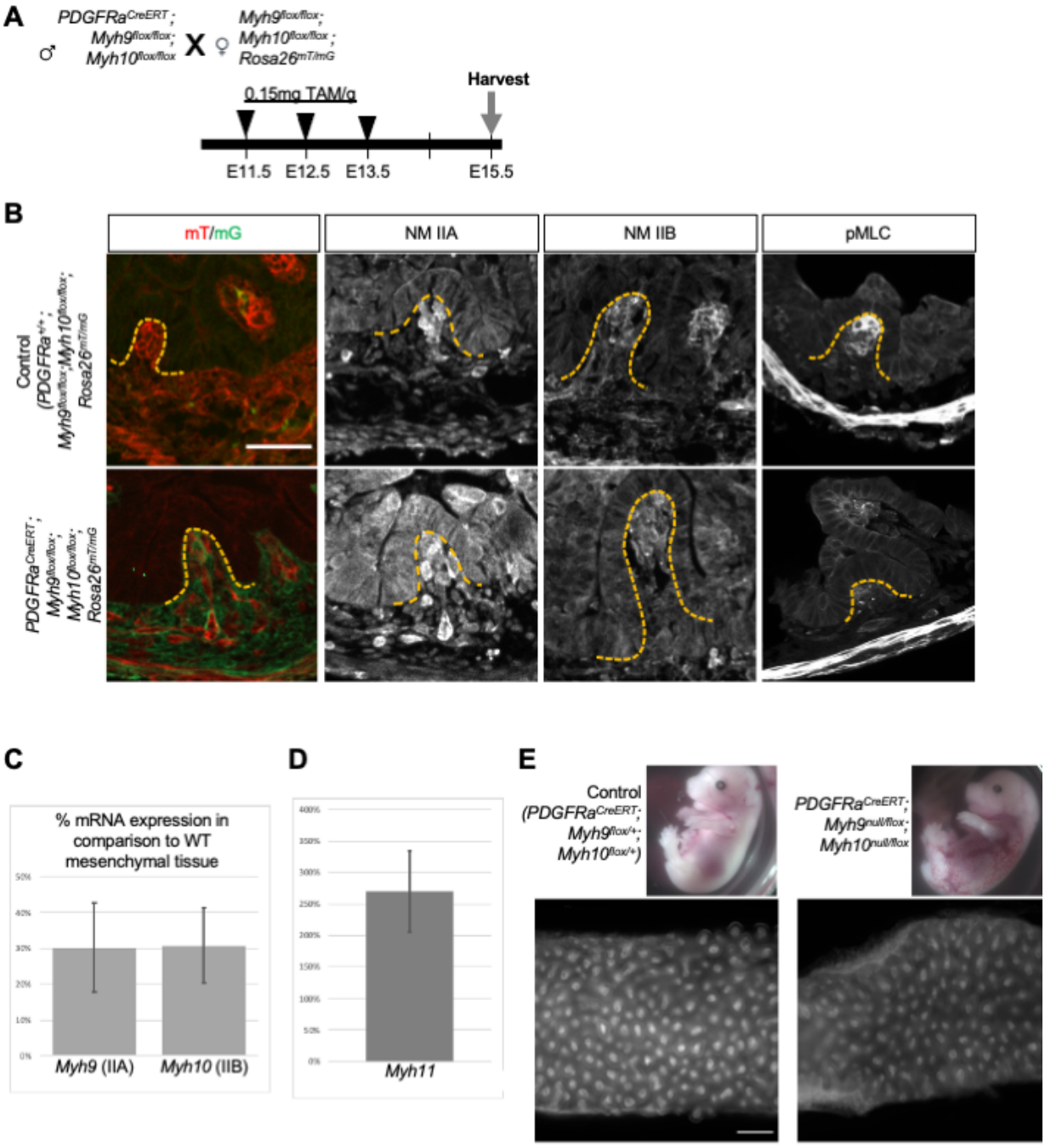
A
PDGFRa CreERT ; Myh9 flox/flox ; Myh10 flox/flox
X
Myh9 flox/flox ; Myh10 flox/flox ; Rosa26 mT/mG
0.15mg TAM/g
Harvest
E11.5 E12.5 E13.5 E15.5
B
mT/mG
NM IIA
NM IIB
pMLC
Control (PDGFRa +/+ ; Myh9 flox/flox ; Myh10 flox/flox ; Rosa26 mT/mG
PDGFRa CreERT ; Myh9 flox/flox ; Myh10 flox/flox ; Rosa26 mT/mG
C
% mRNA expression in comparison to WT mesenchymal tissue
50%
40%
30%
20%
10%
0%
Myh9 (IIA)
Myh10 (IIB)
D
400%
350%
300%
250%
200%
150%
100%
50%
0%
Myh11
E
Control (PDGFRa CreERT ; Myh9 flox/+ ; Myh10 flox/+)
PDGFRa CreERT ; Myh9 null/flox ; Myh10 null/flox

Figure 2.14 E15.5 Intestinal tissues of *Myh9* and *Myh10* double knockout in mesenchyme **A.** Illustration of experimental protocol outlining induction of knockout in PDGFRα inducible driver. **B.** Fluorescent images of tissue sections. mT/mG fluorescent reporter and immunofluorescent staining of non-muscle myosin IIA and IIB proteins reveal the perdurance of non-muscle myosin proteins in spite of the successful recombination reported by mT/mG. Scale bar = 50 μm. **C,D.** % mRNA expression of *Myh9, Myh10* (C) and *Myh11* (D) normalized to the heterozygous knockout (control) tissue measured by qPCR. **E.** Images of the embryo and intestine's luminal images of E15.5 Myh9 and Myh10 null/flox double knockout mice. The knockout embryos did not display recognizable phenotype aside from increased blood vessels sighted. Both of the intestinal lumens were covered by villi structures. Scale bar = 200 μm.

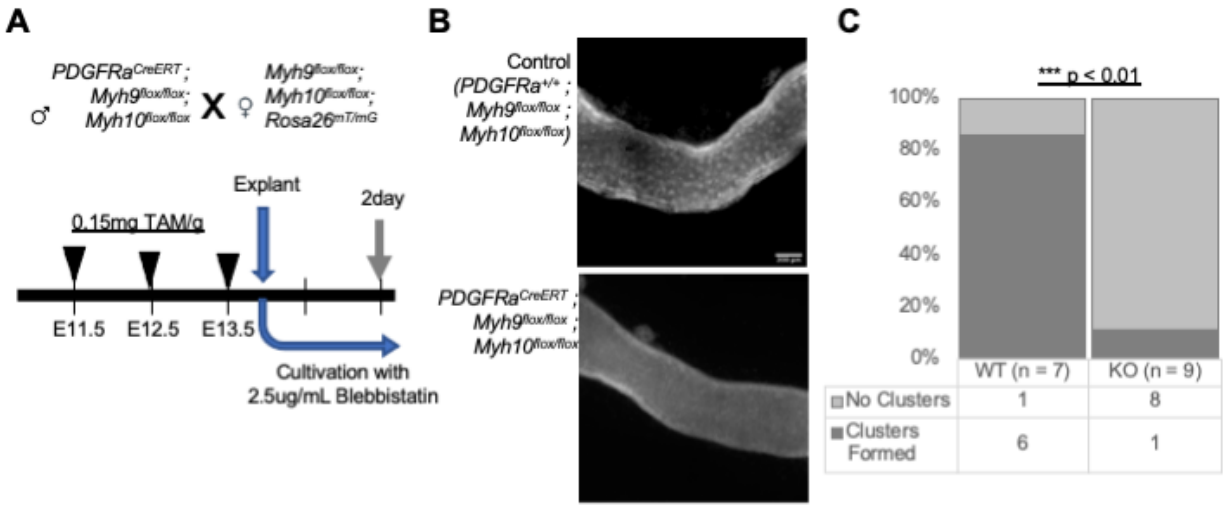

Figure 2.15 Mesenchymal *Myh9, Myh10* double knockout intestines were more sensitive to lower doses of blebbistatin treatments A. Illustration of experimental protocol outlining induction of knockout in *Pdgfra* inducible driver and explant culture. Tissues were cultivated in the presence of half the concentration of typical blebbistatin concentration. **B.** Representative images of control and double knockout intestine after 2 days of culture in the presence of Blebbistatin. Control tissue reveals formations of clusters, while they are not sighted in the knockout tissue. **C.** Summary of total number of tissues experimented across three different experimental littermates.

Table 2.7 Summary of Integrin alpha and beta subunit pairs and their predicted ECM binding partners

INTEGRIN ALPHA SUBUNIT	INTEGRIN BETA SUBUNIT	LIGAND ECM
Itga1	Itgb1	Laminin, Collagen
Itga2	Itgb1	Laminin, Collagen, Fibronectin
Itga11	Itgb1	Collagen
Itga5	Itgb1	Fibronectin, Fibrinogen
Itgav	Itgb1, 3, 5, 6 or 8	Vitronectin, Fibronectin, Fibrinogen, Laminin (RGD)

2.4 Exploring physical models that explain the mechanism of villus morphogenesis

To further quantify the relationship between mesenchymal cluster formation and villus morphogenesis, we constructed computational models of the clustering process. The models are helpful to understand the phenomenon more quantitatively and to build hypotheses for experimental testing.

2.4.1 Spring Model

Developing intestinal tissue has been modeled as an elastic solid in the past, and mesenchymal cluster-driven morphogenesis of engineered tissue has been described using a linear elastic-solid spring model (Hughes et al., 2018; Shyer et al., 2013). Therefore, we investigated whether the same elastic-solid framework could be applied to describe the mesenchymal clustering behavior that drives the initiation of villus morphogenesis. In our spring model implementation, tissue is modeled as an interconnected mesh of springs with given resting lengths and spring constants (**Fig. 2.16**A). Differential tissue properties can be applied by assigning relative spring constants to springs of each tissue layer separately. Clustering of the subepithelial mesenchymal layer (PDGFRα^{High} cells) was simulated by shortening the horizontal resting length of springs at a pre-assigned clustering site. The initial model predicted that the degree of bending is dependent on differential stiffness of the layers above (epithelium) and below (mesenchyme) the clustering site, and significant stiffness differences between the two layers was required to achieve the targeted level of

bending (**Fig. 2.16**B). We used atomic force microscopy (AFM) to measure the elastic stiffness of each tissue component of E14.5 tissue, which is the stage right before the formation of clusters and initiation of vilification (**Fig. 2.16**C). These studies revealed that the epithelial layer is ~2 times stiffer than the mesenchymal layer, in agreement with what has been previously reported (Shyer et al., 2013). According to our initial model, however, this level of stiffness difference is not sufficient to predict any significant curvature formation. To investigate the system dynamics further, we modified the model by assuming that, in addition to horizontal contractions within the clustering site, the clustering site as a whole further contracts towards the epithelium. With the assumption of vertical contractions, the requirement for differential stiffness between layers was relaxed, and a significant degree of buckling was predicted by the model even when all the layers had equal stiffness values (**Fig. 2.16**D,E).

In the spring model, when spring resting lengths of the clustering sites are shortened, their surrounding spring edges are expected to bear elevated tensile stress. Therefore, when the strain is relaxed by making a cut on the tension-bearing region of the tissue, the material is expected to recoil (Hughes et al., 2018; Panousopoulou and Green, 2016) (**Fig. 2.16**F). To study this, we made cuts in regions adjacent to the nascent cluster sites using laser ablation. When the tissue region next to the cluster was ablated, however, the tissue did not show measurable recoil behavior. Instead, over several minutes following the generation of the cuts, the opened sites slowly closed, suggesting lack of residual tensions in these regions of tissue (**Fig. 2.16**G). We also investigated whether the mesenchymal clustering cells may pull on and bend the epithelial layer by generating tensile stresses across the base of clusters, a mechanism

similar to intercalation and bridging by suprabasal layer during placode morphogenesis (Panousopoulou and Green, 2016) (**Fig. 2.16**H). Making incisions at mesenchymal clusters also did not result in recoiling behavior, suggesting that this alternative mechanism also is unlikely to be responsible (**Fig. 2.16**I).

The spring model assumes that the tissue is a connected mesh of springs, and that there is no exchange of neighbors and connections. However, in our live imaging experiments, we observed some nuclei moving long distances independently from their surrounding materials before joining the cluster, as clustering mesenchymal population and non-clustering mesenchymal population revealed vastly different motion within the tissue (**Fig. 2.1**E). In addition, some cells were crossing their path and moving towards opposite directions (**Fig. 2.17**A, B). Given that the final cell membrane borders of clusters are aligned tangentially to the cluster boundaries (**Fig. 2.17**C), rather than radially elongated from their original locations, it seems likely that the cellular neighbor exchanges occur in the cluster formation.

2.4.2 Phase-Separation Model

These data demonstrate that (i) the tissues do not bear tensile stress at or around nascently formed clusters, and (ii) cells engage in long distance motion with neighbor exchange behavior. Therefore, we reasoned that our data were more consistent with a model of tissue mechanics in which fluid-like (viscous) characteristics dominate over elastic-like characteristics. Previous reports support the notion that even though soft tissues may behave as elastic solids at short time scales (seconds to

minutes), they undergo cellular reorganization and the state can be described as viscoelastic or more fluid-like at longer time scales (minutes to hours) that are more relevant to the time scales in which the morphogenesis occurs (Gonzalez-Rodriguez et al., 2012). The fluid-like behavior of tissues during development has been described previously, including recently by Mongera et al (Mongera et al., 2018). To further consider what mechanisms could explain the reorganization of fluid-like tissues as seen in the villus cluster formation, it was observed that, qualitatively, the cluster formation bears striking similarity to many dewetting processes in nature, where cohesive liquid on a substrate breaks up and aggregates into rounded structures driven by differential adhesions between materials. Motivated by these observations, we formulated a continuum model of clustering based on the classical Cahn-Hilliard phase separation dynamics, where different tissue types are represented by abstract material phases, and the material reorganization is driven by unique surface energies of each phase arising from the cohesive and adhesive forces in the system (Cahn & Hilliard, 1958). The basis of this model is consistent with the hypothesis that sorting rearrangement of cells can be explained by surface tensions as cells move towards the configuration that minimizes total surface energy (Steinberg, 1963). One crucial difference between the model and real tissues worth noting is that the model does not distinguish between adhesion proper and contractility, that is, whereas the tissue clustering requires both the favorable connection (adhesion) and the action on the connection (contraction) separately, the model combines both these factors together by essentially assuming that whenever there is a favorable connection, there is contraction. In real tissues, however, these two factors are separable, as demonstrated by the Blebbistatin

experiments which block the cell contractility and hence clustering, while leaving adhesion markers intact. In the present study it was assumed that the separation of adhesion and contractility in the model is not central for formulating a model of the fundamental dynamics driving the clustering, although future studies would be needed to confirm the validity of this assumption.

In our model we identified three material phases as cell fractions, C_1, C_2, C_3, representing PDGFRα^{low}, PDGFRα^{High} and epithelial cells, respectively. Surface energies between phases *i* and *j* are indicated by σ_{ij} (**Fig. 2.18**A). Based on given surface energies, a triple-well potential energy is defined, and the system evolves to minimize the total tissue free energy over the whole tissue. With suitable values of surface energies, break-up and condensation of the phase representing the subepithelial mesenchyme was observed, followed by the clusters pushing against the epithelial phase, qualitatively matching the same phenomena in the real tissue (**Fig. 2.18**B**,**C). Based on the comparison of simulated material velocity and maximum cell velocity in tissue as a function of total distance traveled, the temporal progression of cluster geometry qualitatively matched that of real clusters (**Fig. 2.18**D). One key prediction of the model is that the cluster contact angles are determined by the hierarchy of tissue surface energies (**Fig. 2.18**C). Here, the surface energy values for the simulations were determined based on the similarity of contact angles between the simulated and real tissue clusters, rather than measurement of tissue surface energies. While several techniques exist to determine the surface energies of clusters of cells, such data was not available for this study, and hence the prediction of the connection between the contact angles and surface energies was left untested.

This model, in comparison to the spring model, predicts not only the deformation of the epithelium corresponding to the formation of clusters, but also the emergence of the PDGFRα^{High} cluster patterns themselves: Pre-patterning of cluster sites is not required. In its current implementation the total volume of each phase is fixed, therefore the model does not account for proliferation or differentiation of new PDGFRα^{High} populations. Further, the current model assumes that viscous fluid-like characteristics dominate with negligible elasticity for all the tissues, which likely is an oversimplification and could potentially affect the realism of the model. In particular, consistent with numerous previous studies, the real epithelium is assumed to behave dominantly as elastic material. The key implication of an elastic epithelium is that it would impose an increasing restoring force as a function deformation against an encroaching cluster, thus potentially producing shallower contact angles than predicted from the surface energies of the phase separation model alone. Detailed studies on the mechanical properties of the constituent tissues will be needed to resolve the questions on the importance of elasticity in the clustering dynamics.

2.4.3 Vertex Cell-base Model

One of the biggest strengths of the phase separation model is that its continuum nature allows the model to stay simple and contain very few parameter inputs. It also directly addresses the tissue-scale dynamics, whose understanding is the ultimate goal of our modeling endeavors. This contrasts with cell-based approaches, where the tissue-level dynamics are only an emergent property of the model arising from the

simulation of a large number of cell-level interactions, which can obscure and make the understanding of tissue-level dynamics less than precise. However, the abstract nature of continuum models can lead to interpretative challenges and make it more difficult to include detailed cell-level processes in the model, should there be need. In the case of our phase separation model, one interpretative challenge was related to diffusive phase boundaries, which are hard to interpret in the context of real tissues, where each cell on a tissue boundary has a distinct identity. Another challenge related to cell-level processes was the apparent importance of the high motility of the clustering cells, and the general Brownian-like motion of the cells: The phase separation framework as implemented didn't allow us to freely assign differential motilities to the phases, nor did it allow for a clean implementation of random motion of the phases. For these reasons, we adapted a vertex model to describe the tissue dynamics, where the previous phase-separation concept is translated into units of cell-based behaviors (Barton et al., 2017; Bi et al., 2016), with the crucial addition that differential material motilities and random motion are trivial to implement.

In the vertex model, each cell is represented as a polygon, sharing its edges with its neighboring cells. Each edge is given different adhesion energies; more negative energy values representing more favorable interactions and more positive values representing less favorable or more repulsive interactions. At each time iteration, the cell centroids' locations are updated in the direction of minimizing overall tissue energy and accounting for random motility. As cell edges are recomputed at each iteration step, their cell-cell connection is independent of the prior connections, and the model represents more 'fluid-like' behavior of the tissue. As with the previously considered

models, we did not include changes in cell identity or increases in cell number (proliferation) in this model, therefore keeping the model as simple as possible and focusing on capturing the progression of how the PDGFRα^{High} differentiated layer breaks up into clusters and initiates the epithelial deformation. We assigned higher motility to the PDGFRα^{High} cells based on our observation from our earlier live-imaging data suggesting higher baseline motility, and lower interfacial energy between PDGFRα^{High} cells as we demonstrated that adhesion programs were upregulated and necessary for the process (likely acting through interstitial ECM molecules). When the initial condition of the tissue is set such that a layer of PDGFRα^{High} cells is sandwiched in between epithelium and mesenchyme, the layer breaks up into clusters over time, similarly to the prediction by the phase-separation model (**Fig. 2.19**A). We can now use this model to quantitatively predict the outcome of the development to test the necessity and the sufficiency of certain parameters, or to compare the computational predictions with biological experimental outcomes to validate or adjust our model framework. For example, when the differential cell motility (increased baseline motility of PDGFRα^{High} cells) is eliminated from the model, the PDGFRα^{High} cells no longer reliably break-up into clusters, suggesting the necessity of differential cell motility in driving the clustering phenomenon (**Fig. 2.19**B).

When adhesion hierarchy is impaired to the direction of uniform adhesion, the computational model predicts that the PDGFRα^{High} cells no longer form rounded clusters (**Fig. 2.19**C). This prediction is in close correspondence with the observations from explant tissue cultured in the presence of integrin $\alpha2\beta1$ inhibitor (**Fig. 2.12**A). In addition to motility and adhesion, changing the initial conditions can also be used to

generate predictions. For example, when the initial number of PDGFRα^{High} cells are reduced, the resulting clusters are predicted to be smaller but also more closely spaced. Conversely, when the initial number of PDGFRα^{High} cells is increased, the resulting clusters are predicted to be larger and more widely spaced apart (**Fig. 2.19**D). This scaling relationship was also observed in the explant tissues. When mesenchymal proliferation was reduced by treating the tissue with a proliferation inhibitor, mitomycin C, the explant tissue grew more number of smaller clusters, and correspondingly narrower villi. On the other hand, when the tissue was treated with BMP inhibitor Dorsomorphin, which has previously been shown to increase cluster size, there were fewer, but larger clusters of PDGFRα^{High} cells (**Fig. 2.19**E). It was previously reported that dorsomorphin induced the fusion of clusters (Walton et al., 2016); however, when we examined these tissue in whole mount confocal 3D reconstructions, we saw what had originally appeared like fusions by widefield imaging were actually larger clusters and elongated villi that were protruding across the lumen and seemingly overlapping with clusters on the opposite side of the gut tube. These results provide an alternative explanation to the observations that have previously been used to support a reaction-diffusion model of cluster patterning. Indeed, we additionally observe that PDGFRα^{High} cells remain proliferative in Dorsomorphin treated guts, suggesting a cellular basis for the enlarged clusters and villi. In addition, there are other tissue observations consistent with the model predictions. For example, cluster fusion of nascently forming clusters have been observed in live imaging of the tissue (**Fig. 2.19**F). Fusion of more aggregated nearby clusters also could occur according to the model. These data together suggest that differential motility and adhesion are important to cause cell

sorting phenotype that results in patterned cluster formation, and the model consistently predicts tissue behavior.

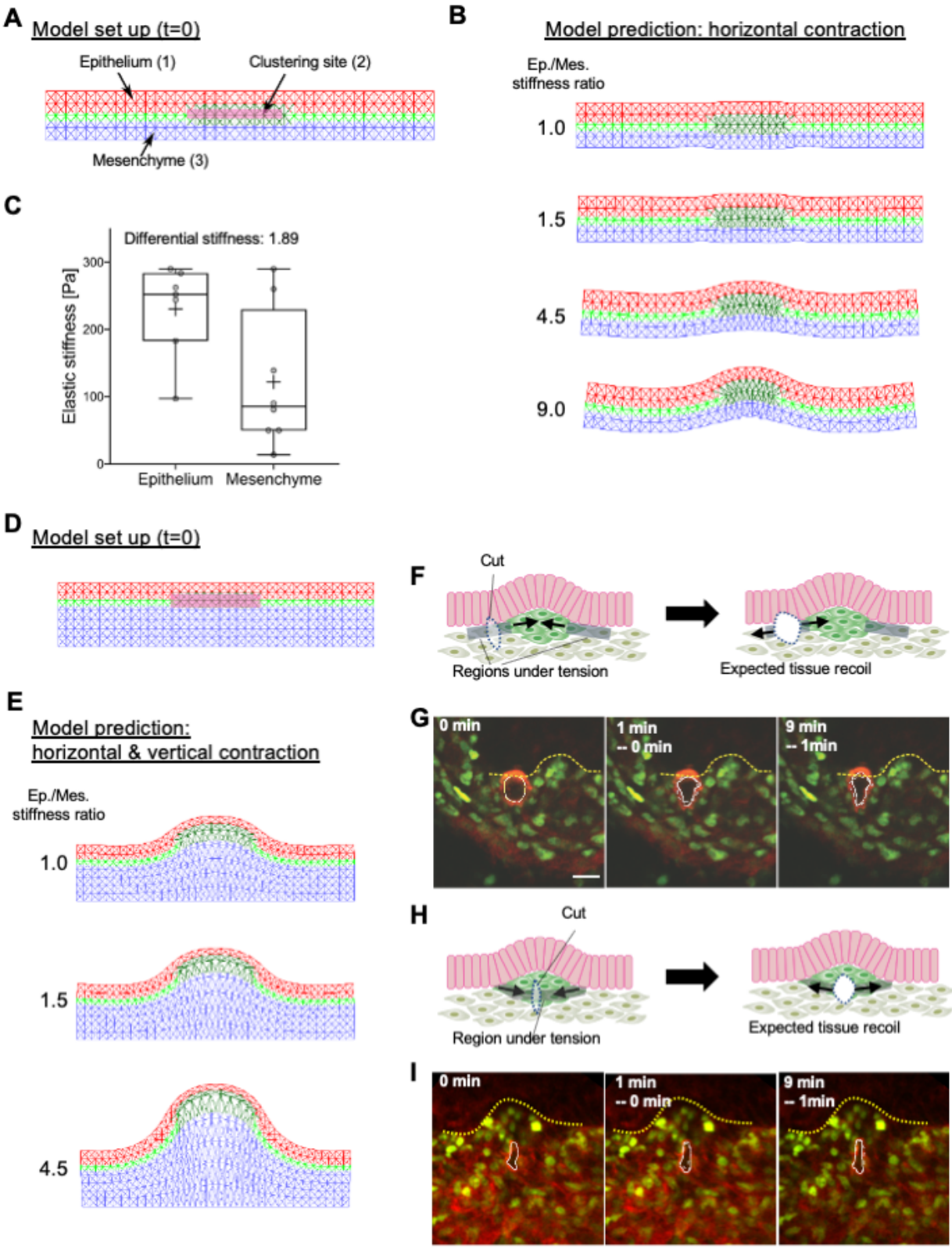
A
Model set up (t=0)
Epithelium (1)
Clustering site (2)
Mesenchyme (3)
B
Model prediction: horizontal contraction
Ep./Mes.
stiffness ratio
1.0
1.5
4.5
9.0
C
Differential stiffness: 1.89
Elastic stiffness [Pa]
300
200
100
0
Epithelium
Mesenchyme
D
Model set up (t=0)
E
Model prediction:
horizontal & vertical contraction
Ep./Mes.
stiffness ratio
1.0
1.5
4.5
F
Cut
Regions under tension
Expected tissue recoil
G
0 min
1 min
-- 0 min
9 min
-- 1min
H
Cut
Region under tension
Expected tissue recoil
I
0 min
1 min
-- 0 min
9 min
-- 1min

Figure 2.16 Model prediction by spring model and biological observations A. The two-dimensional spring model consisting of epithelial layer (1), pre-patterned clustering mesenchymal site (2), and the rest of mesenchyme (3) were constructed. Clustering was modeled by reducing the springs' resting lengths of the highlighted region. **B.** Model predictions with various epithelial-mesenchyme differential spring stiffness. Significant (>5 times) differential stiffness is required to obtain bending morphogenesis. **C.** Stiffness measurements of E14.5 intestinal epithelium and mesenchymal tissue regions by AFM. **D.** Spring model indicating 'active spring edges' under highlighted region. Both vertical and horizontal contractions are modeled in the pre-defined 'cluster regions'. **E.** Model predictions with various epithelial-mesenchyme differential spring stiffness. Differential stiffness of two tissue layers was no longer required to induce buckling morphogenesis when both vertical and horizontal contractions were modeled. **F-I.** Predictions and results of cut and recoil experiments. Illustrative prediction of tissue regions under tensile stress and result of cut & recoil experiments (F, H). Cut experiments in the region using laser ablation technique. Cut-opened regions are outlined. No obvious recoil was observed (G,I). Spring model was assumed representative of the villus morphogenesis (F,G). Morphogenesis mechanism driven by bridging of the epithelium by clustering mesenchyme was considered (H,I). Scale bar = 25 μm.

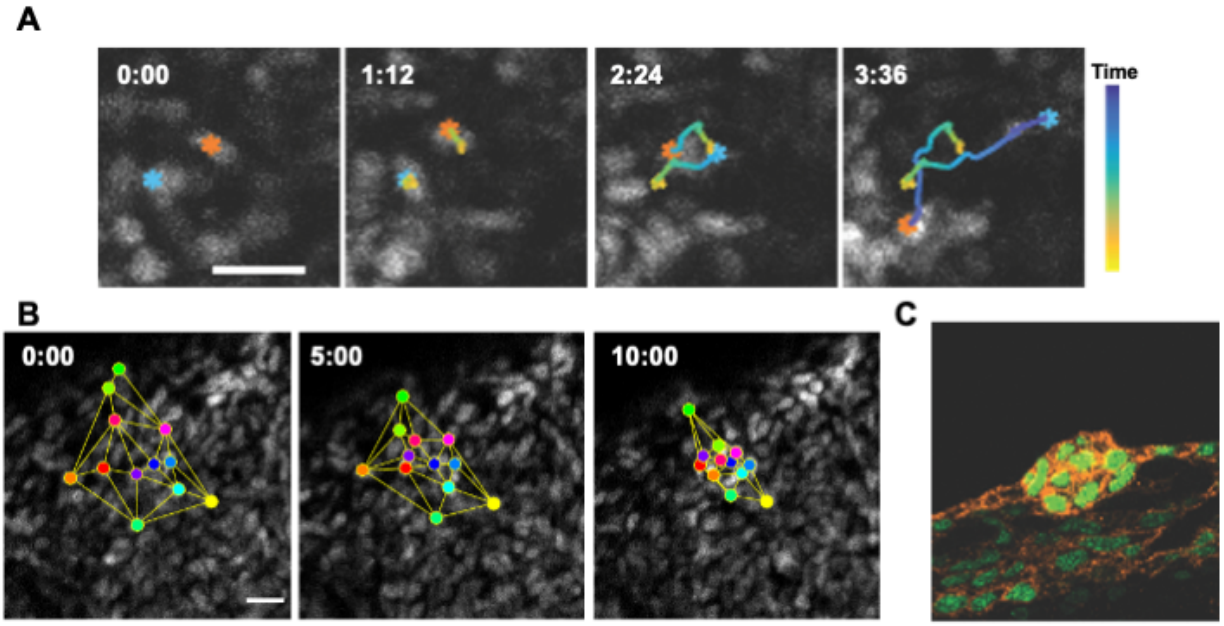

Figure 2.17 Evidence supporting liquid-like behavior of PDGFRα^{High} mesenchymal cells A. An example of a pair of individually tracked cells crossing their path. **B.** Triangulation of tracked clustering cells demonstrates the cells' neighboring triangulation is not maintained. Same tracked cells are color coded. **C.** *Pdgfra*^{EGFP} mesenchymal cell membrane stained with PDGFRα antibody. Cluster cell membrane borders are clear. Scale bars = 20 μm.

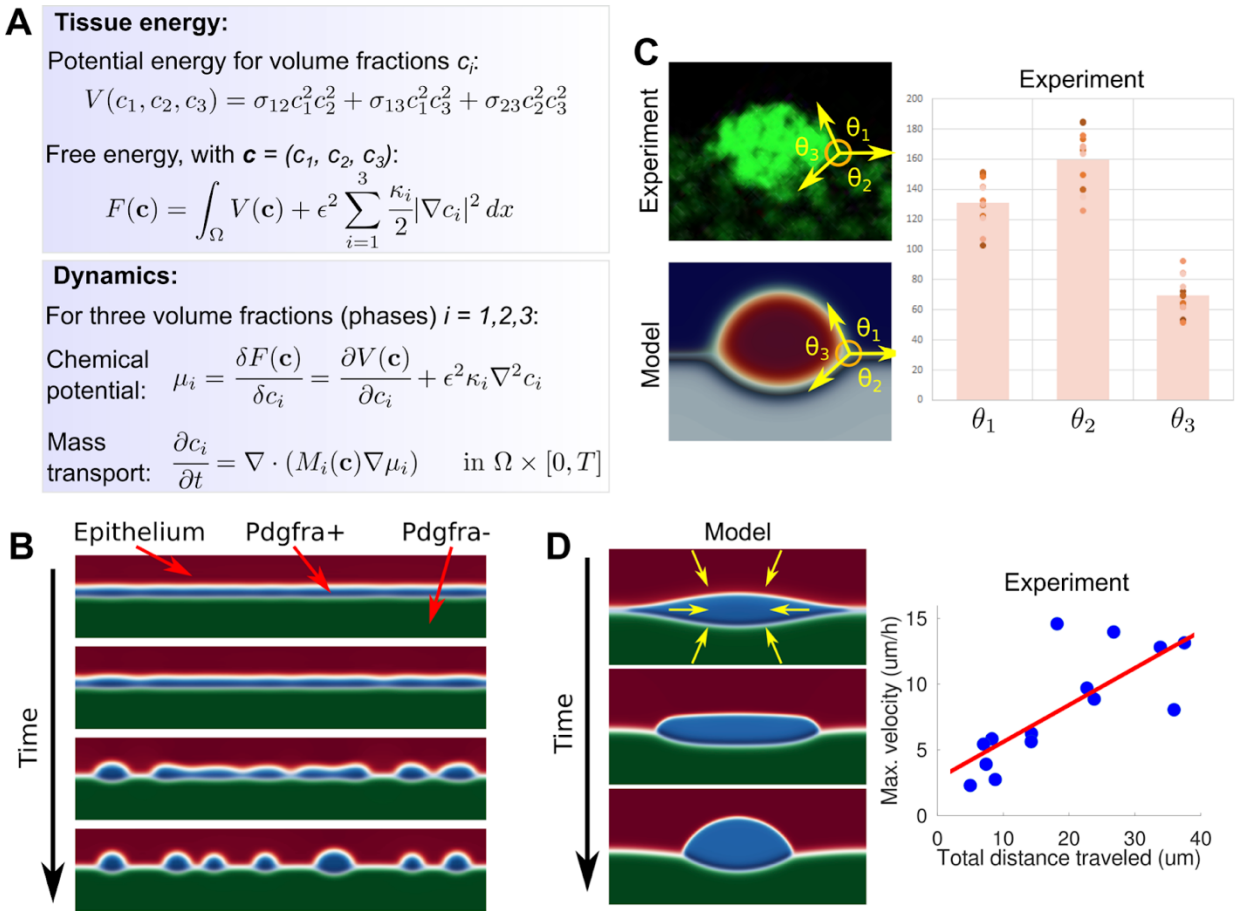

Figure 2.18 Phase separation model of villus patterning and folding A. A summary of the governing equations, motivated by the classical Cahn-Hillard model of phase separation. **B.** Simulation of the break-up of PDGFRα^{High} monolayer sandwiched between the epithelium and the rest of the mesenchyme. **C.** Analysis of the cluster contact angles for calibrating the surface energy parameters for the tissue simulations. **D.** Close-up of a single simulated cluster aggregation, showing the geometry progression as a function of time (left), and the quantification of the maximum clustering cell velocities as a function of total distance traveled (right).

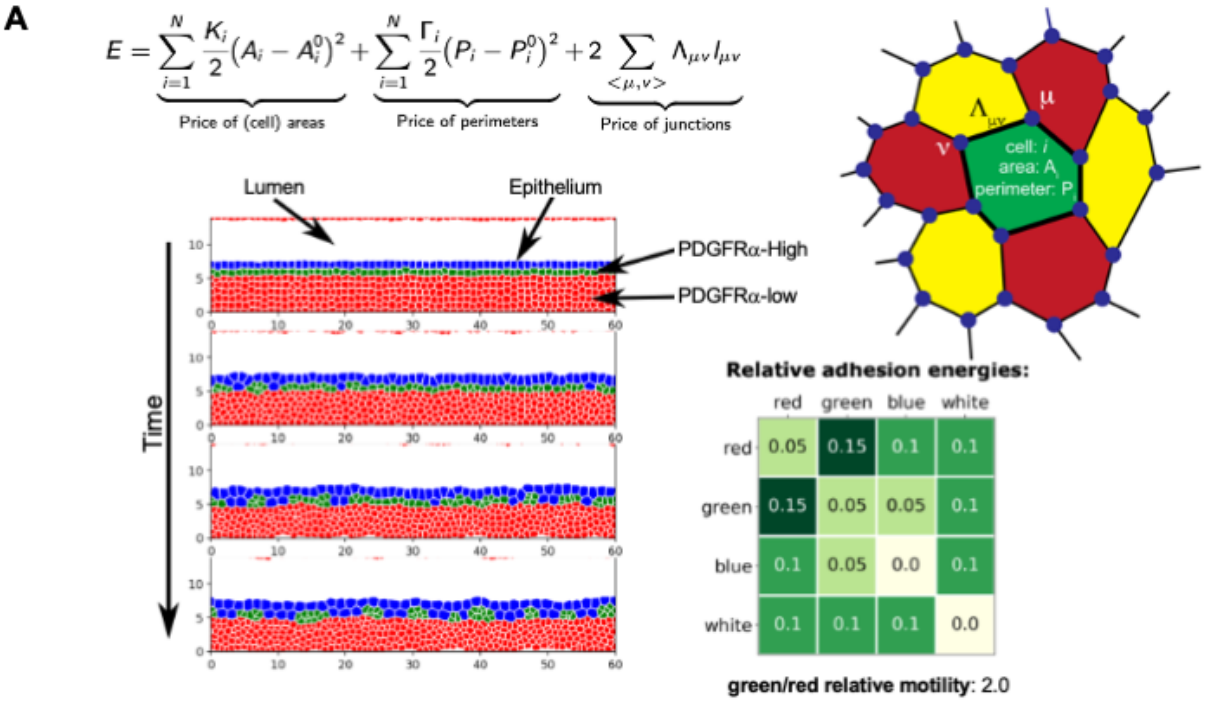
A
$E = \sum_{i=1}^{N} \frac{K_i}{2}(A_i - A_i^0)^2 + \sum_{i=1}^{N} \frac{\Gamma_i}{2}(P_i - P_i^0)^2 + 2 \sum_{<\mu,\nu>} \Lambda_{\mu\nu} l_{\mu\nu}$
Price of (cell) areas
Price of perimeters
Price of junctions
Lumen
Epithelium
PDGFRα-High
PDGFRα-low
Time
μ
ν
$\Lambda_{\mu\nu}$
cell: i
area: A_i
perimeter: P_i
Relative adhesion energies:
red green blue white
red 0.05 0.15 0.1 0.1
green 0.15 0.05 0.05 0.1
blue 0.1 0.05 0.0 0.1
white 0.1 0.1 0.1 0.0
green/red relative motility: 2.0
B
Green/red relative motility: 1.0
C
red green blue white
red 0.05 0.1 0.1 0.1
green 0.1 0.1 0.1 0.1
blue 0.1 0.1 0.0 0.1
white 0.1 0.1 0.1 0.0
D
Initial cell density
E
Less cells
Control
More cells
F
0:00
4:00
8:00

Figure 2.19 Vertex model predictions of villus morphogenesis and biological observations A. Overview of the vertex model implemented. Cell area, perimeters, and adhesions at each cell-cell interface are assigned energy and the model tries to minimize its overall energy at each iteration (top left and top right). Implementation of the model and progression of cluster breakup predicted by the model (bottom left). Adhesion energy and relative motility assigned to each cell component. **B.** When the relative motility is not present, the cluster breakup is not predicted to occur. **C.** Prediction when the adhesion of PDGFRα^{High} cells are reduced. Assigned adhesion energy for the simulation (right). **D.** Simulation outcome when the initial cell density is altered. Increasing initial PDGFRα^{High} materials is expected to result in bigger clusters. **E.** Explant tissue of reduced (mitomycin C treated) and increased (Dorsomorphin treated) PDGFRα^{High} cell populations show narrower and thicker villus, respectively. **F.** Fusion of two clusters was observed and tracked over time. Observed fusing clusters before and after fusion are outlined.

2.5 Application to an engineered *in vitro* living model system

PDGFRα expressing intestinal mesenchymal cells, when isolated and embedded into Matrigel at high density, self-organize to form cell aggregates that resemble the villus clusters observed in vivo (**Fig. 2.20**) (Rao-Bhatia et al., 2020). However, as there are relatively few PDGFRα^{High} cells per gut, and the conditions for expansion/long term culture of these cells whilst maintaining their identities have not been identified, acquiring a sufficient number of cells for experimentation remains challenging. Mouse embryonic fibroblasts (MEFs) are mesenchymal cells derived from embryonic mice that share some characteristics of PDGFRα-expressing mesenchymal cells. For example, they are highly contractile and form clusters when cultured on ECM-based gels (**Fig. 2.21**A), and when cultured in between layers of ECM gels, form clusters with a cross-sectional view resembling the initiating villus (**Fig. 2.21**B). Therefore, we employed MEFs as an *in vitro* model by which to study the cellular basis of patterned cluster formation.

By employing DNA-programmed assembly of cells (DPAC), we were able to pre-pattern cells to specific designs of interest embedded in the surface of ECM substrates (Cabral et al., 2021; Todhunter et al., 2015). The engineered system has some advantages over explants or *in vivo* tissue systems, as there are less actively co-evolving components, and we have more precise control over the initial conditions as well as the ability to genetically manipulate cells. Using DPAC, MEFs were placed in the formation of lines in Matrigel and were cultured. We observed that the lines of MEFs break up into clusters (**Fig. 2.21**C). When the cell-based vertex model is applied to this simplified system, the *in vitro* behavior was well captured: a line of motile and adhesive

cells placed in between non-motile substrates is predicted to break-up into clusters (**Fig. 2.21**D). The behavior was also dependent on integrin-based adhesion, as treatment with the integrin $\alpha 2\beta 1$ inhibitor, TCI15, resulted in failure to break-up into clusters both *in vitro* and *in silico* simulation (**Fig. 2.21**E,F). Scaling relationships were also tested in the *in vitro* system. When the width of the initial coverage is decreased, both the *in vitro* DPAC model and computational model resulted in smaller clusters (**Fig. 2.21**G). When the width of the initial cell coverage is increased on the other hand, similar to conditions where gut explants are cultured with dorsomorphin, the model predicted formation of larger more spaced apart clusters. They again resulted in cluster size and spacing that are consistent to the predictions by the computational model (**Fig. 2.21**G).

These results demonstrate that the adhesion dependent model framework constructed earlier for intestinal mesenchymal clustering and villus morphogenesis is robust and applicable to predict other similar cellular behavior.

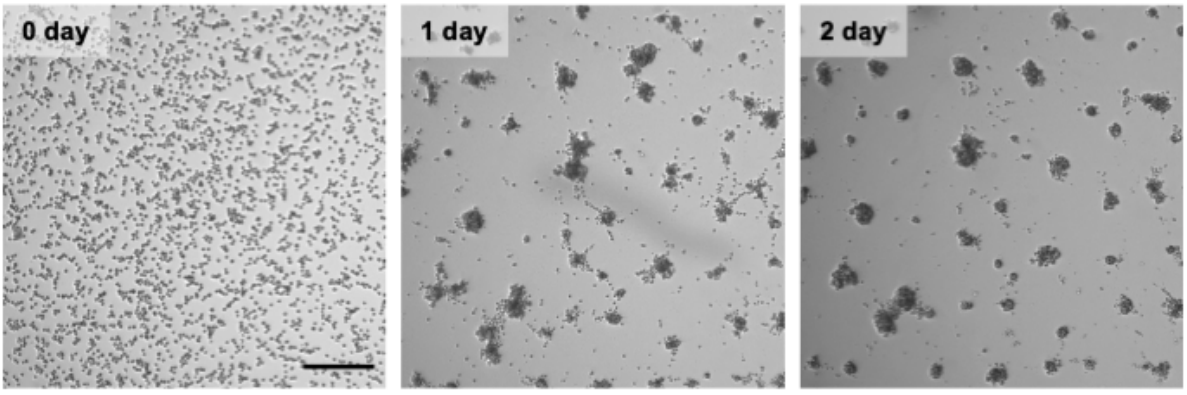

Figure 2.20 Sorted *Pdgfra^{EGFP} cells* seeded in Matrigel surface break up into clusters
Scale bar = 200 μm.

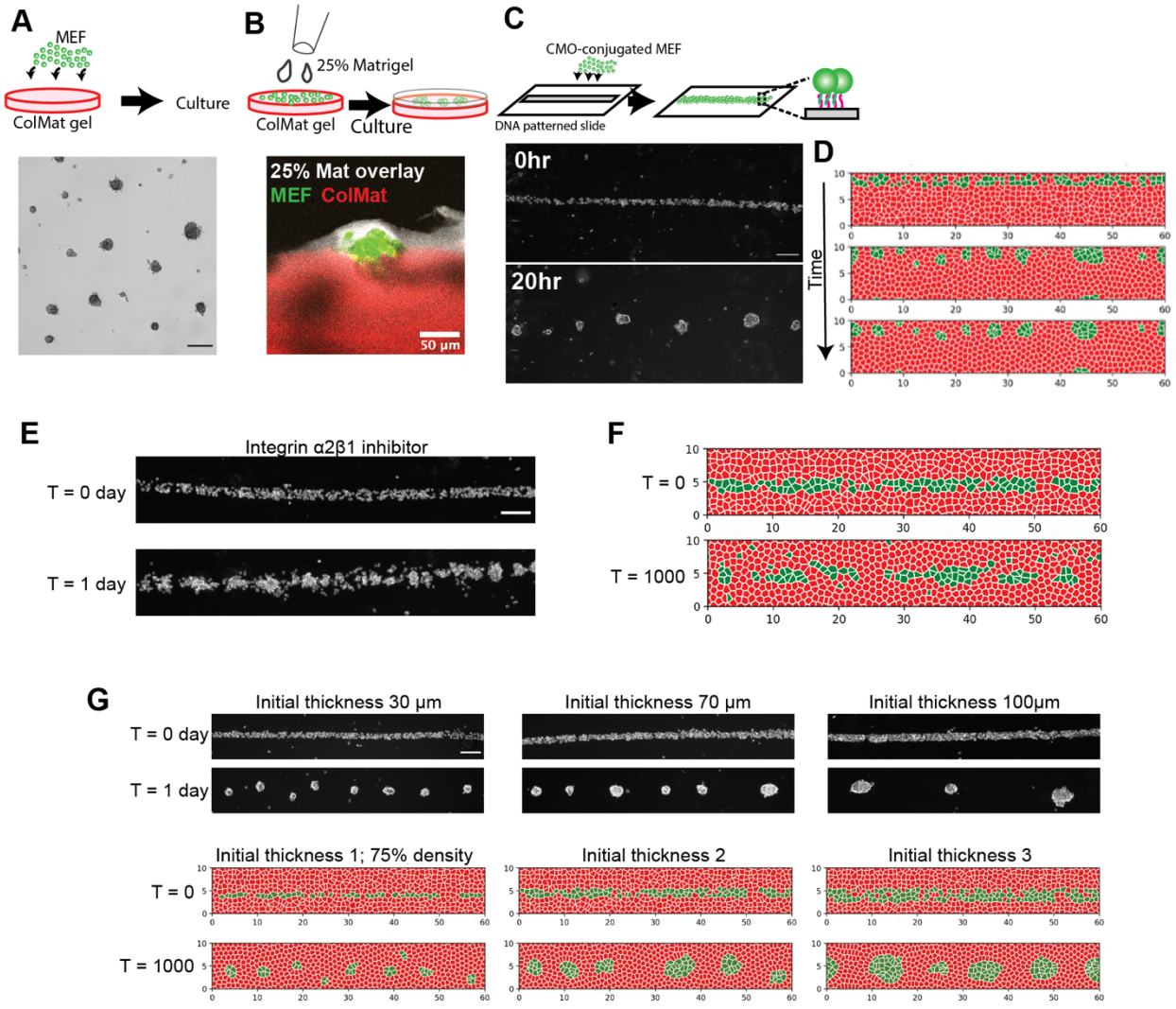

Figure 2.21 Comparison between *in vitro* engineered MEF clustering and computational predictions A. Mouse embryonic fibroblasts (MEFs) seeded on solidified ECM gel surface composed of 1mg/mL Collagen mixed into Matrigel. MEF cells break up into clusters similarly to sorted PDGFRα cells. Scale bar = 100 μm. **B.** Cross-section view of the MEF cells cultured in between two layers of ECM gels. MEF cells were seeded onto solidified 1mg/mL Collagen mixed in Matrigel, and covered by 25% diluted Matrigel and cultured for 2 days. Scale bar = 50 μm. **C.** Simplified illustration of DPAC process (top) and the result of the DPAC patterned lines of MEF cells cultured in Matrigel (bottom). Scale bar = 200 μm. **D.** The cell-vertex model was constructed to simulate *in vitro* DPAC experiments. **E.F.** Adhesion inhibition by treatments with integrin α2β1 inhibitors resulted in a failure to break the lines up into clusters in *in vitro* experiments (E) and in *in silico* simulation (F). **G.** Scaling relationships between initial cell line widths and cluster size are observed and predicted in both *in vitro* (top) and computational simulations (bottom).

3. Material and Methods

Mouse genetics

All animal experiments were performed in accordance with the guidance established by Institutional Animal Care and Use Committee (IACUC) and Laboratory Animal Resource Center (LARC) of University of California, San Francisco, CA, USA. The following mouse strains were used: C57BL/6J (Jackson Laboratory: 000664); *Pdgfra*^{EGFP} ; *Shh*^{Cre} ; *Twist2*^{Cre}; *Pdgfra*^{CreER}; *β-Act*^{Cre}; *Myh9*^{flox}; *Myh10*^{flox}; *Myocd*^{flox}; *Rosa26*^{tdTomato}; *Rosa26*$^{mT/mG}$. Official gene symbol and MGI information of the mice are summarized in **Table 3.1**. To generate *Myh9*$^{null/+}$ and *Myh10*$^{null/+}$ mouse, *Myh9*^{flox} and *Myh10*^{flox} mouse were first crossed with *β-Act*^{Cre} and *β-Act*^{Cre} allele was bred out from the offspring. For generation of embryos, the observed plug date was considered embryonic day 0.5. Tamoxifen (0.15 mg/g of body weight) was administered via oral gavage to pregnant dams at E11.5, E12.5 and E13.5 to induce genetic recombination.

Explant Culture

Embryonic intestines were harvested at E13.5 and grown in culture as described (Walton and Kolterud, 2014). Briefly, intestines were placed on 8.0 μm pore-size transwells (Falcon or Corning) in fetal gut media (BGJb media containing 0.1 mg/mL ascorbic acid) with or without pharmacological inhibitors and cultured for 24-72 hours at 37°C with 5% CO_2. For Edu incorporation assay, 10 μM of Edu (Invitrogen, C10637) were added to the media 2 hours prior to experimental end point and tissue fixation. At experimental end time point, explants were rinsed, fixed with 2 – 4% paraformaldehyde

for 2 hours at room temperature or 4 hours – overnight at 4°C. To monitor the development of tissue, images were taken on Leica DMi8 epifluorescence microscope.

Table 3.1 Summary of mouse genetics utilized in the study

	Official symbol	MGI	Reference
Pdgfra^{EGFP}	Pdgfra$^{tm11(EGFP)Sor}$	J:83560	(Hamilton et al., 2003)
Shh^{Cre}	Shh$^{tm1(EGFP/cre)Cjt}$	3053959	(Harfe et al., 2004)
Twist2^{Cre}	Twist2$^{tm1(cre)Dor}$	3044412	(Šošić et al., 2003)
Pdgfra^{CreER}	Pdgfra$^{tm1.1(cre/ERT2)Blh}$	6201731	(Chung et al., 2018)
β-Act^{Cre}	Tmem163$^{Tg(ACTB-cre)2Mrt}$	2176050	(Lewandoski et al., 1997)
Myh9^{flox}	Myh9^{tm5Rsad}	4838521	(Jacobelli et al., 2010)
Myh10^{flox}	Myh10^{tm3Rsad}	3052104	(Ma et al., 2004)
Myocd^{flox}	Myocd^{tm1Msp}	3773717	(Huang et al., 2008)
Rosa26^{tdTomato}	Gt(ROSA)26Sor$^{tm14(CAG-tdTomato)Hze}$	3809524	(Madisen et al., 2010)
Rosa26$^{mT/mG}$	Gt(ROSA)26Sor$^{tm4(ACTB-tdTomato,-EGFP)Luo}$	3716464	(Muzumdar et al., 2007)

Live imaging

Pdgfra^{EGFP} and *Shh^{Cre}; Pdgfra^{EGFP}; Rosa26^{tdTomato}* reporter mice were used to visualize mesenchymal cell clusters and epithelial layer. Embryonic intestines were harvested and longitudinally cut open using tungsten needles (127 μm diameter, A-M systems) and cultured on transwell membranes with epithelial surface up. Either 200 μM SNP or 60 μM Nifedipine were added to the culture media to minimize tissue movement due to peristalsis. Images were acquired using 4x (0.4NA) AZ Plan Apo Air objective with both

optical and digital zooms for 10-20 hours. Images were taken every 10-12 minutes on a Nikon AZ100M with an environmental chamber.

Data analysis of live imaging data

For the analysis of curvature and cluster relationship, live imaging data obtained with *Shh^{Cre}; $Pdgfra^{EGFP}$; $Rosa26^{tdTomato}$* reporter mice tissue was used. Regions of interest at curled edges of the tissue that allowed for visualization of both epithelial and mesenchymal layers in an optical plane were selected, and optical sections with the clearest epithelial-mesenchymal boundary were used for the analysis. For epithelium curvature measurement, the epithelial-mesenchymal boundary was traced manually. The traced lines were further analyzed on MATLAB by fitting circles to compute local curvatures using custom script (**Fig. 3.1**A). In order to measure clustered profile of mesenchymal cells, 90% mesenchymal dispersion distance was used. These values were computed by analyzing 60 μm x 60 μm square regions of mesenchyme adjacent to the epithelium. Nuclei occupied regions were identified by converting the original data into binary image using ImageJ, and dispersion of occupied pixels from its center of mass were computed using MATLAB custom code. When cell nuclei are well-dispersed, nuclei containing pixels are expected to be dispersed throughout the region of interest, increasing the distance of 90 percentile pixel location from the center of mass. On the other hand, when mesenchyme's clustered profile dominates the region, more numbers of nuclei occupying pixels are expected to concentrate around the center of mass, decreasing the distance of the 90 percentile pixel location (**Fig. 3.1**B).

For the mesenchymal nuclei tracking, the images were first corrected for tissue drift and movement using StackReg plugin (Thevenaz et al., 1998) on ImageJ. The cell nuclei were then tracked manually using the 'Manual Tracking' plugin on ImageJ. Cell coordinates were saved as .csv files and further analyzed or overlayed on original images on MATLAB using custom code. For cell speed and GFP pixel value analysis, to minimize noise due to technical limitations, distance moved over an hour (over 5 timeframes) and average of GFP pixel values over an hour were computed and used. To compare baseline motility of clustering vs non-clustering cells, data points with hourly speed below 10 μm/hr were used for the analysis.

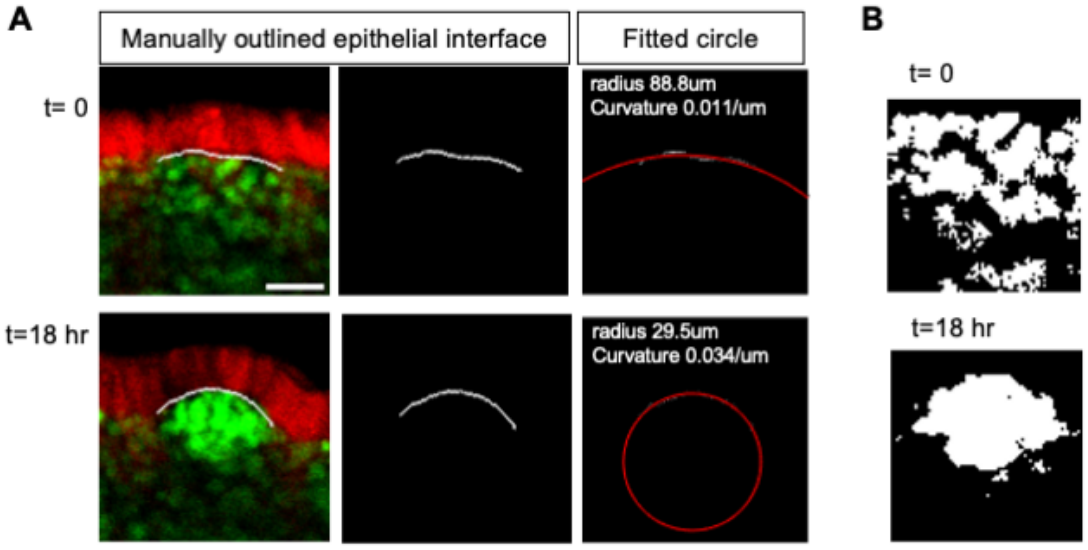

Figure 3.1 Examples of curvature and 90% dispersion distance analysis A. Epithelial curvature was computed by first manually outlining the epithelial interface and fitting a circle to the line. B. Dispersion measurements were done on binary processed images of mesenchymal *Pdgfra*^{EGFP} nuclei.

Tissue fixation and immunostaining

Tissues were fixed for 2 hours at room temperature or for 4 hours – overnight at 4°C in 2-4% PFA. For frozen sections, tissues were transferred to 30% sucrose and embedded in OCT, and sectioned at 10 µm - 50 µm slices using cryostat to generate thin and thick sections. Tissue sections were stained using standard immunofluorescence protocols with modified lengths of incubation for thicker sections. After immunofluorescent staining, EdU+ cells were detected using Click-iT Plus EdU Assay Kit (ThermoFisher, C10640). Images were taken on either Leica DMi8 epifluorescence, Zeiss spinning disk, Zeiss LSM800 or LSM900 confocal microscope.

Single cell sequencing

Embryos with *Pdgfra*^{EGFP} genotype were used for the experiments. Small intestines were dissected from E13.5 – E18.5 embryos and cut into 2.5mm length segments. Number of tissues used and segments obtained from each tissue is summarized in **Table 3.2**. Each tissue segments were dissociated to single cells in HBSS buffer containing 10mM HEPES, 1% BSA, 0.3mg/mL DNase and 0.1W/mL Liberase TL on an orbital shaker at 37C for 30 min with trituration with P200 pipette every 15 mins. Single-cell suspensions were then transferred to 96-well U-bottom plates and washed twice in fetal gut media to remove any remaining BSA. MULTI-seq lipid barcode labeling was performed in 96 well plates following the MULTI-seq protocol (McGinnis et al., 2019b). Once the cells are incubated with lipid modified oligos (barcode, anchor and co-anchor) in total of 100 µL volume reaction, 150 µL of HBSS with 2% BSA solution were added to quench the reaction and pooled together in 15ml conical tubes. The cells were pelleted

and stained with APC/Cy7 anti-mouse Ter119, APC anti-mouse CD31, BV605 anti-mouse CD45, PE/Cy7 Epcam (all from Biolegend) for 30min on ice followed by a wash with FACS buffer. The cells were resuspended in FACS buffer with DAPI to stain dead cells and passed through a 35um cell strainer. Using BD FACS Aria II, live ($DAPI^{-}$, $Ter119^{-}$) cells as well as enriched rare cells ($CD31^{+}$, $CD45^{+}$, $Epcam^{+}$, or GFP^{High}) were sorted separately in a desired ratio. 35,000 cells were loaded to each well of GEM chip (2 wells of live-sorted cells and 1 well of enriched rare cells for each experimental day) for single-cell capture using the 10x Chromium Single Cell 3' Reagent Kit V3 (10X Genomics) for aimed target recovery of 20,000 cells per well. Library preparation for both cDNA and MULTI-seq barcodes were performed following 10X library preparation protocol along with MULTI-seq library preparation protocol. Libraries were pooled and subjected to sequencing in a single lane of an Illumina NovaSeq6000 for each experiment. Sequencing data was processed, and downstream analysis performed as described below.

Table 3.2 Summary of tissue segments and replicates obtained from each tissue for the single-cell sequencing experiment.

Stage	# Segments	# Replicates	Collection day
E13.5	3	4	2
E14.5	5	3	2
E15.5	10	2	1
E16.5	15	2	1
E18.5	20	2	2

Processing FASTQ Files, Assignment of barcodes, Quality Control and Doublet Removal

Expression library FASTQs were pre-processed using cellranger count (10X Genomics) and aligned to the mm10 mouse reference transcriptome using default parameters. Read-depth normalization between 10x Genomics lanes was then performed using cellranger aggr (10x Genomics). Aggregated raw RNA UMI count matrices were then analyzed using Seurat (Stuart et al., 2019; Hafemeister et al., 2019), excluding cells with < 1e3 total RNA UMIs and genes with <= 3 total counts across cells. Cells were further filtered to remove gene expression clusters associated with high proportions of mitochondrial reads and/or low total RNA UMIs. Using this filtered set of cell barcodes, MULTI-seq FASTQs were then pre-processed and subjected to the sample classification and semi-supervised negative cell reclassification workflows as implemented in the deMULTIplex R package (McGinnis et al., 2019b). MULTI-seq sample classifications were then mapped onto gene expression space to identify clusters enriched for inter-sample doublets which were cross-validated using DoubletFinder (McGinnis et al., 2019a). The final scRNA-seq dataset was then generated by filtering cells using the final criteria: removing cells that were (i) classified by MULTI-seq as doublets or negatives, (ii) assigned to doublet-enriched clusters, or (iii) exhibited >= 10% mitochondrial gene content.

Data integration, cell annotation and downstream analysis

Seurat objects were normalized using SCTransform methods (Hafemeister and Satija, 2019). Integration of Seurat objects from two different experimental days were

performed following the Seurat integration workflow. Cells and clustering were visualized using Uniform Manifold Approximation and Projection (UMAP) dimensional reduction methods. To further analyze cells in specific clusters of interests, identified clusters were subsetted, integrated and re-clustered for downstream analysis and visualization. Cluster annotation was achieved by presence of known markers and based on identified marker genes (Haber et al., 2017). To identify marker genes of PDGFRα-High 1 population in the subepithelial mesenchymal cell population, differentially expressed genes were identified by comparing PDGFRα-High 1 to PDGFRα-low 1 population. The list of differentially expressed genes were then analyzed for functional enrichment analysis using g:Profiler to identify upregulated KEGG terms (Raudvere et al., 2019). Pseudotime inferences were made and gene expressions were fitted along the trajectory using Slingshot (Street et al., 2018) and tradeSeq (Van den Berge et al., 2020), respectively.

In-situ hybridization

For in-situ hybridization, 12 µm cryosections from E15.5 and E16.5 tissue were generated as described in 'Tissue fixation and immunostaining'. Sections were stained using the RNAScope HiPlex8 Detection Kit(Advanced Cell Diagnostics, Cat. No. 324100) with the following adjustments to the manufacturer's protocol (fixed frozen tissue sample): Post-fixation time in 4% PFA was increased to 90 minutes, and the target retrieval step was performed while keeping the slides horizontal. Probes used against mouse RNA include *Fabp1* (enterocyte marker), *Agr2* (Goblet cell marker), *Cck* (Enteroendocrine cell marker). Additional proves not included in figures: *Npnt*

(Differentiated PDGFRα), *Ccl11*(Transitioning mesenchyme), *Ebf1* (Unidentified population of mesenchyme), *Cdh2* (Neuron marker), and *Elavl4* (Neuron marker #2). Images were acquired using Plan Apo VC 100x/1.4 Oil objective with Nikon DS-Qi2 monochrome camera on a Nikon Ti Inverted Microscope. Deconvolution was performed using Huygens Deconvolution software. Channels with two different rounds of staining were aligned using HiPlex image Registration Software provided by Advanced Cell Diagnostics.

qRT-PCR

For mRNA measurement by qRT-PCR, *Pdgfra*^{CreERT}*; Myh9*$^{flox/flox}$*; Myh10*$^{flox/flox}$*; Rosa26*$^{mT/mG}$ and *Pdgfra*^{CreERT}*; Myh9*$^{flox/+}$*; Myh10*$^{flox/+}$*; Rosa26*$^{mT/mG}$ mice at E15.5 were used. Tamoxifen was administered to the pregnant dams at E11.5, E12.5 and E13.5. Intestines were isolated and digested into single cells as described in 'Single-cell Sequencing'. 5,000 mesenchymal cells were collected into RLT lysis buffer (Qiagen) using BD FACS Aria II by sorting for mT/mG recombined cells. RNeasy Mini kit (Qiagen) and The High capacity cDNA Reverse Transcription Kit (ThermoFisher) were used according to manufacturer's protocols to purify mRNA and convert them into cDNA. Quantitative PCR was performed using iTaq Universal SYBR® Green Supermix (Biorad) on a Biorad CFX384. Test gene values were normalized to Gapdh, a housekeeping gene, values. Fold changes relative to control were calculated using the DDC_T method. Predesigned prime time qPCR primers were purchased from IDT. Following primers were used for the experiments: *Myh9* (Mm.PT.58.8415709), *Myh10*(Mm.PT.58.17097401), *Myh11*(Mm.PT.58.9236105), and *Gapdh*(Mm.PT.39a.1).

Atomic Force Microscopy (AFM) stiffness measurement

Fresh tissue was used for the stiffness measurement with AFM. Tissue sample was prepared by embedding isolated intestine into 6% agarose and making 200um sections using vibratome. The sections were mounted on a glass slide with Vetbond Tissue Adhesive (3M) and were encircled with a hydrophobic barrier using a ImmEdge pen to allow for incubation in media solution. Atomic Force Microscopy (AFM) analysis was done with a MFP3D-BIO inverted optical AFM mounted on a Nikon TE2000-U inverted fluorescent microscope (Asylum Research) as described previously (Lopez et al., 2011). Indentation was performed with a pyramidal silicone nitride cantilever with a nominal spring constant of 0.06 N/m attached with a borosilicate glass sphere of 20 μm in diameter. Probes were calibrated with the thermal noise method (Hutter and Bechhoefer, 1993) before each experiment. While in fetal gut media, samples were indented with a trigger point of 1 V and single force indentations were obtained with IGOR PRO build supplied by Asylum Research. The Hertz model (Hertz, 1882) was used to determine the elastic modulus of the tissue, with the assumption that cells were incompressible and using a Poisson's ratio of 0.5. With the microscope, we determined the location of the indentation by looking whether the tip was at the mesenchyme tissue versus the epithelial tissue (**Fig. 3.2**).

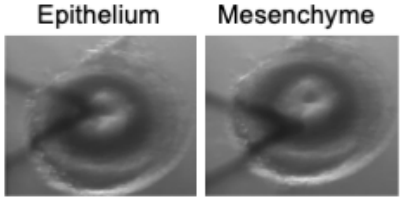

Figure 3.2 Example images of stiffness measurement of targeted tissue location The location for the indentation were targeted and identified by visually locating the tip of the cantilever in the microscope view.

Implementation of FEM, Phase separation, and Vertex models

The spring model was implemented in Matlab R2018b with the methods available in the default installation (no toolboxes used). The phase-separation model was implemented in Python 3 using the FEniCS 2019.1.0 library for solving the model equations and Matplotlib 3.1.0 for visualization. The vertex model was implemented in Python 3 using libraries including NumPy and SciPy for mesh handling and solving the model equations, Numba for optimizing the code performance, and Matplotlib for visualization. All the simulations were performed on a desktop PC with Intel i7-3770K CPU and 32G of RAM, and a 2015 MacBook Pro laptop with 16G of RAM. The simulations were generally not memory intensive, but the choice of spatial resolution in the vertex model was CPU-limited. The spring model and the vertex model used the first-order explicit Euler method for time integration, while the phase-separation model used the second-order implicit Crank-Nicolson method.

Laser ablation experiment

Freshly harvested E14.5 tissue with *Pdgfra*^{EGFP}*; Rosa26*$^{mT/mG}$ genotypes were used for the experiments for fluorescent visualization. Intestines were cut into 250 μm thick cylindrical tubes and embedded on the surface of 0.7% agarose gel and immersed in fetal gut media. The tissue was placed on an environmental setup for the duration of the experiment. Nikon A1R upright laser scanning two-photon microscope with Apo LWD 25x/1.1 water-immersion objective was used. 800 nm wavelength with maximum laser power with 1/8 frame per second scanning speed was used to make ablation on

targeted regions of interest (ROI). Immediately after the ablation, the entire tissue region was imaged at 920 – 960 nm wavelength with 20-30% laser power with ¼ frame per second scanning speed every minute for 10 timeframes.

PDGFRα$^+$ cells *in vitro* spheroid formation assay

GFP+ cells (including both high and low GFP-expression) from *Pdgfra*^{EGFP} intestinal tissue were collected as described in 'Single cell sequencing'. The isolated cells were cultured in Matrigel as described previously (Rao-Bhatia et al., 2020). In short, sorted cells were added to the surface of Matrigel at 10,000 cells/ µL density in MEF medium. Once the Matrigel is solidified at 37°C, the cells embedded on the Matrigel surface were cultured in MEF medium for multiple days.

MEF culture and cluster formation assay

Mouse embryonic fibroblasts (MEFs, male and female mixed, gift of Jay Debnath, UCSF) expressing maxGFP via pSicoR-Ef1a- maxGFP-Puro (gift of Justin Farlow, Serotiny Bio) were maintained in MEF medium and cultured on polystyrene flasks at 37°C and 5% CO2 (Corning). MEF medium is composed of Dulbecco modified Eagle's medium (DMEM) with 10% fetal bovine serum (FBS). To induce cluster formation, MEF cells in single cell suspension were cultured on solidified Matrigel surface at 3 x 10^4 cells/cm^2 density and incubated overnight in MEF medium at 37°C and 5% CO_2 for 15-24 hours.

For sandwich assay, Matrigel was fluorescently labeled using 1mg/mL AlexaFluor 555 NHS ester in DMSO (ThermoFisher Scientific A37571) at the final concentration of 2.5

μg/mL. MEF cells were seeded and incubated for one hour to allow for cells to adhere to the Matrigel surface. Medium was removed and replaced with 25% Matrigel that are fluorescently labeled with AlexaFluor 647 NHS ester (ThermoFisher Scientific A37573). The samples were incubated for another hour to let the matrigel solidify before MEF media was added and cultured for 1 to 2 days. For cross-sectional view images, the engineered tissue was embedded in 2% agarose gel and solidified. The agarose embedded tissue was then sectioned by a razor blade and the sliced gels were placed on a glass bottom plate for visualization.

Pre-patterning of MEF cells on ECM substrate using DPAC

Protocol previously described was followed to pattern MEF cells to Matrigel surface (Cabral et al., 2021). In short, photo masks of varying line widths were designed using AutoCAD (AutoDesk) and fabricated by CAD/Art Service Inc. The design was patterned to aldehyde-functionalized slide using positive photoresist, photomask and UV-light. Amine-modified DNA was added to the pattern, incubated and reductive amination reaction was performed to covalently bind the DNA pattern on the slide before removing photoresist. Once the slides are washed and made hydrophobic, the PDMS flow cells were placed on the slide. MEF cells were trypsinized and made into single-cell suspension and labelled with DNA sequences complementary to DNA on the slides using cholesterol modified oligos. These cells were applied to the DNA patterned slides in high density through the flow cell to make patterned cells on the slide. Excess cells were washed out and replaced by Matrigel containing 2% DNase (LifeTechnologies AM2238). Once the Matrigel sets, the sheets of Matrigel containing patterned cells were

isolated using a razor blade and placed on Matrigel coated plastic 6-well plate with cell-side-up. The plate with hydrogel sheets was incubated for 30 minutes at 37°C without media. Once the gels are attached to the plate, MEF medium was added and the patterned MEFs on Matrigel sheets were cultured overnight. The brightfield images of patterned cells were acquired before and after the experiment with a 2.5x objective using Zeiss Axio Vert A1.

4. Discussion

4.1 Discussion

Several signaling pathways play critical roles during intestinal villus morphogenesis, yet a mechanistic understanding of how they regulate cellular behaviors to drive morphogenesis has been lacking. This thesis research revealed key cellular programs required for mesenchymal cell clustering that initiate vilification.

Through the comprehensive investigation by my collaborators and I, we revealed that (i) the PDGFRα^{High} mesenchymal cell clustering is mechanically active and is the initiator of villus morphogenesis and (ii) adhesion and actomyosin activities are upregulated and required for proper cluster formation. Further, through computational simulations we have demonstrated that increased adhesion and motility among PDGFRα^{High} mesenchymal cells are sufficient in theory to explain the patterning and formation of clusters that initiate villus morphogenesis. Finally, simplified *in vitro* systems constructed of adhesive and contractile mesenchymal cells, MEFs, and inactive ECM confirmed the reliability and applicability of our suggested model framework outside of villus morphogenesis.

Previously, intestinal tissue mechanics have been studied by assuming that the tissues behave as elastic solids (Shyer et al., 2013). Our investigation, however, suggested that tissue undergoing PDGFRα^{High} cell clustering and initiation of villus morphogenesis exhibit more fluid-like behavior; the clustering PDGFRα^{High} cells undergo long distance motion involving neighbor exchange, and the tissue does not store evident tensile stresses. In reality, most biological tissues are neither purely elastic

nor purely fluid-like, but rather a combination of both. Our model has applied the basic principle proposed by Steinburg in the 1960s that analogizes cell sorting behavior with behavior of liquids wherein differential interfacial adhesion drives the sorting of cell populations. These principles have been used to describe cell sorting behavior within a cell aggregate of mixed cell population such that cells sort to the inside or outside layer of the aggregate (Steinberg, 1963). In our implemented model, we have assigned initial conditions such that instead of starting as an aggregate, the tissue is modeled as layers of cells with different cellular properties - matching the radial pattern of cell layers within the gut. The more adhesive cells in this case, instead of sorting to a simple inside-outside configuration, broke up into multiple rounded cell aggregates, bearing similarity to the dewetting phenomenon of a cohesive liquid on a substrate. The conceptual idea of an array of cells breaking up to aggregates had been suggested in theory previously (Oster et al., 1983). However, to our knowledge this is the first time the differential adhesion concept has been applied to describe dewetting-like cellular patterning within a tissue.

In the previously described differential adhesion driven cell sorting models, the adhesive cell-cell interaction in discussion had been direct cell-cell adhesions mediated through cadherins (Foty and Steinberg, 2005; Steinberg, 1963; Toda et al., 2018). Epithelial cells have clear interfaces with cell polarity where apical, basal and lateral interfaces can be described as direct cell-lumen, cell-ECM and cell-cell interactions, respectively. Mesenchymal cell interactions, on the other hand, are more complex. They typically do not display clear polarity, and the interfaces are described as a combination of cell-cell, cell-ECM or cell-ECM-cell interactions. Therefore, we have hypothesized

that cell adhesion could be described either by direct cell-cell adhesion through cadherins or indirectly through cell-ECM interactions mediated through integrins. Indeed, we observe specific collagen and fibronectin binding integrins expressed within PDGFRα^{High} cells, and inhibiting their functions impairs mesenchymal cell clustering in explant tissue culture. While this serves as evidence supporting the necessity of ECM mediated indirect cell-cell adhesions, we were not able to identify specific cellular interfaces that are enriched for integrin localization as integrins are infamously difficult to stain in tissue. Based on the ECM localization, we have assumed that inhibition of integrin interaction with small molecules would decrease relative PDGFRα^{High} cell adhesion to its kind and to other cellular interfaces. Confirmation of the specific integrin localization and activation would help us make better predictions as to what aspects of adhesion we are perturbing and explain the tissue phenomenon better. The specific combinations of integrin subtype pairs that we have tested with explant culture, Integrin a2b1 and a5b1, had been suggested to induce fibronectin assembly *in vitro* using a contractile actomyosin winch *(Lu et al., 2020)*. Similar interaction involving fibronectin fibril assembly may also be deployed in the intestinal tissue system during cluster formation.

The intercellular and intracellular molecular components that determine cellular mechanics are often shared and interconnected. Uncoupling motility and adhesion, two of the components we determined necessary based on our model, in the explant culture or in *in vitro* system has been a challenge. We were unable to identify specific treatments that only modify cellular motility without interfering with cytoskeleton and cellular adhesion programs. Similarly, it would not be surprising that integrin inhibition

and actomyosin inhibition we have performed may also have unintended consequences to cellular motility or other cellular properties, as cells require a connection to the substrate in order to migrate. Despite the limitations, our data from various inhibitor experiments together support that it is not just adhesion, motility or contractility alone, but likely a combination of these factors together drive the mesenchymal clustering that lead to the villus initiation. Teasing apart each of the factors and assigning a hierarchy of importance to them, in a more reductionist *in vitro* system will be an important future endeavor.

To make our model as concise and targeted as possible, we have decided to simplify the model to initiate from a preformed layer of differentiated PDGFRα^{High} cells sandwiched between the epithelium and PDGFRα^{low} cells. However, in development, the appearance of the differentiated PDGFRα^{High} cells occurs concurrently with the cluster formation. As we have yet to understand the underlying mechanism and dynamics in which the differentiation of PDGFRα^{High} cells is induced, we assumed that the differentiation is slow relative to clustering and differentiation was not implemented in our current model. Understanding the mechanism or the differentiation dynamic would allow us to better implement the cellular distribution in our model, and the differentiation dynamics may also alter the model predictions. Alternatively, if we can build an *in vitro* system in which adhesion or motility programs can be induced, the role of dynamic cellular proportion could be more systematically tested.

Addressing previous models of cluster patterning and morphogenesis

Multiple investigations had been conducted in the past to explain villus morphogenesis. In this section, I will address and discuss the findings by previous investigations and describe alternative hypotheses that might explain discrepancies between these and our current findings.

The presence of orthogonally aligned muscle layers had been suggested to be necessary and sufficient for villus formation by Shyer and colleagues in both chick and in mouse. In this study, they showed that inhibition of muscle layer development by treatment of explant tissue with small molecule inhibitors AG1295 and FK506 resulted in failure to form villi. However, our data clearly show that in mouse constraint by smooth muscle is not required for villus initiation, and thus these compounds might act to prevent villus initiation through other mechanisms. AG1295 is a selective PDGFR tyrosine kinase inhibitor, and as knockout of *Pdgfra* alone resulted in reduction in the number of villus clusters likely due to reduced proliferation, it is not surprising that blocking of all PDGF signals may even further inhibit proliferation of the mesenchyme (Karlsson et al., 2000). It is highly likely that the lack of PDGF signaling in mesenchyme would not only block the differentiation of smooth muscle but also would alter proliferation of the mesenchymal cells, therefore changing the initial mesenchymal tissue compositions. Indeed, our computational model predicts that below a critical number of initial PDGFRα^{High} cells, the clustering behavior is impaired. FK506 on the other hand binds to and inhibits Fkbp, or Fk506 binding protein family. The complex had been reported to inhibit gut smooth muscle differentiation, induce TGFβ receptors availability and inhibit calcineurin activity (Fukuda et al., 1998; Liu et al., 1991; Wang et

al., 1996). One of the calcineurin genes, *Ppp3ca* gene is upregulated in the PDGFRα^{High} mesenchymal cells according to our single-cell sequencing data. Many subtypes of Fkbp genes, Fk506's binding targets, as well as several TGFb receptor genes are also expressed throughout the mesenchyme. As the detailed function of Fbpk is not well understood, it is possible that FK506 inhibits vilification directly through a mechanism independent of its function in inhibiting muscle differentiation. Therefore, investigating the effects of these compounds in light of our new model for villus initiation in the mouse might help to explain the mechanism by which they prevent villus formation.

A role for smooth muscle might be required for later steps of villus formation following the cluster-mediate initiating events. Based on our experience working with intestinal explant culture, villus morphogenesis was only induced reliably when the tissue was cultured on a transwell membrane; these explants had reduced efficiency in developing villi when cultured embedded in soft matrix or floating inside media. Therefore, it is probable that sufficient mechanical support is required for the tissue to develop mature villi, and muscle layer may contribute to providing the extra mechanical support for villus elongation.

Various investigations have suggested the role of hedgehog signaling in intestinal mesenchymal development and villus morphogenesis (Madison et al., 2005; Mao et al., 2010; Walton et al., 2012). Our investigation agrees with these findings that epithelial Hh is indeed necessary and sufficient for the cluster formation. Replacement of epithelial-originated Hh signals by Smoothen agonist treatment in the absence of epithelium was sufficient to drive clustering formation. Still, exactly how Hh signaling

promotes these cell behaviors and whether it is acting instructively or permissively in this process remains unknown.

Walton and colleagues proposed that Bmps and Bmp inhibitors work as Turing inhibitors and activators, respectively to induce mesenchymal cluster patterns in a reaction-diffusion manner. Though reaction-diffusion mechanism is an attractive model to describe the formation of various patterns, the final pattern is highly sensitive to the parameters. Diffusion rate of each morphogen, speed of reaction, initial concentration and model domain size and shape all need to be precisely coordinated to achieve a targeted pattern (Bard and Lauder, 1974; Bunow et al., 1980). Further, these parameter values are arbitrarily assigned to obtain the targeted patterns without numerical evidence. Our proposed model on the other hand not only has fewer variables and is less sensitive to small changes in parameter values - making it a more attractive computational models -, but more importantly is more consistent with our observation of villus morphogenesis. Our live-imaging result observation clearly showed that the cluster formation is a dynamic process, with cells actively moving long distances to generate clusters, as opposed to the patterning of a field of cells into cluster versus non-cluster regions expected from a reaction-diffusion model. In addition, our explant culture experiments imaged with high-resolution 3D confocal microscopy of cleared whole-mount tissues revealed that stripe-like patterns observed upon treatment with the Bmp inhibitor, Dorsomorphin, by Walton might be an imaging artifact due to the imaging of 3D elongated villi from their side views that makes them appear like stripes, when they are really overlapping villi protruding into the lumen from opposite sides of the gut. However, we did observe wider and longer villi in the Dorsomorphin treated tissue,

confirming some roles of Bmp signals in PDGFRα^{High} mesenchymal cluster formation. One possible explanation to this altered phenotype is that Bmp signals may control the number of differentiated PDGFRα^{High} cells, therefore affecting the initial layer thickness in our model.

Recently, Wnt5 has also been suggested as a chemoattractant that drives clustering behavior of the PDGFRα^{High} mesenchymal cells (Rao-Bhatia et al., 2020). The concept of cells finding their path based on the concentration gradient is not consistent with our observation that some cell-nuclei trajectories cross their path. Instead of moving towards the nearest neighboring clusters, those cells moved towards final clusters that are located further away. It will be interesting to further investigate whether Wnt5a has effects on cellular behavior as a chemoattractant or as a general cell activity modulator, such as by increasing baseline cell motility. Since the pathway analysis in their study was performed through bulk-RNA sequencing of all mesenchymal cells including both the PDGFRα^{High} clustering mesenchymal cells and the rest of the bulk mesenchymal population, it is difficult to identify exactly which cell population was affected by the *Spop, Sufu* double knockout genotype. Through our single-cell RNA sequencing data of all the intestinal cells revealed that one of the key genes identified in their study, *Fat4,* is highly enriched in the PDGFRα^{High} cell population after villus initiation. Their study using *Fat4* knockout tissue revealed that the clustering PDGFRα^{High} cells in these mutants were not oriented in direction. However, from the limited number of images they have provided, the initial mesenchymal cluster and basal deformation seems to be present in the *Fat4* knockout tissue. In addition, it is also important to point out that the majority of the tissue in these mutants appears

unaffected, but only small patches of the tissue showed deformed-villi phenotypes. These data make me hypothesize that the PCP-programs are not required for the initial cluster formation and initiation of villi but they are instead required for its subsequent elongation step. Villus fusion in this case may not be due to the failure to form clusters but could be due to its inability to maintain formed clusters as individual villi. It will be intriguing to investigate further whether the initiation of PDGFRα^{High} cell clustering is interfered in these PCP mutant mice.

Previously, rounding of mitotic epithelial cells has been suggested as a contributor of apical invaginations of intestinal epithelium, termed T-folds, that may define the sites of villus initiation (Freddo et al., 2016). Our investigation suggests that mesenchymal cell cluster formation is the main driver of the basal deformation in the intestine, and proliferation is not necessary in the induction of initial buckling morphogenesis. In longitudinally opened intestinal explant, cluster formation directly translated to basal and apical epithelial deformation. However, nascent clusters in tissue often display basal epithelial deformations without accompanied apical deformations. Coordination between epithelium proliferation including mitotic rounding may be necessary in the subsequent step where epithelial basal deformation is accompanied by epithelial apical deformation in a tightly packed lumen.

In summary, these observations suggest that though motility and adhesion driven cell behavior may be sufficient for the PDGFRα^{High} mesenchymal cell clustering and initiation of basal deformation in epithelium, other concurrently coordinated cellular actions happening closely in time are likely present to orchestrate different aspects of the morphogenesis. Investigating the pathways previously implicated in villus formation

in light of our findings will provide insight into how they might act to affect cell motility and adhesion.

4.2 Unresolved questions

Our data revealed that (i) increased actomyosin activity was present in the PDGFRα^{High} clusters, (ii) inhibition of actomyosin activity by Blebbistatin resulted in failure to form mesenchymal cell clustering and (iii) mesenchymal *Myh9* and *Myh10* double knockout tissue showed sensitivity to Blebbistatin treatment. Combining these results together, I feel confident that actomyosin activity in the subepithelial mesenchyme is important for the mesenchymal cluster formation. However, we were not able to see detectable villus phenotypes in mutant tissue directly, even when *Myh9*$^{null/flox}$ *Myh9*$^{null/flox}$ mice were used. Immunostaining and qPCR results suggested that there were still some levels of both gene and protein expressions left. Therefore, I hypothesize that the lack of phenotype is due to the combination of incomplete knockout, perdurance of proteins, and compensation by other myosin proteins, such as *Myh11*. However, it will be a strong supporting piece of evidence to have phenotypes with tissue-specific genetic perturbation. This might be accomplished by generating dominant negative myosin mouse lines or targeting the upstream genes of actomyosin activity such as myosin light chain kinase. However, there are many kinases compensating for each other to regulate myosin phosphorylation, and thus these approaches might present their own challenges.

Another piece of evidence lacking from the current investigation is physical measurements of cellular characteristics. In particular, the hierarchy of adhesion energy

between different cellular interfaces were made based on the gene expression of integrin in combination with the systemic inhibition of integrin activities in explant culture. I have attempted to work with isolated cells from the tissue, however faced challenges due to mainly two reasons: (i) the number of PDGFRα^{High} cells is very low and therefore collecting enough cells to run assays is difficult and (ii) we do not have a good understanding of *in vitro* cell culture conditions that maintain their cellular characteristics. In the current investigation, I have isolated sufficient numbers of GFP+ cells (including both PDGFRα^{low} cells and a small number of PDGFRα^{High} cells) from PDGFRα^{EGFP} intestinal tissues and demonstrated that these cells cluster in ECM, consistent with the general characteristics of contractile mesenchymal cells. However, we were not able to find experimental conditions in which PDGFRα^{High} cells and PDGFRα^{Low} cells can be sorted separately and cultured for this cluster formation assay while maintaining their cellular properties. Figuring out the culture conditions (both media and ECM environment) in which each of the cell properties are reliably maintained would be highly valuable. Once appropriate culture conditions are figured out, the differential adhesion assays such as the sorting assays of both PDGFRα^{High} and PDGFRα^{low} mixed cell aggregates, or assays examining differential clustering kinetics *in vitro* should be performed to confirm or dispute our model assumptions. In addition, our single-cell RNA sequencing results revealed that even among PDGFRα^{High} cells the gene expression is different between the nascently clustering cells and mesenchymal cluster cells at elongating villi. Therefore, even once the cell culture condition *in vitro* is established, ensuring to use the ‘correct’ clustering PDGFRα^{High} cell

population may remain a challenge due the fact that the cell state is rapidly changing between developmental stages.

4.3 Future directions

In chick villus morphogenesis, muscle development had been shown to be responsible for the sequential luminal structural transition from flat to ridges to zigzags (Shyer et al., 2013). However, the last transition from zigzags to individual villi requires additional explanations. It would be interesting to investigate whether a similar mesenchymal cell clustering mechanism is active during this transition. Moreover, intestinal villus shapes vary substantially across species, and while much of this variation can be attributed to different arrangements of muscle layers (Shyer et al., 2013), it will be important to examine whether the mechanism of villus cluster formation we describe here is unique to mammals, or is present, perhaps at different stages in other species.. Moreover, another exciting project would be to investigate the mechanisms deployed by different species from an evolutionary standpoint. Interestingly, the field vole, *Microtus montebelli,* initially develops individual villi which postnatally fuse into zigzag structure (Kurohmaru et al., 1983). In addition, mice with Laminin a5 knockout also showed phenotypes of fused or coalesced villi (Mahoney et al., 2008). These villus fusion phenotypes may or may not be due to mesenchymal tissue activity, but regardless, I would be curious to learn about various structural transition mechanisms of villi.

My thesis investigation focused on understanding the mechanism of villus development in embryos. Another area of my interests is to compare the mechanism

with villus repair. It has been reported that villus atrophy in classical Whipple's disease patients' duodenum were partially recovered upon antibiotic treatment, and azathioprine drug triggered villus atrophy was recovered after discontinuation of the drug treatment (Epple et al., 2017; Ziegler et al., 2003). Identifying whether the similar mesenchymally driven villus initiation mechanism is utilized in villus repair would help us better understand the path towards application of the mechanisms for regeneration and repair *in vivo*.

For my thesis research, I have only mined into the differentiation path of PDGFRα^{High} mesenchymal cells and epithelium from the rich set of single-cell RNA sequencing data we have obtained. Further analysis of developmental paths as well as interaction between different cell types should be performed. In particular, I am interested in identifying specific gene characteristics and underlying mechanisms that define developmental versus regional differentiation. Further, learning about interactions among these different cell types and how they achieve the coordinated cellular behavior leading to villus morphogenesis would be a great addition to the field. One observation that intrigued me from the epithelium data was the presence of differentiated secretory cells even before the villus morphogenesis or the presence of Lgr5 expressing stem cells. Identifying the origins of secretory cells and what induces their differentiation would be another interesting project. Furthermore, my dataset also contains many other cell types I had not been able to look into in detail, including Ptn+ mesenchymal cells, endothelial cells and immune cells. Villus morphogenesis is accompanied by recruitment of endothelial cells to the villus core. Looking into the possible signaling ligands secreted by either mesenchymal cells or villus epithelium that direct

angiogenesis and differentiation of villus-specific endothelial cell types is another question that could be investigated through the existing dataset. In adults, distinct populations of intestinal mesenchymal cell types have been identified. These include PDGFRα^{High} telocytes, trophocytes, myocytes and pericytes. However, a lot of the gene markers were not as clearly expressed in the fetal mesenchymal dataset I have generated. Combining our dataset from embryonic intestines together with adult single-cell sequencing dataset would allow us to better understand maturation pathways and lineages of each cell type.

4.4 Conclusion

In summary, I have utilized a multifaceted approach incorporating live imaging, single-cell transcriptional analysis, in vivo and explant tissue experiments, a series of computational models, and *in vitro* engineering to investigate cellular mechanisms that drive villus morphogenesis. I found that PDGFRα^{High} mesenchymal cells form clusters in an adhesion and motility-driven mechanism to initiate basal epithelial deformation at the sites of villus initiation. Validation of the model in tissue explants and in *in vitro* simplified systems allowed us to verify the applicability of our model in driving biological pattern formation. I believe that our work has demonstrated a distinctive mechanism and provided new insights to describe cellular organization during development.

References

Bard, J., Lauder, I., 1974. How well does Turing's theory of morphogenesis work? Journal of Theoretical Biology 45, 501–531. https://doi.org/10.1016/0022-5193(74)90128-3

Barker, N., 2014. Adult intestinal stem cells: critical drivers of epithelial homeostasis and regeneration. Nat Rev Mol Cell Biol 15, 19–33. https://doi.org/10.1038/nrm3721

Barton, D.L., Henkes, S., Weijer, C.J., Sknepnek, R., 2017. Active Vertex Model for cell-resolution description of epithelial tissue mechanics. PLoS Comput Biol 13, e1005569. https://doi.org/10.1371/journal.pcbi.1005569

Becht, E., McInnes, L., Healy, J., Dutertre, C.-A., Kwok, I.W.H., Ng, L.G., Ginhoux, F., Newell, E.W., 2019. Dimensionality reduction for visualizing single-cell data using UMAP. Nat Biotechnol 37, 38–44. https://doi.org/10.1038/nbt.4314

Bellusci, S., Grindley, J., Emoto, H., Itoh, N., Hogan, B.L., 1997. Fibroblast growth factor 10 (FGF10) and branching morphogenesis in the embryonic mouse lung. Development 124, 4867–4878. https://doi.org/10.1242/dev.124.23.4867

Bernfield, M.R., Banerjee, S.D., Cohn, R.H., 1972. Dependence of salivery epithelial morphology and branching morphogenesis upon acid mucopolysaccharide-protein (proteoglycan) at the epithelial surface. Journal of Cell Biology 52, 674–689. https://doi.org/10.1083/jcb.52.3.674

Bi, D., Yang, X., Marchetti, M.C., Manning, M.L., 2016. Motility-Driven Glass and Jamming Transitions in Biological Tissues. Phys. Rev. X 6, 021011. https://doi.org/10.1103/PhysRevX.6.021011

Bresciani, F., 1968. Topography of DNA synthesis in the mammary gland of the C3H mouse and its control by ovarian hormones: an autoradiographic study. Cell Prolif 1, 51–63. https://doi.org/10.1111/j.1365-2184.1968.tb00193.x

Bunow, B., Kernevez, J.-P., Joly, G., Thomas, D., 1980. Pattern formation by reaction-diffusion instabilities: Application to morphogenesis in Drosophila. Journal of Theoretical Biology 84, 629–649. https://doi.org/10.1016/S0022-5193(80)80024-5

Cabral, K.A., Patterson, D.M., Scheideler, O.J., Cole, R., Abate, A.R., Schaffer, D.V., Sohn, L.L., Gartner, Z.J., 2021. Simple, Affordable, and Modular Patterning of Cells using DNA. JoVE 61937. https://doi.org/10.3791/61937

Cahn, J.W., Hilliard, J.E., 1958. Free Energy of a Nonuniform System. I. Interfacial Free Energy. The Journal of Chemical Physics 28, 258–267. https://doi.org/10.1063/1.1744102

Chung, M.-I., Bujnis, M., Barkauskas, C.E., Kobayashi, Y., Hogan, B.L.M., 2018. Niche-mediated BMP/SMAD signaling regulates lung alveolar stem cell proliferation and differentiation. Development 145, dev163014. https://doi.org/10.1242/dev.163014

Clevers, H., 2013. The Intestinal Crypt, A Prototype Stem Cell Compartment. Cell 154, 274–284. https://doi.org/10.1016/j.cell.2013.07.004

Coquenlorge, S., Yin, W.-C., Yung, T., Pan, J., Zhang, X., Mo, R., Belik, J., Hui, C., Kim, T.-H., 2019. GLI2 Modulated by SUFU and SPOP Induces Intestinal Stem Cell Niche Signals in Development and Tumorigenesis. Cell Reports 27, 3006-3018.e4. https://doi.org/10.1016/j.celrep.2019.05.016

Coulombre, A.J., Coulombre, J.L., 1958. Intestinal Development. Development 6, 403–411. https://doi.org/10.1242/dev.6.3.403

Darwich, A.S., Aslam, U., Ashcroft, D.M., Rostami-Hodjegan, A., 2014. Meta-Analysis of the Turnover of Intestinal Epithelia in Preclinical Animal Species and Humans. Drug Metab Dispos 42, 2016–2022. https://doi.org/10.1124/dmd.114.058404

Elmentaite, R., Ross, A.D.B., Roberts, K., James, K.R., Ortmann, D., Gomes, T., Nayak, K., Tuck, L., Pritchard, S., Bayraktar, O.A., Heuschkel, R., Vallier, L., Teichmann, S.A., Zilbauer, M., 2020. Single-Cell Sequencing of Developing Human Gut Reveals

Transcriptional Links to Childhood Crohn's Disease. Developmental Cell 55, 771-783.e5. https://doi.org/10.1016/j.devcel.2020.11.010

Epple, H.-J., Friebel, J., Moos, V., Troeger, H., Krug, S.M., Allers, K., Schinnerling, K., Fromm, A., Siegmund, B., Fromm, M., Schulzke, J.D., Schneider, T., 2017. Architectural and functional alterations of the small intestinal mucosa in classical Whipple's disease. Mucosal Immunol 10, 1542–1552. https://doi.org/10.1038/mi.2017.6

Foty, R.A., Steinberg, M.S., 2005. The differential adhesion hypothesis: a direct evaluation. Developmental Biology 278, 255–263. https://doi.org/10.1016/j.ydbio.2004.11.012

Freddo, A.M., Shoffner, S.K., Shao, Y., Taniguchi, K., Grosse, A.S., Guysinger, M.N., Wang, S., Rudraraju, S., Margolis, B., Garikipati, K., Schnell, S., Gumucio, D.L., 2016. Coordination of signaling and tissue mechanics during morphogenesis of murine intestinal villi: a role for mitotic cell rounding. Integr. Biol. 8, 918–928. https://doi.org/10.1039/C6IB00046K

Fukuda, K., Tanigawa, Y., Fujii, G., Yasugi, S., Hirohashi, S., 1998. cFKBP/SMAP; a novel molecule involved in the regulation of smooth muscle differentiation. Development 125, 3535–3542. https://doi.org/10.1242/dev.125.18.3535

Gonzalez-Rodriguez, D., Guevorkian, K., Douezan, S., Brochard-Wyart, F., 2012. Soft Matter Models of Developing Tissues and Tumors. Science 338, 910–917. https://doi.org/10.1126/science.1226418

Guiu, J., Hannezo, E., Yui, S., Demharter, S., Ulyanchenko, S., Maimets, M., Jørgensen, A., Perlman, S., Lundvall, L., Mamsen, L.S., Larsen, A., Olesen, R.H., Andersen, C.Y., Thuesen, L.L., Hare, K.J., Pers, T.H., Khodosevich, K., Simons, B.D., Jensen, K.B., 2019. Tracing the origin of adult intestinal stem cells. Nature 570, 107–111. https://doi.org/10.1038/s41586-019-1212-5

Haber, A.L., Biton, M., Rogel, N., Herbst, R.H., Shekhar, K., Smillie, C., Burgin, G., Delorey, T.M., Howitt, M.R., Katz, Y., Tirosh, I., Beyaz, S., Dionne, D., Zhang, M., Raychowdhury,

R., Garrett, W.S., Rozenblatt-Rosen, O., Shi, H.N., Yilmaz, O., Xavier, R.J., Regev, A., 2017. A single-cell survey of the small intestinal epithelium. Nature 551, 333–339. https://doi.org/10.1038/nature24489

Hafemeister, C., Satija, R., 2019. Normalization and variance stabilization of single-cell RNA-seq data using regularized negative binomial regression. Genome Biol 20, 296. https://doi.org/10.1186/s13059-019-1874-1

Hamilton, T.G., Klinghoffer, R.A., Corrin, P.D., Soriano, P., 2003. Evolutionary Divergence of Platelet-Derived Growth Factor Alpha Receptor Signaling Mechanisms. Mol Cell Biol 23, 4013–4025. https://doi.org/10.1128/MCB.23.11.4013-4025.2003

Harfe, B.D., Scherz, P.J., Nissim, S., Tian, H., McMahon, A.P., Tabin, C.J., 2004. Evidence for an Expansion-Based Temporal Shh Gradient in Specifying Vertebrate Digit Identities. Cell 118, 517–528. https://doi.org/10.1016/j.cell.2004.07.024

Harris, A.K., 1976. Is cell sorting caused by differences in the work of intercellular adhesion? A critique of the steinberg hypothesis. Journal of Theoretical Biology 61, 267–285. https://doi.org/10.1016/0022-5193(76)90019-9

Hartl, L., Huelsz-Prince, G., van Zon, J., Tans, S.J., 2019. Apical constriction is necessary for crypt formation in small intestinal organoids. Developmental Biology 450, 76–81. https://doi.org/10.1016/j.ydbio.2019.03.009

Helander, H.F., Fändriks, L., 2014. Surface area of the digestive tract – revisited. Scandinavian Journal of Gastroenterology 49, 681–689. https://doi.org/10.3109/00365521.2014.898326

Hertz, H., 1882. On the contact of elastic solids. J. Reine Angew. Math. 92, 156–171.

Huang, J., Cheng, L., Li, J., Chen, M., Zhou, D., Lu, M.M., Proweller, A., Epstein, J.A., Parmacek, M.S., 2008. Myocardin regulates expression of contractile genes in smooth muscle cells and is required for closure of the ductus arteriosus in mice. J. Clin. Invest. JCI33304. https://doi.org/10.1172/JCI33304

Hughes, A.J., Miyazaki, H., Coyle, M.C., Zhang, J., Laurie, M.T., Chu, D., Vavrušová, Z., Schneider, R.A., Klein, O.D., Gartner, Z.J., 2018. Engineered Tissue Folding by Mechanical Compaction of the Mesenchyme. Developmental Cell 44, 165-178.e6. https://doi.org/10.1016/j.devcel.2017.12.004

Hutter, J.L., Bechhoefer, J., 1993. Calibration of atomic-force microscope tips. Review of Scientific Instruments 64, 1868–1873. https://doi.org/10.1063/1.1143970

Huycke, T.R., Miller, B.M., Gill, H.K., Nerurkar, N.L., Sprinzak, D., Mahadevan, L., Tabin, C.J., 2019. Genetic and Mechanical Regulation of Intestinal Smooth Muscle Development. Cell 179, 90-105.e21. https://doi.org/10.1016/j.cell.2019.08.041

Irion, S., Nostro, M.C., Kattman, S.J., Keller, G.M., 2008. Directed Differentiation of Pluripotent Stem Cells: From Developmental Biology to Therapeutic Applications. Cold Spring Harbor Symposia on Quantitative Biology 73, 101–110. https://doi.org/10.1101/sqb.2008.73.065

Jacobelli, J., Friedman, R.S., Conti, M.A., Lennon-Dumenil, A.-M., Piel, M., Sorensen, C.M., Adelstein, R.S., Krummel, M.F., 2010. Confinement-optimized three-dimensional T cell amoeboid motility is modulated via myosin IIA–regulated adhesions. Nat Immunol 11, 953–961. https://doi.org/10.1038/ni.1936

Kammeraad, A., 1942. The development of the gastro-intestinal tract of the rat. I. Histogenesis of the epithelium of the stomach, small intestine and pancreas. J. Morphol. 70, 323–351. https://doi.org/10.1002/jmor.1050700209

Karlsson, L., Lindahl, P., Heath, J.K., Betsholtz, C., 2000. Abnormal gastrointestinal development in PDGF-A and PDGFR-(alpha) deficient mice implicates a novel mesenchymal structure with putative instructive properties in villus morphogenesis. Development 127, 3457–3466. https://doi.org/10.1242/dev.127.16.3457

Kim, H.Y., Pang, M.-F., Varner, V.D., Kojima, L., Miller, E., Radisky, D.C., Nelson, C.M., 2015. Localized Smooth Muscle Differentiation Is Essential for Epithelial Bifurcation during

Branching Morphogenesis of the Mammalian Lung. Developmental Cell 34, 719–726. https://doi.org/10.1016/j.devcel.2015.08.012

Kim, H.Y., Varner, V.D., Nelson, C.M., 2013. Apical constriction initiates new bud formation during monopodial branching of the embryonic chicken lung. Development 140, 3146–3155. https://doi.org/10.1242/dev.093682

Koyama, H., Shi, D., Suzuki, M., Ueno, N., Uemura, T., Fujimori, T., 2016. Mechanical Regulation of Three-Dimensional Epithelial Fold Pattern Formation in the Mouse Oviduct. Biophysical Journal 111, 650–665. https://doi.org/10.1016/j.bpj.2016.06.032

Kurohmaru, M., Hayakawa, T., Seki, M., Zyo, K., Nishida, T., Mochizuki, K., 1983. Postnatal Development of Intestinal Villi in the Field Vole (Microtus montebelli): A Scanning Electron Microscopic Study. Okajimas Folia Anatomica Japonica 60, 73–85. https://doi.org/10.2535/ofaj1936.60.2-3_73

Kwon, O., Han, T.-S., Son, M.-Y., 2020. Intestinal Morphogenesis in Development, Regeneration, and Disease: The Potential Utility of Intestinal Organoids for Studying Compartmentalization of the Crypt-Villus Structure. Front. Cell Dev. Biol. 8, 593969. https://doi.org/10.3389/fcell.2020.593969

Lecuit, T., Lenne, P.-F., 2007. Cell surface mechanics and the control of cell shape, tissue patterns and morphogenesis. Nat Rev Mol Cell Biol 8, 633–644. https://doi.org/10.1038/nrm2222

Leptin, M., 1995. Drosophila Gastrulation: From Pattern Formation to Morphogenesis. Annu. Rev. Cell Dev. Biol. 11, 189–212. https://doi.org/10.1146/annurev.cb.11.110195.001201

Lewandoski, M., Meyers, E.N., Martin, G.R., 1997. Analysis of Fgf8 gene function in vertebrate development. Cold Spring Harbor Symposia on Quantitative Biology 62, 159–168. https://doi.org/10.1101/SQB.1997.062.01.021

Lewis, W.H., 1947. Mechanics of invagination. Anat. Rec. 97, 139–156. https://doi.org/10.1002/ar.1090970203

Liu, J., Farmer, J.D., Lane, W.S., Friedman, J., Weissman, I., Schreiber, S.L., 1991. Calcineurin is a common target of cyclophilin-cyclosporin A and FKBP-FK506 complexes. Cell 66, 807–815. https://doi.org/10.1016/0092-8674(91)90124-H

Lopez, J.I., Kang, I., You, W.-K., McDonald, D.M., Weaver, V.M., 2011. In situ force mapping of mammary gland transformation. Integr. Biol. 3, 1233. https://doi.org/10.1039/c1ib90045e

Lu, J., Doyle, A.D., Shinsato, Y., Wang, S., Bodendorfer, M.A., Zheng, M., Yamada, K.M., 2020. Basement Membrane Regulates Fibronectin Organization Using Sliding Focal Adhesions Driven by a Contractile Winch. Developmental Cell 52, 631-646.e4. https://doi.org/10.1016/j.devcel.2020.01.007

Ma, X., Kawamoto, S., Hara, Y., Adelstein, R.S., 2004. A Point Mutation in the Motor Domain of Nonmuscle Myosin II-B Impairs Migration of Distinct Groups of Neurons. MBoC 15, 2568–2579. https://doi.org/10.1091/mbc.e03-11-0836

Madisen, L., Zwingman, T.A., Sunkin, S.M., Oh, S.W., Zariwala, H.A., Gu, H., Ng, L.L., Palmiter, R.D., Hawrylycz, M.J., Jones, A.R., Lein, E.S., Zeng, H., 2010. A robust and high-throughput Cre reporting and characterization system for the whole mouse brain. Nat Neurosci 13, 133–140. https://doi.org/10.1038/nn.2467

Madison, B.B., Braunstein, K., Kuizon, E., Portman, K., Qiao, X.T., Gumucio, D.L., 2005. Epithelial hedgehog signals pattern the intestinal crypt-villus axis. Development 132, 279–289. https://doi.org/10.1242/dev.01576

Mahoney, Z.X., Stappenbeck, T.S., Miner, J.H., 2008. Laminin α5 influences the architecture of the mouse small intestine mucosa. Journal of Cell Science 121, 2493–2502. https://doi.org/10.1242/jcs.025528

Mao, J., Kim, B.-M., Rajurkar, M., Shivdasani, R.A., McMahon, A.P., 2010. Hedgehog signaling controls mesenchymal growth in the developing mammalian digestive tract. Development 137, 1721–1729. https://doi.org/10.1242/dev.044586

Martinez-Rico, C., Pincet, F., Thiery, J.-P., Dufour, S., 2010. Integrins stimulate E-cadherin-mediated intercellular adhesion by regulating Src-kinase activation and actomyosin contractility. Journal of Cell Science 123, 712–722. https://doi.org/10.1242/jcs.047878

Mayhew, T.M., Myklebust, R, Whybrow, A, Jenkins, R, 1999. Epithelial integrity, cell death and cell loss in mammalian small intestine. Histology and Histopathology 257–267. https://doi.org/10.14670/HH-14.257

McGinnis, C.S., Murrow, L.M., Gartner, Z.J., 2019a. DoubletFinder: Doublet Detection in Single-Cell RNA Sequencing Data Using Artificial Nearest Neighbors. Cell Systems 8, 329-337.e4. https://doi.org/10.1016/j.cels.2019.03.003

McGinnis, C.S., Patterson, D.M., Winkler, J., Conrad, D.N., Hein, M.Y., Srivastava, V., Hu, J.L., Murrow, L.M., Weissman, J.S., Werb, Z., Chow, E.D., Gartner, Z.J., 2019b. MULTI-seq: sample multiplexing for single-cell RNA sequencing using lipid-tagged indices. Nat Methods 16, 619–626. https://doi.org/10.1038/s41592-019-0433-8

Michael, L., Davies, J.A., 2004. Pattern and regulation of cell proliferation during murine ureteric bud development. J Anatomy 204, 241–255. https://doi.org/10.1111/j.0021-8782.2004.00285.x

Misra, M., Audoly, B., Kevrekidis, I.G., Shvartsman, S.Y., 2016. Shape Transformations of Epithelial Shells. Biophysical Journal 110, 1670–1678. https://doi.org/10.1016/j.bpj.2016.03.009

Mongera, A., Rowghanian, P., Gustafson, H.J., Shelton, E., Kealhofer, D.A., Carn, E.K., Serwane, F., Lucio, A.A., Giammona, J., Campàs, O., 2018. A fluid-to-solid jamming transition underlies vertebrate body axis elongation. Nature 561, 401–405. https://doi.org/10.1038/s41586-018-0479-2

Muzumdar, M.D., Tasic, B., Miyamichi, K., Li, L., Luo, L., 2007. A global double-fluorescent Cre reporter mouse. genesis 45, 593–605. https://doi.org/10.1002/dvg.20335

Nusse, Y.M., Savage, A.K., Marangoni, P., Rosendahl-Huber, A.K.M., Landman, T.A., de Sauvage, F.J., Locksley, R.M., Klein, O.D., 2018. Parasitic helminths induce fetal-like reversion in the intestinal stem cell niche. Nature 559, 109–113. https://doi.org/10.1038/s41586-018-0257-1

Oster, G.F., Murray, J.D., Harris, A.K., 1983. Mechanical aspects of mesenchymal morphogenesis. Development 78, 83–125. https://doi.org/10.1242/dev.78.1.83

Panousopoulou, E., Green, J.B.A., 2016. Invagination of Ectodermal Placodes Is Driven by Cell Intercalation-Mediated Contraction of the Suprabasal Tissue Canopy. PLoS Biol 14, e1002405. https://doi.org/10.1371/journal.pbio.1002405

Rao-Bhatia, A., Zhu, M., Yin, W.-C., Coquenlorge, S., Zhang, X., Woo, J., Sun, Y., Dean, C.H., Liu, A., Hui, C., Shivdasani, R.A., McNeill, H., Hopyan, S., Kim, T.-H., 2020. Hedgehog-Activated Fat4 and PCP Pathways Mediate Mesenchymal Cell Clustering and Villus Formation in Gut Development. Developmental Cell 52, 647-658.e6. https://doi.org/10.1016/j.devcel.2020.02.003

Raudvere, U., Kolberg, L., Kuzmin, I., Arak, T., Adler, P., Peterson, H., Vilo, J., 2019. g:Profiler: a web server for functional enrichment analysis and conversions of gene lists (2019 update). Nucleic Acids Research 47, W191–W198. https://doi.org/10.1093/nar/gkz369

Sato, T., Vries, R.G., Snippert, H.J., van de Wetering, M., Barker, N., Stange, D.E., van Es, J.H., Abo, A., Kujala, P., Peters, P.J., Clevers, H., 2009. Single Lgr5 stem cells build crypt-villus structures in vitro without a mesenchymal niche. Nature 459, 262–265. https://doi.org/10.1038/nature07935

Savin, T., Kurpios, N.A., Shyer, A.E., Florescu, P., Liang, H., Mahadevan, L., Tabin, C.J., 2011. On the growth and form of the gut. Nature 476, 57–62. https://doi.org/10.1038/nature10277

Sawyer, J.M., Harrell, J.R., Shemer, G., Sullivan-Brown, J., Roh-Johnson, M., Goldstein, B., 2010. Apical constriction: A cell shape change that can drive morphogenesis. Developmental Biology 341, 5–19. https://doi.org/10.1016/j.ydbio.2009.09.009

Sbarbati, R., 1982. Morphogenesis of the intestinal villi of the mouse embryo: chance and spatial necessity. J Anat 135, 477–499.

Shahjalal, H.Md., Abdal Dayem, A., Lim, K.M., Jeon, T., Cho, S.-G., 2018. Generation of pancreatic β cells for treatment of diabetes: advances and challenges. Stem Cell Res Ther 9, 355. https://doi.org/10.1186/s13287-018-1099-3

Shyer, A.E., Huycke, T.R., Lee, C., Mahadevan, L., Tabin, C.J., 2015. Bending Gradients: How the Intestinal Stem Cell Gets Its Home. Cell 161, 569–580. https://doi.org/10.1016/j.cell.2015.03.041

Shyer, A.E., Rodrigues, A.R., Schroeder, G.G., Kassianidou, E., Kumar, S., Harland, R.M., 2017. Emergent cellular self-organization and mechanosensation initiate follicle pattern in the avian skin. Science 357, 811–815. https://doi.org/10.1126/science.aai7868

Shyer, A.E., Tallinen, T., Nerurkar, N.L., Wei, Z., Gil, E.S., Kaplan, D.L., Tabin, C.J., Mahadevan, L., 2013. Villification: How the Gut Gets Its Villi. Science 342, 212–218. https://doi.org/10.1126/science.1238842

Šošić, D., Richardson, J.A., Yu, K., Ornitz, D.M., Olson, E.N., 2003. Twist Regulates Cytokine Gene Expression through a Negative Feedback Loop that Represses NF-κB Activity. Cell 112, 169–180. https://doi.org/10.1016/S0092-8674(03)00002-3

Spence, J.R., Lauf, R., Shroyer, N.F., 2011. Vertebrate intestinal endoderm development. Dev. Dyn. 240, 501–520. https://doi.org/10.1002/dvdy.22540

Sprangers, J., Zaalberg, I.C., Maurice, M.M., 2021. Organoid-based modeling of intestinal development, regeneration, and repair. Cell Death Differ 28, 95–107. https://doi.org/10.1038/s41418-020-00665-z

Steinberg, M.S., 1963. Reconstruction of Tissues by Dissociated Cells. Science 141, 401–408.

Street, K., Risso, D., Fletcher, R.B., Das, D., Ngai, J., Yosef, N., Purdom, E., Dudoit, S., 2018. Slingshot: cell lineage and pseudotime inference for single-cell transcriptomics. BMC Genomics 19, 477. https://doi.org/10.1186/s12864-018-4772-0

Stuart, T., Butler, A., Hoffman, P., Hafemeister, C., Papalexi, E., Mauck, W.M., Hao, Y., Stoeckius, M., Smibert, P., Satija, R., 2019. Comprehensive Integration of Single-Cell Data. Cell 177, 1888-1902.e21. https://doi.org/10.1016/j.cell.2019.05.031

Sumigray, K.D., Terwilliger, M., Lechler, T., 2018. Morphogenesis and Compartmentalization of the Intestinal Crypt. Developmental Cell 45, 183-197.e5. https://doi.org/10.1016/j.devcel.2018.03.024

Tallinen, T., Chung, J.Y., Rousseau, F., Girard, N., Lefèvre, J., Mahadevan, L., 2016. On the growth and form of cortical convolutions. Nature Phys 12, 588–593. https://doi.org/10.1038/nphys3632

Thevenaz, P., Ruttimann, U.E., Unser, M., 1998. A pyramid approach to subpixel registration based on intensity. IEEE Trans. on Image Process. 7, 27–41. https://doi.org/10.1109/83.650848

Toda, S., Blauch, L.R., Tang, S.K.Y., Morsut, L., Lim, W.A., 2018. Programming self-organizing multicellular structures with synthetic cell-cell signaling. Science 361, 156–162. https://doi.org/10.1126/science.aat0271

Todhunter, M.E., Jee, N.Y., Hughes, A.J., Coyle, M.C., Cerchiari, A., Farlow, J., Garbe, J.C., LaBarge, M.A., Desai, T.A., Gartner, Z.J., 2015. Programmed synthesis of three-dimensional tissues. Nat Methods 12, 975–981. https://doi.org/10.1038/nmeth.3553

Turing, Alan.M., 1952. The chemical basis of morphogenesis. Phil. Trans. R. Soc. Lond. B 237, 37–72. https://doi.org/10.1098/rstb.1952.0012

Van den Berge, K., Roux de Bézieux, H., Street, K., Saelens, W., Cannoodt, R., Saeys, Y., Dudoit, S., Clement, L., 2020. Trajectory-based differential expression analysis for

single-cell sequencing data. Nat Commun 11, 1201. https://doi.org/10.1038/s41467-020-14766-3

Varner, V.D., Nelson, C.M., 2014. Cellular and physical mechanisms of branching morphogenesis. Development 141, 2750–2759. https://doi.org/10.1242/dev.104794

Vicente-Manzanares, M., Ma, X., Adelstein, R.S., Horwitz, A.R., 2009. Non-muscle myosin II takes centre stage in cell adhesion and migration. Nat Rev Mol Cell Biol 10, 778–790. https://doi.org/10.1038/nrm2786

Walton, K.D., Kolterud, Å., 2014. Mouse Fetal Whole Intestine Culture System for Ex Vivo Manipulation of Signaling Pathways and Three-dimensional Live Imaging of Villus Development. JoVE 51817. https://doi.org/10.3791/51817

Walton, K.D., Kolterud, A., Czerwinski, M.J., Bell, M.J., Prakash, A., Kushwaha, J., Grosse, A.S., Schnell, S., Gumucio, D.L., 2012. Hedgehog-responsive mesenchymal clusters direct patterning and emergence of intestinal villi. Proceedings of the National Academy of Sciences 109, 15817–15822. https://doi.org/10.1073/pnas.1205669109

Walton, K.D., Mishkind, D., Riddle, M.R., Tabin, C.J., Gumucio, D.L., 2018. Blueprint for an intestinal villus: Species-specific assembly required. WIREs Dev Biol 7. https://doi.org/10.1002/wdev.317

Walton, K.D., Whidden, M., Kolterud, Å., Shoffner, S., Czerwinski, M.J., Kushwaha, J., Parmar, N., Chandhrasekhar, D., Freddo, A.M., Schnell, S., Gumucio, D.L., 2016. Villification in the mouse: Bmp signals control intestinal villus patterning. Development dev.130112. https://doi.org/10.1242/dev.130112

Wang, T., Li, B.-Y., Danielson, P.D., Shah, P.C., Rockwell, S., Lechleider, R.J., Martin, J., Manganaro, T., Donahoe, P.K., 1996. The Immunophilin FKBP12 Functions as a Common Inhibitor of the TGFβ Family Type I Receptors. Cell 86, 435–444. https://doi.org/10.1016/S0092-8674(00)80116-6

Weaver, M., Dunn, N.R., Hogan, B.L., 2000. Bmp4 and Fgf10 play opposing roles during lung bud morphogenesis. Development 127, 2695–2704. https://doi.org/10.1242/dev.127.12.2695

Williams, J.M., Duckworth, C.A., Burkitt, M.D., Watson, A.J.M., Campbell, B.J., Pritchard, D.M., 2015. Epithelial Cell Shedding and Barrier Function: A Matter of Life and Death at the Small Intestinal Villus Tip. Vet Pathol 52, 445–455. https://doi.org/10.1177/0300985814559404

Yui, S., Azzolin, L., Maimets, M., Pedersen, M.T., Fordham, R.P., Hansen, S.L., Larsen, H.L., Guiu, J., Alves, M.R.P., Rundsten, C.F., Johansen, J.V., Li, Y., Madsen, C.D., Nakamura, T., Watanabe, M., Nielsen, O.H., Schweiger, P.J., Piccolo, S., Jensen, K.B., 2018. YAP/TAZ-Dependent Reprogramming of Colonic Epithelium Links ECM Remodeling to Tissue Regeneration. Cell Stem Cell 22, 35-49.e7. https://doi.org/10.1016/j.stem.2017.11.001

Ziegler, T.R., Fernández-Estívariz, C., Gu, L.H., Fried, M.W., Leader, L.M., 2003. Severe villus atrophy and chronic malabsorption induced by azathioprine. Gastroenterology 124, 1950–1957. https://doi.org/10.1016/S0016-5085(03)00405-0

Publishing Agreement

It is the policy of the University to encourage open access and broad distribution of all theses, dissertations, and manuscripts. The Graduate Division will facilitate the distribution of UCSF theses, dissertations, and manuscripts to the UCSF Library for open access and distribution. UCSF will make such theses, dissertations, and manuscripts accessible to the public and will take reasonable steps to preserve these works in perpetuity.

I hereby grant the non-exclusive, perpetual right to The Regents of the University of California to reproduce, publicly display, distribute, preserve, and publish copies of my thesis, dissertation, or manuscript in any form or media, now existing or later derived, including access online for teaching, research, and public service purposes.

DocuSigned by:
Hikaru Miyazaki
5B69C0AEA19A4D3...
Author Signature

12/16/2021
Date